LEAN BLOWOUT MITIGATION IN SWIRL STABILIZED PREMIXED FLAMES

A Dissertation
Presented to
The Academic Faculty

by

Shashvat Prakash

In Partial Fulfillment
of the Requirements for the Degree
Doctor of Philosophy in the
Woodruff School of Mechanical Engineering

Georgia Institute of Technology
August 2007

LEAN BLOWOUT MITIGATION IN SWIRL

STABILIZED PREMIXED FLAMES

Approved by:

Dr. Ben T. Zinn, Advisor
Schools of Mechanical and Aerospace Engineering
Georgia Institute of Technology

Dr. Wayne Book
School of Mechanical Engineering
Georgia Institute of Technology

Dr. Timothy Lieuwen
School of Aerospace Engineering
Georgia Institute of Technology

Dr. Nader Sadegh
School of Mechanical Engineering
Georgia Institute of Technology

Dr. Yedidia Neumeier
School of Aerospace Engineering
Georgia Institute of Technology

Date Approved: June 29, 2007

I dedicate this thesis to my family and friends who supported me throughout my doctoral studies and to the memory of my late grandfather, Prof. Devendra Prasad, whose career and values will always be a source of inspiration.

ACKNOWLEDGEMENTS

I wish to thank my advisor, Prof. Ben T. Zinn, for his guidance, Adjunct Professor Yedidia Neumeier, Professors Tim Lieuwen, Jerry Seitzman,, J. Jagoda, from the Aerospace Department, and former colleagues Asst. Prof. T. M. Muruganandam and Dr. Suraj Nair for their contributions to the field of lean blowout and for their support and feedback. I also wish to acknowledge the technical support of Mr. David Scarborough, Prof. J. V. Prasad, and Dr. Manuj Dhingra of the Aerospace Engineering Department, Professors Wayne Book and Nader Sadegh of the Mechanical Engineering Department, and Prof. Zvi Rusak from Rensselaer Polytechnic Institute.

I am thankful for my wife, Priyanka, daughter, Ashna, and my parents, in-laws and extended family, who all remained supportive of my vision of completing my doctorate throughout the difficult and financially uncertain times. I am thankful also for my cousin, Shruti, and her fiancé, Amit, both Ph.D. students, who made it possible for me to submit this thesis.

I am grateful to all the past and present students at the Ben Zinn Combustion Laboratory who helped me formulate and test my ideas or otherwise helped me overcome the rigors of daily life as a married graduate student with a daughter. In no particular order, they are: Tom W., Qingguo, Sai, Preetham, Santosh H., Santosh S., Arun, Yogish, Adithya, Bobby, John C., Yash, Rajesh, Choi, Thao, J.P., Mohan 'Bobba', Nori, Priya, Colby, Randy, Ben B., Demitry, and Adam C.

TABLE OF CONTENTS

LIST OF FIGURES

LIST OF SYMBOLS

α	Mass Diffusivity
Δ	Uncertainty, Change
δ	Event Spacing
ϕ	Equivalence Ratio
γ	Alarm Frequency
η	Operating State, Conserved Scalar
μ	Mean Event Spacing
κ	Number of Presumed Events
ν	Stoichiometric Coefficient
τ	Time Constant
ρ	Density
Ψ	Stream Function
ζ	Forgetting Filter Parameter
A	Alarm Signal
D	Mass Diffusivity
Da	Damkohler Number
c_p	Specific Heat at Constant Pressure
$\Delta E^*(\delta)$	Mean Event Spacing Uncertainty, Normalized
e	Estimation Error
f	Sample Frequency
H	Enthalpy, Filter Transfer Function
ΔH_R	Heat of Reaction
h	Specific Enthalpy

i	Species Index
K	DC Gain
k	Thermal Conduction Coefficient, Time Index
K_p	Proportional Gain
K_d	Derivative Gain
M	Margin
$\dot{m}''$	Mass Flux
N_T	Number of Observed Events in Interval
P	Pressure, Probability
ΔP^*	Normalized Probability Uncertainty
Re	Reynolds Number
r^*	Anchoring Radius of Conical Flame
S	Swirl Number, Signal
S_L	Laminar Flame Speed
s	Complex Laplace Variable
T	Temperature, Time Interval
U	Internal Energy
U_{ref}	Reference Velocity in a Turbulent Flow
u	Specific Internal Energy
V	Volume
v_e	Reactant Exit Velocity
Y	Mass Fraction
z	Discrete Complex Variable

LIST OF ABBREVIATIONS

ffilt	Forgetting Filter
high	Downstream PMT
int	Interface
mid	Midpoint PMT
NOx	Nitrogen Oxides
LBO	Lean Blow Out
LES	Large Eddy Simulation
PMT	Photomultiplier Transducer
RR	Reaction Rate
win	Moving Window

SUMMARY

Lean, premixed combustion has been aggressively pursued in recent years because it offers a practical approach for reducing emissions of nitrogen oxides (NOx) from gas turbines in both aircraft and land based applications. However, lean, premixed flames pose a greater risk of lean blowout (LBO). Active control techniques are therefore sought which can stabilize a lean flame and prevent LBO. This involves developing detection methods to assess flame attributes and gauge LBO probability, actuation strategies to stabilize the flame, and control logic to complete the feedback loop.

The present work has resulted in the development of flame detection, dynamic modeling, margin estimation, actuation, and control techniques. Optical and acoustic methods have been developed or improved to detect two blowout precursor types – localized extinction pockets and brief, flame shape modulations. The latter behavior is studied in the context of swirling flow dynamics. The understanding of dynamic behavior allows the formulation of an empirical model that determines when flame modulations will occur. This model is then applied to detect both precursor types from the same sensor. Margin estimation methods have been developed that use the frequency of each precursor type to determine the probability of blowout.

It has been shown that the flame's blowout limit can be extended by redistributing fuel from the annular swirler to the central, premixed pilot. However, due to the emissions penalty, the control algorithm must command actuation only to maintain margin. Both rule-based and lead-lag control architectures have been developed and validated.

CHAPTER 1. INTRODUCTION

Control of pollutant emissions presents a considerable challenge for the gas turbine industry. Government regulations and public pressure are motivating companies to develop combustor designs that can provide the necessary power with minimal environmental impact. Thus, while combustors have traditionally used diffusion flames, newer designs are featuring premixed combustion. Specifically, lean, premixed combustion presents a way to burn fuel at lower temperatures and thereby minimize NOx formation by the thermal mechanism. The emissions benefit of lean, premixed flames have been demonstrated by premixed gaseous and prevaporized premixed liquid land based engines[1], and even in partially premixed liquid aero engines[2].

However, the stable sustenance of lean premixed flames is difficult in a turbine combustor environment. A premixed flame propagates when the incoming fuel and air mixture is rendered sufficiently reactive as a result of heat conducting and radicals diffusing upstream from the flame's reaction zone. At leaner conditions, the reaction rate is lower and flame propagation is affected. When the amount of heat and radicals produced by the reaction are insufficient for the given flow velocity, the flame will convect out of the combustor. This is known as lean blow out (LBO); the conditions at which LBO occur are called the lean flammability limit or lean blowout limit. A blowout is undesirable in land based turbines since it entails power loss and down times. In aircraft, a blowout can occur during the critical takeoff or landing phases of flight and cause catastrophic failures.

The flammability limits of premixed flames may be extended by enhancing the heat and radical feedback and/or decelerating the flow. Common techniques for doing

this include the use of bluff body flame holders, area expansions, swirlers, and secondary (pilot) flames. Clearly, each technique has drawbacks that affect the pressure loss and therefore impact the cycle efficiency. In the case of pilot flames, the concentrated 'hot' zone accelerates thermal NOx formation. There is therefore always a tradeoff between improving combustor stability margin and improving engine performance.

While the risk of blowout is elevated by the occurrence of velocity or mixture composition disturbances, the most evident risk arises from the transients induced by power setting changes. Figure 1-1 (a) presents a schematic of the main components of a gas turbine. When the turbine is throttled down, the fuel flow rate and therefore, equivalence ratio, are immediately affected. However, due to the rotational inertia of the turbine and compressor, the air velocity fed to the combustor decreases at a slower rate. As a result, the air fuel ratio reduces faster than the velocity. This causes the operating state to follow the top, broken line arc A-B in Figure 1-1 (b). The solid line in that figure represents the steady state operating points. Similarly, when the throttle is increased, the flame becomes richer before the velocity responds, and the engine's state moves along the bottom, broken line arc B-A.

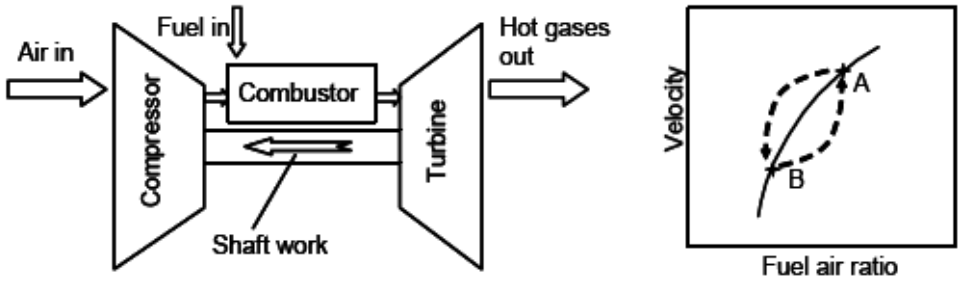

(a) (b)

Figure 1-1. (a) Schematic of basic gas turbine components. (b) Illustration of the gas turbine operating regime. The solid line represents the set of possible steady state operating conditions. The broken line describes the transient paths between two states, A and B.

The lean flammability limit is a function of both velocity and equivalence ratio for a given combustor design. Due to uncertainties in velocities and mixture

compositions, the limit cannot be defined precisely. Instead, a gray area separates the operating space between flammability and flame extinction regions (see Figure 1-2). For this reason, the combustor's operability regime, as denoted by the solid line, are designed to assure that the worst possible state (denoted as state 2) will remain at a tolerable distance from the blowout limit. This necessarily means that all other states (such as state 1) will lie in a regime that is overly conservative and suboptimal in terms of emissions. The improved safety is achieved only by operating richer (and hotter) and thereby forgoing some of the emissions advantage of lean, premixed combustion. In addition, power setting changes are scheduled conservatively so that the rate at which settings can be adjusted is limited. Ideally, the combustor should be operated in a manner that maintains the optimal safety margin at all power settings. The margin should be above a certain safety limit and below a performance limit for every power setting. For instance, the operating state at 1' in Figure 1-2 clearly produces lower emissions than state 1 and still has the same safety margin as state 2. An ideal transient would move the state of the combustor along a curve parallel to the blowout limit to insure that an optimal safety margin is maintained, with minimal emissions and guaranteed safety. In order to safely operate leaner, with greater operating flexibility and without emissions penalty, a control approach must be developed that would assess the probability of blowout in real time, and counter detected flow disturbances with rapid actuation that stabilizes the flame.

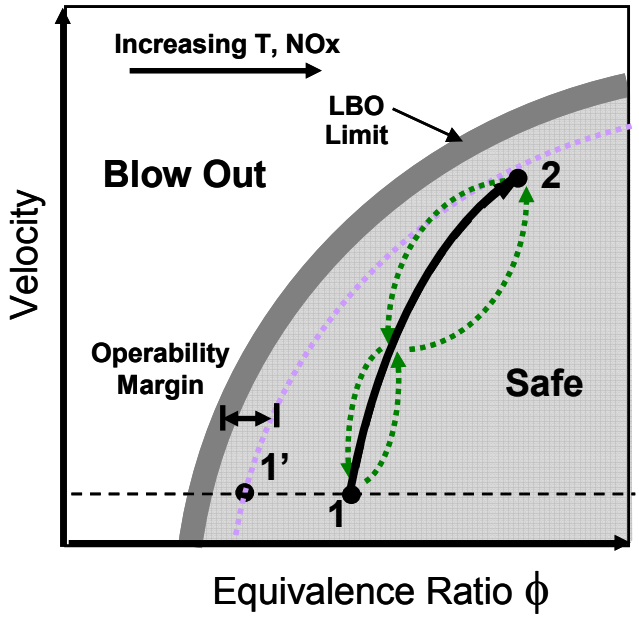

Figure 1-2. Detailed schematic of combustor operating regime and transients. The operating regime (solid line) is designed such that the worst possible state (2) lies immediately outside an operability limit. As a result, the other operating states (such as 1) are overly conservative.

Flame stabilization via active control presents a method whereby the flame status may be assessed and compensation commanded, both in real time and across a wide range of operating conditions. Active control minimizes the need for human intervention and can operate at faster timescales for better disturbance rejection and improved overall performance. An effective LBO control system must capably detect and mitigate impending lean blowout in a timely manner. Without rapid response, the flame can easily succumb to disturbances that occur with sufficient amplitude at high frequencies. Detection requires rapid and accurate determination of LBO probability. Furthermore, an understanding of flame behavior at lean conditions is required for effective controller design and optimization.

1.1 Present Understanding of Lean Blowout

Combustor stability can be characterized in terms of dynamic or static stability. Whereas dynamic stability concerns the coupling of unsteady heat release with the pressure and flow oscillations, static stability refers to the ability of a combustor to maintain a stable flame. Stability with regards to blowout and flashback is therefore considered static stability, and is dependent upon such parameters as temperature, velocity, and equivalence ratio of the reactive flow. Dynamic instability can trigger static instability due to the flow and pressure oscillations and localized static instability can trigger dynamic instability by creating nonuniformities in flow and temperature that 'oscillate' the reaction rate. While a great deal of work has been done to understand dynamic instabilities, less is known about static instabilities in complex combustors.

Prior studies have shed light on the characteristics of the combustor flow and combustion processes as the lean blow out limit is approached. For example, Nicholson and Field[3] noted large scale, low frequency flame pulsations as well as periodic detachment of the flame from its flame holder near the LBO limit. Chen and Goss[4] attempted to characterize the intermittent behavior near liftoff of various flames. They reported that the frequency appeared to be irregular but remained in the range of 100-150 Hz. Chao et al.[5] used acoustic excitation to stabilize a jet flame beyond its stability limit and then turned off the excitation to observe the blowout process. They found that the flame went through a pulsating phase before the onset of liftoff and eventually blowout. They also found that the process depended on the rate at which the conditions are changed towards blowout. They suggested that the high strain rates, much higher than the extinction strain rate, encountered by the flame base should be a prominent factor in the blowout process.

Lean flame pulsations have also been studied in the framework of nonlinear dynamics. Using a thermodiffusive model, Bayliss *et al.*[6] found pulsations in lean methane air flames that were characteristic of a Hopf bifurcation, i.e., complex eigenvalues crossing the imaginary axis. Gorman *et al.*[7] experimentally studied the behavior of a premixed methane flame near the extinction limit. They observed radial mode period doubling indicative of chaotic dynamics of a flame near LBO. However, these studies ignored aerodynamic effects and attempted to isolate flame from external influences.

The behavior of lean counterflowing flames, stabilized along a stagnation plane, formed the basis of several useful observations. In these types of flames, the strain rate was found to be an important contributor to extinction[8,9]. This finding verified the effect of strain rate on the transport of heat and species to the reaction zone. In other studies, a counterflow flame subject to acoustically driven forcing was found to withstand higher instantaneous strain rates than the critical values[10,11]. However, prolonged forcing weakened the flame; time to total flame extinction was found to be a function of the forcing amplitude and frequency. Evidence also suggests that the magnitude and rate of change of local, instantaneous strain rates are responsible for the occurrence of localized pockets of extinction and reignition that are typical in lean flames[12,13].

While the plane flame studies provide insight into fundamental flame behavior, gas turbine combustors are generally more complex, commonly employing swirl and area expansion to stabilize the flame. Black and Smith[14] assessed the large eddy simulation (LES) modeling of blowout of a low emission gas turbine fuel injector. They concluded

that the models used for spray and chemistry require improvements to predict near blowout behavior correctly.

The study by Muruganandam *et al.*[15] on swirl and dump stabilized premixed flames noted that the localized extinction 'events', characterized by 'dips' in the OH chemiluminescence signal, appeared more frequently as the flame became leaner. An example of such dips can be seen in Figure 1-3. These dips purportedly arose from the same localized, strain induced extinctions that were observed in the aforementioned plain flame studies.

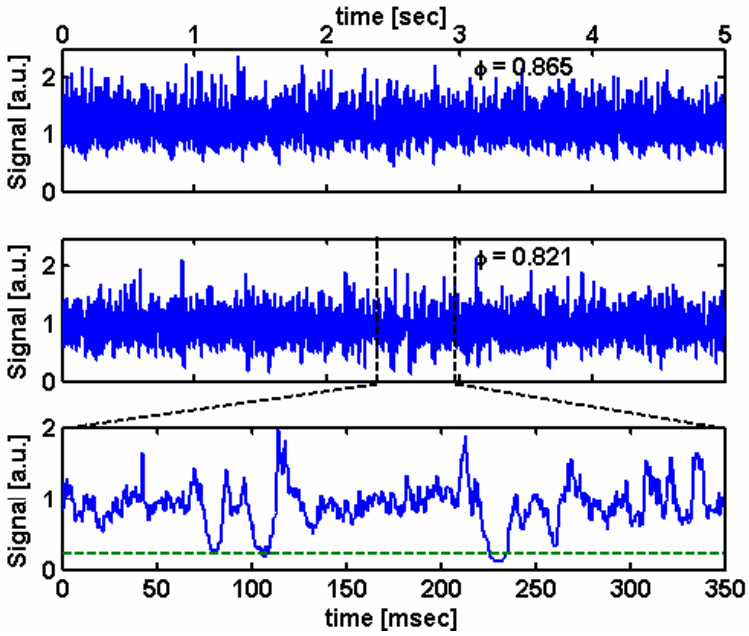

Figure 1-3. Example of localized extinction 'dips' in swirl and dump stabilized flames, as detected by OH chemiluminescence. Image adopted from Muruganandam.[15]

Muruganandam *et al.* further noted that the low frequency (~1 - 200 Hz) power content of both the optical OH (Figure 1-4 (a)) and acoustic (Figure 1-4 (b)) spectra was higher in lean flames. The authors postulated that this increase in low frequency power was due to a combination of localized extinction time scales (on the order of 10 ms) and the mean time between such events (on the order of 1s). It was further noted that as the flame became leaner, there was an increase in the frequency and duration of the localized

flame extinguishment events. While the authors examined both optical and acoustic approaches for detecting localized extinguishment events, the data processing required for the proposed acoustic method made it much slower than optical sensing. Nair and Lieuwen[16] continued the development of acoustic based sensing of localized extinction events. They demonstrated that when localized extinctions are present, the acoustic signal exhibits a repeated pattern, which can be extracted using a set of wavelets whose shapes are similar to the pattern.

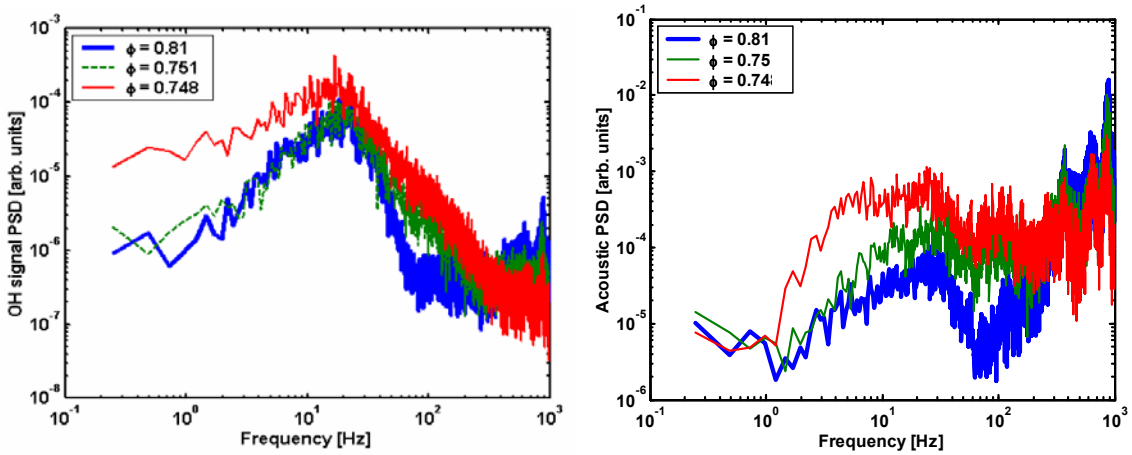

(a) (b)

Figure 1-4. Fourier spectra of the (a) optical and (b) acoustic signals from a premixed flame at different equivalence ratios. Images adopted from Muruganandam and Nair[16].

Fundamentally, extinction and blowout are different phenomena. While extinction indicates a loss of combustion, blowout occurs when a previously anchored flame convects downstream due to excessive flow velocities and/or insufficient reaction rates.

In his thesis, Muruganandam[17] examined the blowout dynamics of a swirl and dump stabilized flame. He postulated that as the flame gets leaner, the combustion in the inner recirculation region weakens, and its size diminishes. The flow patterns in the expanding vortex structure downstream of this region may aid in reestablishing the inner

recirculation zone to its former size. Alternatively, the pressure from the flow surrounding the recirculation zone may lead to its complete collapse. When this happens, the flame becomes less stable and may blow out.

1.2 Previous Blowout Mitigation Control Applications

A functional controller incorporates elements of sensing, processing and actuation. Thus, blowout mitigation control requires techniques to determine real time stability or blowout probability, actuation schemes which stabilize a lean flame, and processing and control approaches that reduce the blowout probability with rapid actuation.

Active control has been previously pursued as a means for NOx reduction in lean flames for gas turbine applications. A U.S. patent filed by Lucenko et al.[18] demonstrated the use of pressure, the time derivative of pressure, and shaft angular velocity to determine whether a blowout had occurred in a gas turbine. If indeed there had been a blowout, the fuel flow was shut off to prevent unburned fuel from flowing into the turbine. Another U.S. patent by Snyder and Rosfjord[19] featured a blowout proximity detection technique whereby total pressure oscillation amplitude was monitored. The presence of oscillation amplitude above a set threshold indicated the presence of lean instability, which occurred near the blowout limit. The corrective action was to increase fuel flow rate in order to avoid the operating regime where the oscillations were occurring. In both of these patents, the actual blowout margin was not monitored; instead, the pressure signal indicated whether or not the flame had already extinguished, or whether there was a lean instability.

More precise control of the combustor operating state for emissions reduction was demonstrated by Nakae *et al.*[20] A lean, premixed, prevaporized (LPP) combustor's equivalence ratio was varied based on CO emissions feedback. The controller varied the air distribution in the combustion chamber by modulating the air flow rate through an inlet downstream of the primary injection plane. Since monitoring the exhaust gases was a lengthy process, the method was intended for maintaining steady state lean operation.

The General Electric LM6000 and similar engines have demonstrated blowout avoidance control using measured and calculated fuel flow rate values.[21] When the inlet conditions appeared to approach a predetermined blowout limit, the flame temperature was increased by manipulating fuel flow rate. However, this had the effect of increasing overall engine power.

1.3 Overview of Research

Current blowout mitigation techniques require knowledge of inlet or outlet conditions to predict the blowout limit based on previous data. These methods, while effective, rely on accurate monitoring of either the equivalence ratio or the exhaust flow. The dependence on multiple sensors makes these approaches vulnerable to sensor failure. Furthermore, undetected changes to the flow or combustion process can reduce the reliability of previous data. In the case of exhaust gas monitoring, detection may not be rapid enough to prevent blowout from operating transients.

More recent work has focused on detecting distinct flame attributes near the flammability limit to estimate the stability margin. However, margin estimation that is only valid when margin is already near a critical state provides a limited scope for mitigation strategies. In such cases, the only course of action is a rapid, large amplitude

correction. There is no scope for smaller amplitude corrections to prevent the margin from becoming near critical in the first place.

The focus of this research is blowout mitigation in premixed, swirl stabilized flames through active control. This research work expands on past developments by investigating improvements in margin detection, signal processing, and control algorithms. Further, this work has investigated the dynamic behavior of lean flames and related precursor phenomena in order to enhance the determination of the margin and flame stability, and improve control techniques.

The thesis is presented in the following manner. Chapter 2 provides a fundamental background of premixed combustion; Chapter 3 describes the experimental facilities, including the combustor, sensors, valves, and processing hardware; Chapter 4 discusses precursor detection using acoustic and optical techniques; Chapter 5 describes the flame behavior and dynamics near the lean blow out limit. Blowout margin estimation techniques are covered in Chapter 6 and Chapter 7 presents actuation techniques that increase margin and stabilize lean flames. Blowout mitigation control is presented in Chapter 8 and Chapter 9 summarizes the conclusions and recommendations for future work.

CHAPTER 2. BACKGROUND

This chapter will cover the fundamental background material that will be implemented throughout the presented research. The first section will cover premixed flames and the second section will provide the fundamentals of control theory. The third section will delve briefly into vortex flow dynamics.

2.1 Combustion Fundamentals

The following section is an overview of combustion basics, as outlined in introductory textbooks[22]. The concepts of energy conservation and chemical kinetics introduced here will be used to explain lean, premixed flames in a swirl stabilized combustor in later sections.

2.1.1 Thermochemistry

Combustion is a chemical reaction wherein fuel combines with an oxidizer to generate high temperature products. The chemical energy stored in the fuel and oxygen molecules are used partly to form chemically stable combustion products. The remaining energy is given off as heat. The energy balance can be considered as follows: chemical energy of reactants = chemical energy of products + heat.

Energy conservation can be applied to fluid flow (and reaction) in a one dimensional duct. In such a system, enthalpy (H) is conserved for a constant pressure, adiabatic reaction. Gas turbine combustors are considered to fit this description since the pressure and heat losses are minimal compared to the overall cycle.

The net heat release from chemical reaction can be determined by considering the total enthalpy of the reactants at the reference temperature ($H_{reac}(T_{ref})$), and the total

enthalpy of the products at the same temperature ($H_{prod}(T_{ref})$). The difference in the two enthalpies, termed the 'heat of reaction', or $\Delta H_R(T_{ref})$, represents the heat energy available to raise the products to the final, adiabatic flame temperature. The adiabatic flame temperature is an idealized maximum possible temperature, since heat losses inhibit the flame from reaching the value.

Although a high flame temperature is beneficial for cycle efficiency, it increases NOx emissions as well. "NOx" refers to the sum of NO (nitric oxide) and NO_2 (nitrogen dioxide), which have long been identified as harmful atmospheric pollutants, contributing to acid rain production, photochemical smog and ozone depletion.[22,23] Burning of fossil fuels in power generation, transportation and industrial burners has been shown to be a major source of NOx in the world. NOx is primarily produced during combustion by the oxidation of atmospheric nitrogen in the high temperature regions (i.e., above 1850 K) of the post-flame gases where there is enough energy to overcome the high activation energy of the formation reactions of NOx. The chemical kinetics that describes this NO formation process is given by the thermal or extended Zeldovich[24] mechanism. Because of the harmful effects of NOx emissions, various government agencies have placed stringent restrictions on the operation of combustors in the industry.

2.1.2 Premixed Flames

Flames are characterized as one of two types: diffusion or premixed. Diffusion flames occur when a concentrated fuel source (i.e., jet) is injected into a stationary or moving oxidizer, which is usually air. The diffusion flame forms on the boundary where the fuel and oxidizer exist in stoichiometric proportions, and requires a premixed flame for stabilization. Premixed flames can occur in either fuel rich or fuel lean conditions, but not outside a set of flammability limits. Premixed flames stabilize when the heat and radicals generated from combustion are sufficient to overcome heat losses and ignite the incoming unburned mixture.

As a simplification, the premixed flame is segmented into 'preheat' and 'reaction' zones, as seen in Figure 2-1. Reactants first enter the thicker 'preheat' zone where their temperature is raised to a critical ignition value. In this region, the reaction rate is assumed negligible Lewis number (Le = $k/(\rho c_p D)$) is assumed to be unity. Turns[22] thereby derives the energy balance in the preheat zone:

$$\rho_u c_{p,u} S_L \left(T_{\text{int}} - T_u\right) = -k \left.\frac{dT}{dx}\right|_{\text{int}} \tag{2.1}$$

In Equation (2.1), ρ_u, $c_{p,u}$, and T_u are the unburned reactants' density, heat capacity, and temperature. S_L is the velocity at which the reactants approach the stationary flame. Alternatively, S_L is the speed at which the flame propagates into a stagnant unburned mixture. The subscript 'int' refers to quantities at the preheat and reaction zone interface. On the right side of Equation (2.1), k is the heat conduction coefficient and x is the spatial variable. The term is the net heat flux into the preheat zone due to conduction from the preheat zone. The temperature profile in the preheat zone is exponential, with the unburned reactant temperature at the upstream boundary.

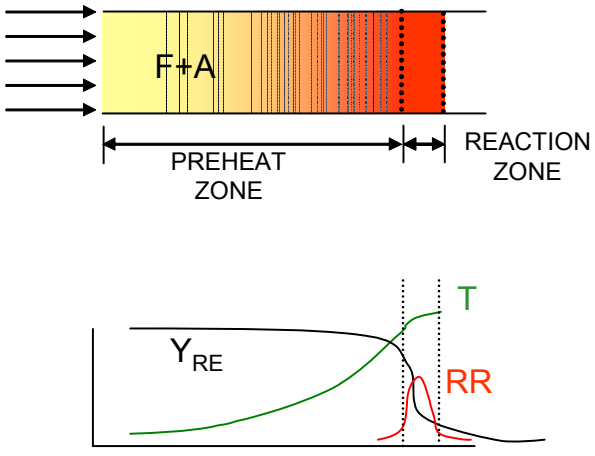

Figure 2-1. Anatomy of a laminar premixed flame in a one dimensional duct. A thicker preheat zone is followed by a compact reaction zone, where most of the reaction occurs. The bottom drawing shows spatial variations of reactant mass fraction (Y_{RE}), temperature (T), and reaction rate (RR).

The thinner 'reaction zone' is the flame region where the majority of reactions occur. In typical hydrocarbon premixed flames, this region may appear blue due to the luminescence of OH at 390 nm wavelength. Turns[22] derives the energy balance in this region by assuming that the first spatial derivative of temperature is negligible compared to the second spatial derivative. This yields,

$$\frac{d}{dx}\left(k\frac{dT}{dx}\right) = \Delta h_R \cdot RR \,. \tag{2.2}$$

Multiplying both sides of Equation (2.2) by $k \cdot dT$ and integrating, the following equation is obtained:

$$k\frac{dT}{dx}\bigg|_{\text{int}} = \sqrt{2\Delta h_R * \int_{T_{\text{int}}}^{T_b} RR \cdot k \cdot dT} \tag{2.3}$$

From Equation (2.3), it is evident that the conductive heat flux across the interface, as represented by the left hand side of the equation, is equivalent to the total rate of heat release from chemical reaction in the reaction zone. From Equation (2.1), the same conductive heat flux across the interface is responsible for raising the reactants' temperature from T_u to T_b in the preheat zone of the flame. It is clear therefore that the heat released from chemical reaction in the reaction zone is responsible for heating the incoming reactants in the preheat zone. Without this 'upstream' communication, the flame would be unsustainable in the flow.

The right hand side of Equation (2.3) can be equated with the left hand side of Equation (2.1), and then simplified with the assumption that the interface temperature is approximately equal to the final 'burned' temperature. Furthermore, the conductivity, k, can be assumed constant and the temperature integral of reaction rate from T_{int} to T_b can

be considered equal to the same integral from T_u to T_b (since RR in the preheat zone is neglected). Turns thereby derives the following equation for laminar flame speed:

$$S_L = \sqrt{\frac{2\nu'_f}{\rho_u Y_{f,u}} \overline{\alpha} * \overline{RR}} \tag{2.4}$$

In the above equation, overbars indicate mean values, averaged over the flame. α is the thermal diffusivity ($\alpha=k/(\rho c_p)$), ν_f' is the stoichiometric coefficient of fuel on the reactant side of a representative reaction. $Y_{f,u}$ is the fuel mass fraction in the reactant mixture, and RR is the reaction rate.

Flow velocity, mixture equivalence ratio, and upstream temperature, along with fuel type affect the fundamental flame characteristics. For typical hydrocarbon flames, the chemical reaction rate peaks at slightly fuel-rich conditions, near the equivalence ratio values of 1.0 – 1.1. Correspondingly, the flame temperature and flame speed (S_L) are maximum at those conditions as well. As mentioned earlier, a flame is no longer sustainable when the heat released from reaction cannot overcome losses to raise the incoming reactants to the critical ignition temperature. In general, a premixed flame cannot exist outside a set of rich and lean flammability limits. At these limits, the heat and radicals produced in the reaction zone are insufficient for the flow, and the flame is convected out of the combustor.

The flame speed can also be affected by flow related heat and species transfer away from the reaction zone in a non-normal direction. Thus, the flow field can either enhance or inhibit the flame speed; this is often called the stretch/curvature effect.[8,25]

While premixed flames have a propagation speed, nonpremixed, diffusion flames do not. For reasonably fast chemistry, they burn in regions of near stoichiometric mixture

fraction. It has been shown that jet diffusion flames are stabilized by a small premixed flame near the lip of the jet burner.[26,27] Thus, the diffusion flame can also propagate due to propagation of the anchoring premixed flame. In contrast, premixed flames are not constrained to burn at stoichiometric conditions like diffusion flames. Such flames can sustain a reaction across a finite range of mixture conditions and produce a corresponding range of flame temperatures.

2.2 Flame Stabilization

A premixed flame will stabilize along the contour where the component of velocity normal to the flame front is equal to the local laminar flame speed. For instance, the flame is stationary in a one dimensional duct only when the (assumed) uniform flow velocity matches S_L. In an open tube, such as a Bunsen burner with exit velocity $v_e > S_L$, a conical flame with half angle θ equal to the arccosine of S_L/v_e, forms along the surface where the velocity component normal to the flame is equal to S_L. Due to the viscous dissipation of velocity near the tube wall, there is a critical radius r^* where $v_e(r^*) = S_L(r^*)$ and the flame appears flat; this is the flame anchoring point. As the velocity increases, the anchoring point moves downstream and $S_L(r^*)$ decreases due to the entrainment of ambient air into the reactants. Eventually, $S_L(r^*)$ will be too low, the anchor will vanish, and the flame will blow off.

Therefore, stabilizing a flame in a high velocity flow, such as a gas turbine combustor, is a considerable challenge given the range of operating conditions. Current combustors utilize recirculating flow, such as that resulting from area expansions, swirl flows, or bluff bodies, to stabilize a flame in high velocity. In addition, fuel preheating, pilot flame, and plasma injection techniques have been utilized as well.[28,29,30] In all

cases the strategy involves either increasing the flame speed by making the inlet mixture more reactive, or decelerating the flow such that the flame can stabilize in the low velocity regions.

Well-stirred reactors have been used to model the effect of recirculation zones, and the approach has been quite successful in predicting trends in stabilization limits and their relationship with combustor flow rate. Further improvements to this model were achieved by the partially stirred reactor, which simulates imperfect mixing in practical combustors.[31] A system of well-stirred reactors and plug flow reactors has also been used to model complex combustors to simplify their characterization. [22]

The space constraint in many practical combustors restricts the length of the combustion chamber. Adding swirl to the flow increases the residence time since the fluid now takes a helical path instead of straight path through the combustor and thus helps ensure higher combustion efficiency within a shorter length combustor. Addition of a sudden expansion in the flow area (called a dump region) decreases the flow velocity and also adds a corner recirculation zone which provides a feed back of hot products and radicals into the reacting flow. The combination of swirl and area expansion in combustors is the most common stabilization method used in modern gas turbine combustors. Swirling flows are characterized by the strength of the swirl, given by swirl number, *S*, defined as the ratio of tangential momentum to the axial momentum of the flow at the inlet of the combustor. Flows with high swirl numbers have the added advantage of vortex breakdown and have an inner recirculation zone, which again helps in stabilizing the flame.[32]

2.2.1 Swirl Flow

In order to develop an understanding of a swirl stabilized flame, it is necessary to examine the fundamentals of swirling flows. A swirling, or vortical flow may be found in naturally occurring vortices such as those formed in the wake of an aircraft wing, or in a typhoon or tornado. Swirl flows can also be induced with vanes or rotating walls. In combustors, swirl is used to enhance mixing and stabilization.

A vortex flow can exhibit a variety of flow structures depending on such parameters as the Reynolds number (*Re*), area expansion ratio, and the ratio of tangential to axial momentum (or swirl number, Ψ).[32] At low values of *Re* and Ψ, the flow remains columnar (i.e. devoid of recirculation). As these parameters increase, the adverse pressure gradient generated by the centripetal forces can cause recirculation zones to appear. In such cases, the axial velocity will stagnate and possibly reverse in a region 2-4 diameters (measured in terms of inlet diameter) from the inlet. This phenomenon is known in the literature as vortex breakdown. The main types of vortex breakdown are depicted in Figure 2-2. The illustrations on the left show the streamlines while the images on the right exhibit the flow dye visualizations.

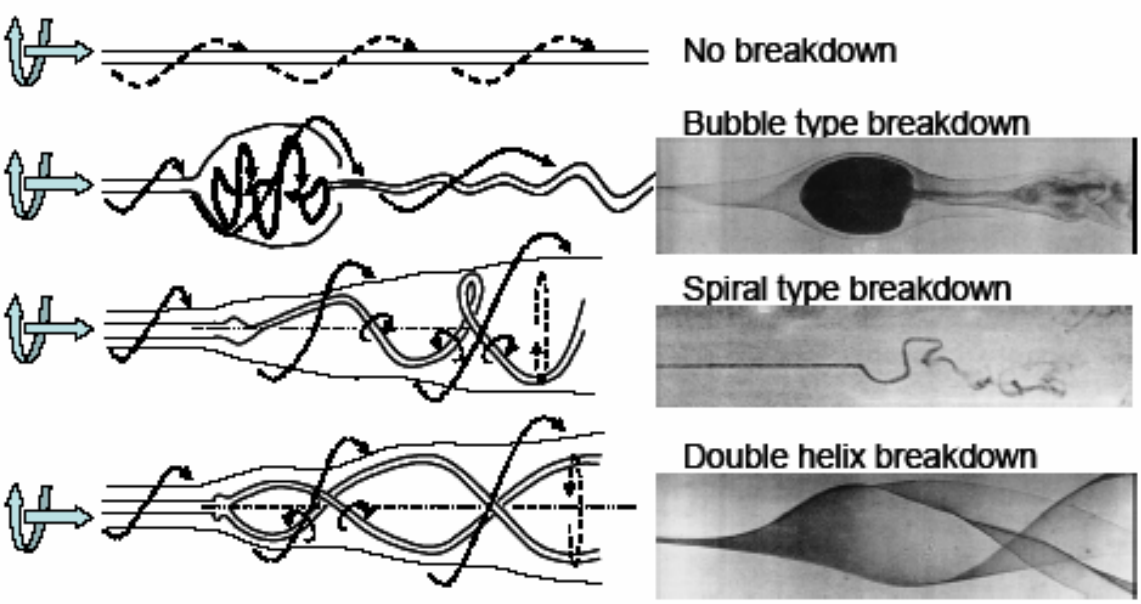

Figure 2-2. Common vortex breakdown types, shown as an illustration (left) and as flow dye visualization (right). Images adopted from Sarpkaya[33] and Muruganandam.

While there are many known types of vortex breakdown, the most common is the bubble-type breakdown, shown in Figure 2-3. Essentially, a momentum deficient 'bubble' forms several diameters downstream of the inlet. The surrounding flow surpasses the bubble as if it were a three dimensional bluff body in the flow. Within the bubble, the flow direction may reverse, with fluid being drawn in from the downstream side. The bubble itself precesses, and is also known as the precessing vortex core. In some combustion studies, the bubble is called the inner recirculation zone, or IRZ, distinguishable from the outer recirculation 'dump' region of an area expansion.[17]

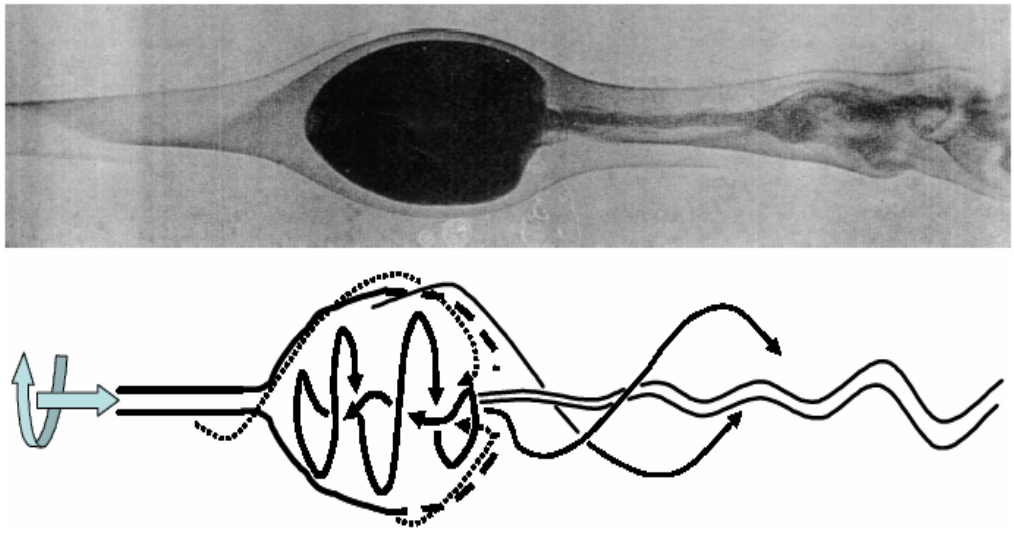

Figure 2-3. Flow dye visualization (top) and pathlines (bottom) of a bubble-type vortex breakdown. Images adopted from Sarpkaya and Muruganandam.

Downstream of the bubble, the 'tail' region may form a spiral structure. Novak and Sarpkaya[34] demonstrated that for higher Reynold's number flows (up to Re = 3×10^5, with tube diameter as the characteristic length) the momentum deficient 'bubble' region is immediately followed by an axisymmetric cone of highly turbulent, spiraling flow. This flow is shown in Figure 2-4 using both 1/30 second and 6 nanosecond exposure times. It was clear that the turbulent structures behind the bubble have a spiral shape when imaged with sufficiently short exposure times.

Transitions between columnar, vortical flow without breakdown and different types of vortex breakdown structures in non-reacting flows have been studied both experimentally and numerically by varying inlet velocity and swirl conditions.[35,36,37] Furthermore, for a set of Reynolds numbers, multiple vortex breakdown types are possible for the same swirl number.[38] Analytical studies by Wang and Rusak suggest that the favored configuration of a swirling flow (whether vortical and columnar or a vortex breakdown state) corresponds to a global minimum in flow energy. For certain

flow conditions, another minimum may exist with an alternate flow configuration. The ability of the flow to transition between alternate states depends upon the magnitude of the flow disturbances compared to the excess energy required for transition.

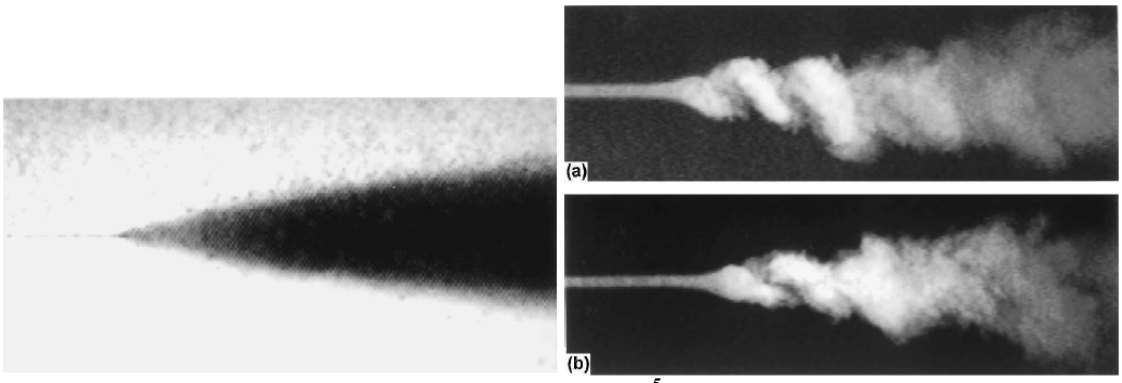

Figure 2-4. Conical/spiral vortex breakdown at Re=1.2x10^5. Images shown for exposure times of 33ms (left) and 6ns (right), adopted from Novak and Sarpkaya.[34]

Figure 2-5 depicts the energy diagram developed by Wang and Rusak. Each curve in the figure corresponds to a different induced swirl rotation rate. The total momentum energy (E) is shown on the y-axis and the stream function (ψ) is shown on the x-axis. For a particular rotation rate, the flow will favor the state or states at minimum energy. These stationary points correspond to the steady state solutions of the Squire-Long Equation:

$$\psi_{yy} + \frac{\psi_{xx}}{2y} = H'(\psi) - \frac{I'(\psi)}{2y} \tag{2.5}$$

In the above equation, H is the total head function, $H=p/\rho + (u^2+ v^2+ w^2)/2$, where p is the dynamic pressure, ρ is the density and u, v, and w are the radial, circumferential, and axial velocity components. $I=r^2v^2/2$ is the extended circulation function, and r is the radial position.

In Figure 2-5, the set of stationary points on the dashed line represent solutions where the flow is columnar, i.e., without vortex breakdown. For subcritical rotation rates

($\omega < \omega_0$), the columnar state is the favored, minimum energy configuration; perturbations may increase or decrease the swirl number (and corresponding stream function) momentarily but the flow will rapidly return to the columnar configuration in steady state. As the rotation increases beyond an initial point ($\omega_0 < \omega < \omega_1$), a local minimum appears at a point corresponding to vortex breakdown. At this state, smaller perturbations can cause the flow to transition to the vortex breakdown state. Upon further increase of rotation ($\omega > \omega_1$), the local minimum becomes a global minimum.

$$E(\psi) = \int_0^{x_0} \int_0^{1/2} \left(\frac{\psi_y^2}{2} + \frac{\psi_x^2}{4y} + H(\psi) - \frac{I(\psi)}{2y} \right) dy\,dx.$$

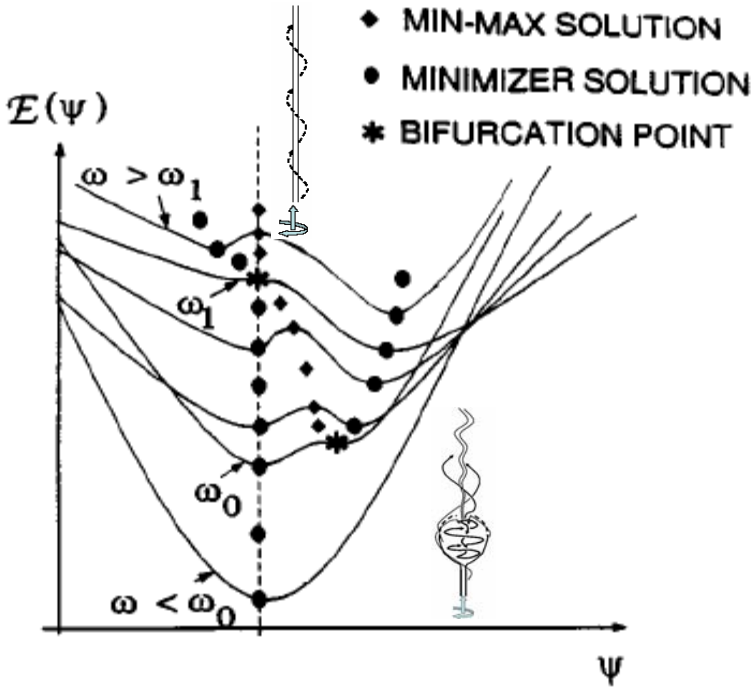

Figure 2-5. Energy diagram depicting favored modes of a nonreacting flow with varying amounts of angular rotation (ω). The x-axis represents the stream function, Ψ, and the y-axis is the total momentum energy of the flow. When the rotation reaches a critical value ($\omega=\omega_0$), the vortex breakdown flow emerges as an alternate flow configuration. At sufficiently high rotation ($\omega>\omega_1$), the breakdown state is the only stable configuration. Image adopted from Wang and Rusak.[36]

2.2.2 Swirl Stabilized Flames

Swirling flow with sudden expansion can produce several flame shapes based on the heat release, swirl and velocity in the combustor.[39] The observed average flow fields in cold and hot flows are different due to the dilatation from heat addition. The presence of the swirl-induced vortex core is suppressed by combustion and the dilatation, which makes the inner recirculation zone (IRZ) smaller for the case with combustion.[40,41] It is also observed that the turbulent kinetic energy and the velocity fluctuations are increased substantially due to combustion.[42]

Among the different types of vortex breakdown, the 'bubble type' vortex breakdown structure is most commonly found in gas turbine combustors, typically induced by swirl vanes and area expansion. The flow characteristics of the resulting 'swirl and dump stabilized' flame enhance the flame's stability. First, the momentum deficient 'bubble' behaves like a bluff body by decelerating the centerline flow, and redistributing momentum from the axial to the radial direction.[43,17] Second, the heat and radicals retained in the bubble increases the temperature and reactivity of the inlet mixture. Third, the turbulent structures behind the bubble enhance mixing and, thereby, the combustion chemistry.

Recent work has concentrated on understanding the dynamics of this complex, reacting flow field using both numerical and experimental methods. Although the mean flow shows a central toroidal vortex, the instantaneous flow field is observed to have smaller vertical structures, which help in mixing.[44] Adding heat release to a near critical swirling flow has been analytically shown to cause a decrease in the critical swirl for breakdown.[45]

2.2.3 Flame Behavior Near Blowout

The study of flame behavior near blowout has been mostly confined to the experimental realm. One of the first detailed works on loss of stabilization of flames was by Lewis and Von Elbe.[46] They found that the velocity gradient at the wall/lip of the burner was important in determining the stability of the flame. Several researchers following their lead studied the loss of static stability of flames. Jet flames and bluff body flames were observed to lose their stability in an intermittent, sporadic and non-symmetric fashion.[3,47] The flames generally pulsated at a low frequency (~10-200 Hz) for several seconds prior to blowout.

It is generally accepted that high magnitudes of strain are a cause for flame extinction.[8,9,13] Whereas blowout implies the convection of an intact flame away from the flameholder, extinction is the quenching of the flame itself. In counterflow flames, fluidic strain rates were found to be responsible for localized pockets of extinction and reignition. However, brief exposures to elevated strain rates did not result in flame loss. When subject to induced, cyclical forcing, the flame could withstand brief periods of supercritical strain rates over several cycles before extinction. Time to extinction was a function of both the forcing frequency and amplitude.

Many turbulent flames develop small holes at random locations that grow in size until the whole flame is extinguished.[48] In turbulent flow fields these local holes of the flame may be a result of strain rates induced by turbulent perturbations. In a turbulent flow these holes would appear and disappear at random locations depending on the strain field at any instant. In more complex flames, e.g., gas turbine combustors, the flame extinctions and reignitions appear to oscillate between two flame shapes prior to blowout.[49,50,51]

Muruganandam examined the dynamics of a swirl and dump stabilized flame near blowout. He noticed that as the flame got leaner, the combustion in the bubble region weakened, and the bubble got smaller. The diminishing bubble would then collapse under pressure from the surrounding flow, and the core flow would transition from a bubble-type vortex breakdown to a double helical-type vortex breakdown, which corresponded to the 'tornado' mode in the swirl stabilized flame. This flow transition is illustrated in Figure 2-6. However, double helical vortex breakdown, while studied numerically[52], has been considered extremely rare in practical flow structures.

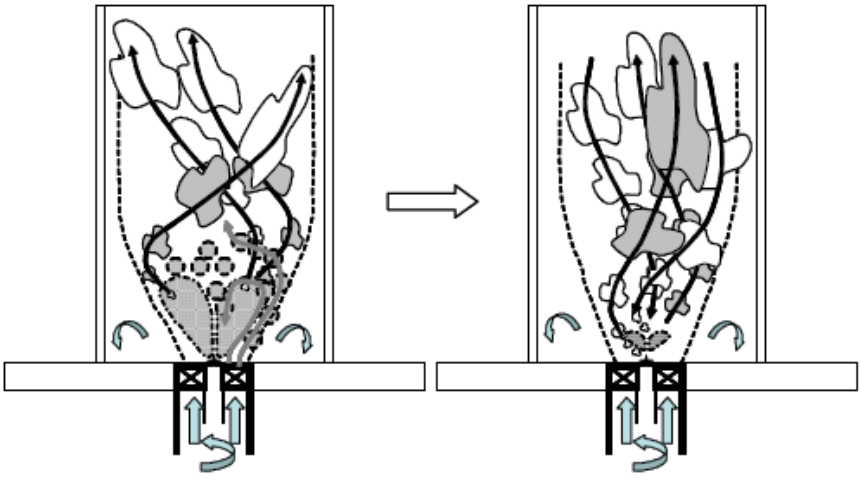

Figure 2-6. Illustration of the flow transition wherein the inner recirculation bubble (shown in gray) diminishes. The resulting flame shape transition is the mechanism for blowout in a swirl and dump stabilized flame. The helical flow structure on the right has both downstream and upstream flow paths. Images adopted from Muruganandam.

CHAPTER 3. EXPERIMENTAL FACILITIES

This chapter describes the experimental setup on which the experiments were conducted over the course of this study. The utilized combustor was a laboratory simulator of a premixed, swirl stabilized turbine combustor, and is described in the first section. The valves and circuitry utilized for fuel redistribution are described in the second section. The third section discusses the acoustic and optical sensors used for diagnostics. The hardware utilized for data acquisition, signal processing, and control is the subject of the fourth, and last, section.

3.1 Combustor

The experiments were performed in an atmospheric pressure, premixed, swirl and dump-stabilized combustor. The same combustor configuration and sensors have been used in previous lean blowout studies.[15,16,71] The combustor was designed to simulate a lean, premixed gas turbine combustor with a swirling premixer section, as seen in Figure 3-1.

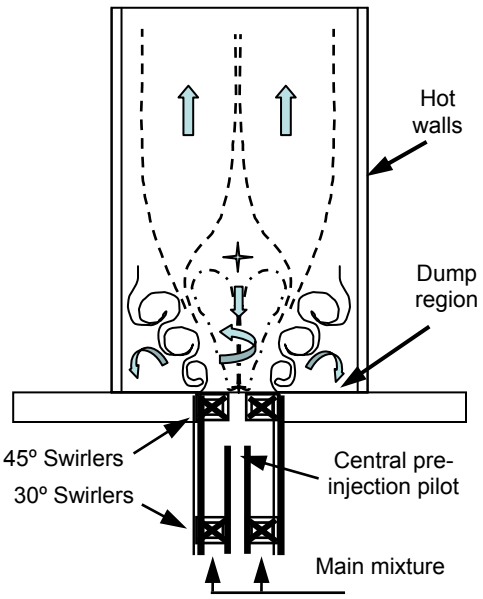

Figure 3-1. A schematic of the utilized combustor.

The inner diameter and length of the uncooled combustor were 70 mm and 127 mm, respectively. The quartz combustor side walls and enabled optical access to the swirl and dump stabilized flame. In some experiments, the combustor length was extended to 243 mm. The swirl section was comprised of two sets of vanes, one upstream at 30º, followed by a 45º swirl 100 mm downstream at the combustor inlet. The swirlers, as illustrated in Figure 3-2, were housed in a 23 mm inner diameter tube, and the nonreacting flow entering the combustor had a theoretical swirl number of 0.66[53]. For the reported studies, a gaseous methane and air mixture was sent through the annular, 'main mixture' duct, while dilution air flowed through the 'pilot' tube.

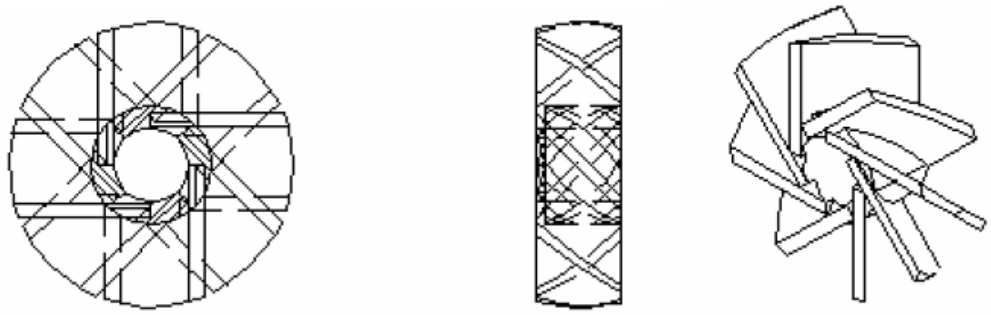

Figure 3-2. Drawing of the swirlers used in the combustor.

The bulk average axial velocity in the combustor remained around 2-3 m/s under cold conditions. Assuming complete combustion, the average axial velocity of the product gases would be ~10-15 m/s. Under nominal operating conditions, a gaseous methane and air mixture was sent through the annular, 'main mixture' duct, while dilution air flowed through the 'pilot' tube. For an equivalence ratio of 0.76, the fuel flow rate was .0008 kg/s, and the air flow rate was .02 kg/s. Approximately 3% of the total mass air flow rate was directed toward the pilot.

As conditions in the combustor were varied, the flame shape assumed one of several of possible configurations. In particular, Muruganandam documented three distinct flame shapes, as shown in the photographs and illustrations of Figure 3-3. At sufficiently high equivalence ratios, two flames were visible; a primary flame with a 'v-shaped' base centered near the swirlers and a secondary torus-shaped flame in the dump region around the primary flame's base. This compound flame was labeled as the 'Compact Flame' in Figure 3-3 (a).

At conditions closer to blowout, only the primary flame remained, corresponding to the 'V-shaped Flame' in Figure 3-3 (b). When the flame transitioned between the

‘Compact Flame’ and ‘V-shaped Flame’ modes, a secondary, torus flame pulsed, vanishing and reappearing at random intervals.

At sufficiently lean conditions, a thin, elongated tornado-shaped flame appeared. This flame shape corresponded to the ‘Tornado Flame’ image in Figure 3-3 (c). When the combustor length was 127 mm, the tornado flame was not sustainable for more than several tens of milliseconds. However, in a longer, 243 mm combustor, the tornado flame could persist indefinitely. At certain intermediary conditions, the flame would ‘pulse’, randomly shifting from the v-shaped flame mode to the tornado flame mode and return immediately. If the tornado persisted beyond a certain critical timescale, the flame would either blow out (as in the 127 mm combustor) or begin favoring the ‘stable’ tornado configuration (as in a longer, 243 mm combustor).

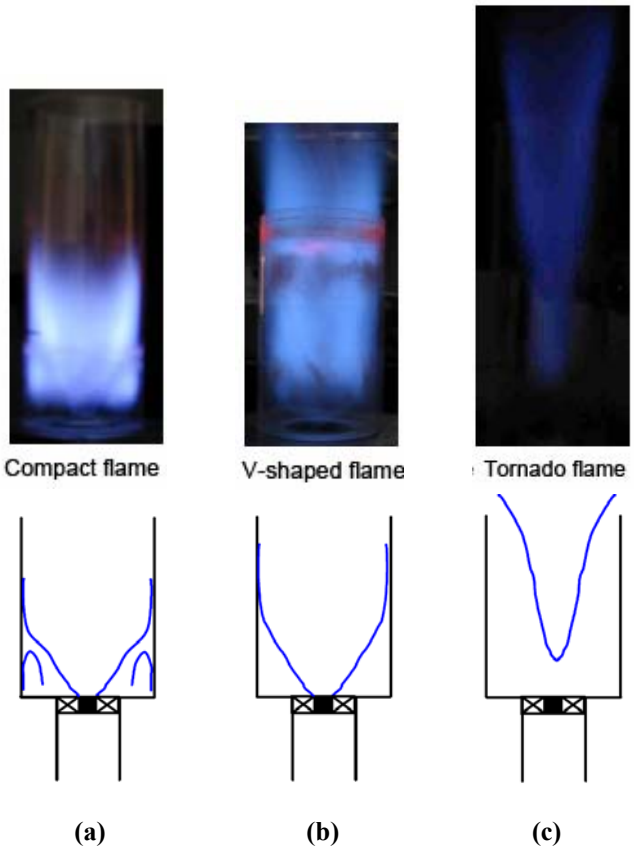

Figure 3-3. Photographs of different flame configurations in the combustor, with illustrations of the approximate flame shape. Images adopted from Muruganadam.[17]

3.2 Fuel Split Valves

The actuation strategy adopted for this study was to redistribute a fixed, total fuel flow rate between the annular swirler ring and the premixed central, pre-injection pilot. Figure 3-4 shows a schematic of the fuel and air flow to the combustor via the splits between main and pilot flow. The air flow split was fixed while the control valve manifold governed the fuel split. A set of choke points ensured that pressure oscillations did not travel upstream to disrupt the split ratios.

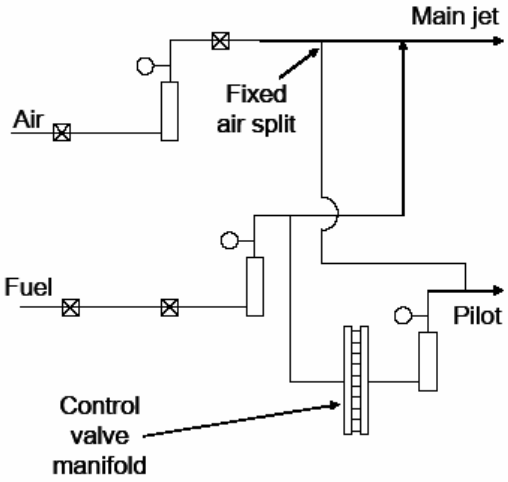

Figure 3-4. A schematic of the air and fuel flow to the combustor. The air flow split was fixed while fuel split was governed by the control valve. The drawing shows the choke points (boxes), flow meters (rectangles) and pressure gauges (circles).

The fraction of fuel that was redirected to the pilot was governed by a manifold of ten Asco Scientific solenoid valves, as shown in the top part of Figure 3-5. Each solenoid 2-way valve was normally closed, and required 24 V to open for pressures up to 110 psi (76 kPa). The orifice size was 0.64 mm. The command signal from the control computer was 5 V DC at 30mA, which activated a set of relay transistors contained on a Panasonic AQV214E, MOSFET relay chip. The relay circuit for one valve unit is shown in the bottom schematic of Figure 3-5. The typical turn on time was 0.5 msec, and the typical turn off time was 0.05 msec.

While the valve response time was rapid, a single valve could only be commanded open or closed, and the maximum flow rate through a single valve was very small (approximately 2% of total fuel flow rate). For this reason, a set of ten valves were used, and operated with pulse width modulated (PWM) commands. For instance, the command for 8% fuel split would be divided among five valves. Three valves would remain open full time (100% duty cycle) while the remaining two valves would be given

a 51% duty cycle. The additional 1% duty cycle command compensated for the response time. Although 8% fuel split could also be achieved with 4 valves at 100% duty cycle, incrementing the split command by .2% (from 8% to 8.2%) would have meant that the 5th valve would be required to produce an unachievable 1% duty cycle.

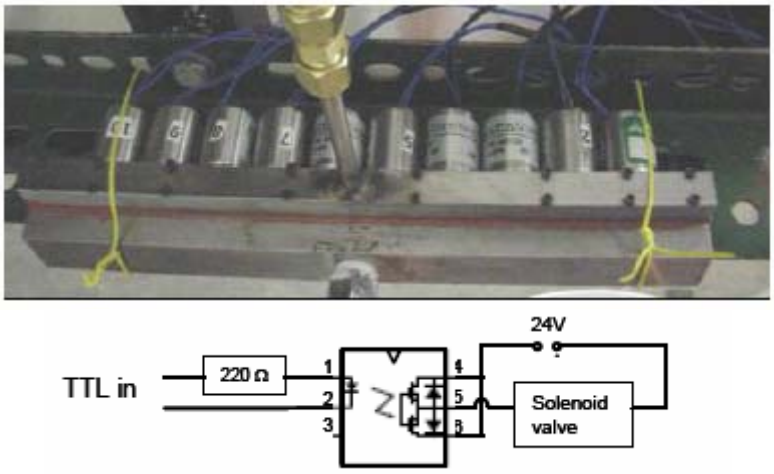

Figure 3-5. Photograph of the manifold of ten solenoid valves used to control fuel split (top). A transistor relay circuit (below) activated the individual, normally closed valves.

The commanded fuel split to the pilot ranged from 0% to 20%, with 2% allocated for each valve. The pilot equivalence ratio depended upon the fuel split. A split of 10% corresponded to a pilot equivalence ratio of approximately 3.5 and a 20% split corresponded to a pilot equivalence ratio of about 5. Although the pilot was considerably richer than the main flow, the overall combustor equivalence ratio remained constant regardless of the fuel split.

3.3 Sensors

One primary objective of the study was to determine whether a flame's proximity to blowout could be monitored by examining the flame itself. Both optical and acoustic sensors were used to detect flame attributes. Optical methods were a direct measure of

the flame luminosity within a specified field of view. However, optical access is not available in many gas turbines. Acoustic techniques, while more susceptible to noise, were, however, more practical for existing platforms.

3.3.1 Acoustic Sensor

Acoustic oscillations were measured with a calibrated, Bruel and Kjaer type 4191 13 mm condenser microphone that had a flat frequency response up to 40 kHz. The microphone dynamic performance was similar to that of pressure transducers found in actual engines. Although the microphone employed a stainless steel diaphragm and a protective grid, it was inoperable beyond temperatures of 450K. High temperatures up to 2000K and highly corrosive exhaust gases disallow flush mounting of standard microphones to combustor walls. Therefore, the microphones were typically located in the acoustic far field, ~61 cm from the combustor exit at ~90^{o} from the flow axis.

In the acoustic studies presented by Nair and Lieuwen[16] with identical apparatus, flame noise exhibited little directivity, and results demonstrated weak dependence upon the microphone location. The principal exception to this occurred when the microphone was placed in the combustion chamber exhaust. In that case, hydrodynamic pressure fluctuations substantially increased background noise levels.

The acoustic signal provides a global gauge of pressure oscillations that may be useful in determining flame characteristics. Furthermore, acoustic oscillations are proportional to the rate of heat release in the flame. However, changes in background noise level can potentially result in false readings. Hence, signal processing becomes integral to any acoustic based sensing approach.

3.3.2 Optical Sensors

In investigating flame shape oscillations and local extinctions, optics based sensing methods are preferable for their localized nature and high degree of accuracy. Flame chemiluminescence is directly related to the local chemical reaction processes[54,55]. The primary sources of chemiluminescence in lean hydrocarbon flames are OH (ultraviolet emission around 308 nm), CH (visible emission around 430 nm) and CO_2 (broadband ultraviolet and visible emission)[56,57,58].

Photomultiplier transducers (PMT's) were used to optically detect flame luminosity. Such devices produce a current when light impinges on a charged substrate. Electrons are released via the photoelectric effect, and are subsequently accelerated through a series of electric fields.[59] For most experiments, light was collected through a fiber optic cable oriented horizontally approximately 57mm downstream of the combustor inlet. Figure 3-6 shows the location of the optical fiber, designated 'mid', in relation to the combustor. The values for h_{Mid} and d_{Mid} were ~57mm and ~25 mm respectively.

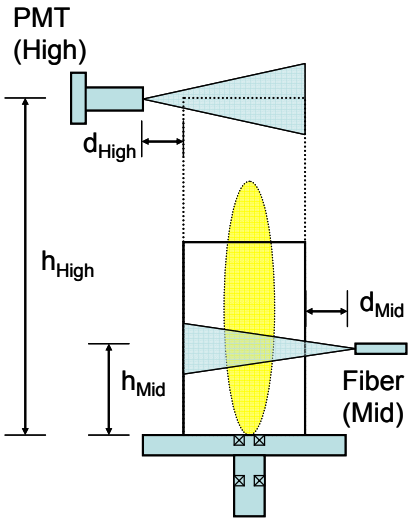

Figure 3-6. Diagram depicting the optical sensor locations.

The fiber optic collection setup employed a 365 μm diameter fused silica optical fiber. The fiber had an acceptance cone half-angle of about 12º. The collected radiation passed through an interference filter, centered at 308 nm and with a full-width-half-maximum (FWHM) of 10 nm, which corresponded to the primary spectral region for the OH $A^2\Sigma$-$X^2\Sigma$ electronic transition. The collected OH emission was detected by a miniature, metal package PMT (Hamamatsu H5784-04). This PMT had a built-in amplifier (bandwidth of 20 kHz) to convert the current to voltage and operated from a 12 VDC source.

A second PMT, placed further downstream and labeled 'high', was used in some experiments to study flame shape modulations. The 'high' sensor detected light when the flame shape transitioned from base-stabilized to a thin, lifted configuration. This sensor was unfiltered, since the objective was to detect any type of light from a flame burning in a darkened room. An aperture restricting cover with an opening of 2 mm was placed on the PMT to limit its field of view.

3.4 Acquisition, Processing and Control Hardware

Data acquisition and signal processing were critical elements of the overall system. Brief descriptions of the overall layout and the hardware involved will be presented here. Details concerning filters and control algorithms will be presented in later chapters.

Figure 3-7 presents a schematic of the signal and fluid flow of the closed loop combustor system. During the control experiments, the air flow rate was externally perturbed by the operator to simulate disturbances. Near blowout, the flame would exhibit precursors, which were detected by the sensor. The processing and control

algorithm used the sensor signal to determine the required fuel split actuation, and sent an appropriate pulse width modulated command to the valve manifold. The valve manifold then redirected a portion of the total fuel into the center pilot port.

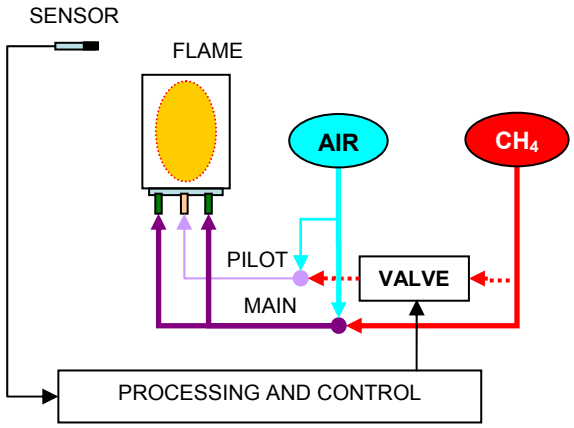

Figure 3-7. A schematic of the air, fuel, and signal flow. The air flow split was fixed while fuel split was governed by the valve.

Figure 3-8 shows the various hardware components involved in signal acquisition and processing. For all reported experiments, data was sampled at 10 kHz using a 2 bit National Instruments A/D board connected to a computer running LabVIEW (denoted as DATA ACQ in the figure). Anti aliasing filters were set up to lowpass at 4.5 kHz using a 4th order Butterworth filter. The valve commands were issued by a dedicated control computer running QNX real time operating system with a Power DAQ I/O board running at 10 kHz. The control logic produced a valve command that switched transistor relays and activated each valve.

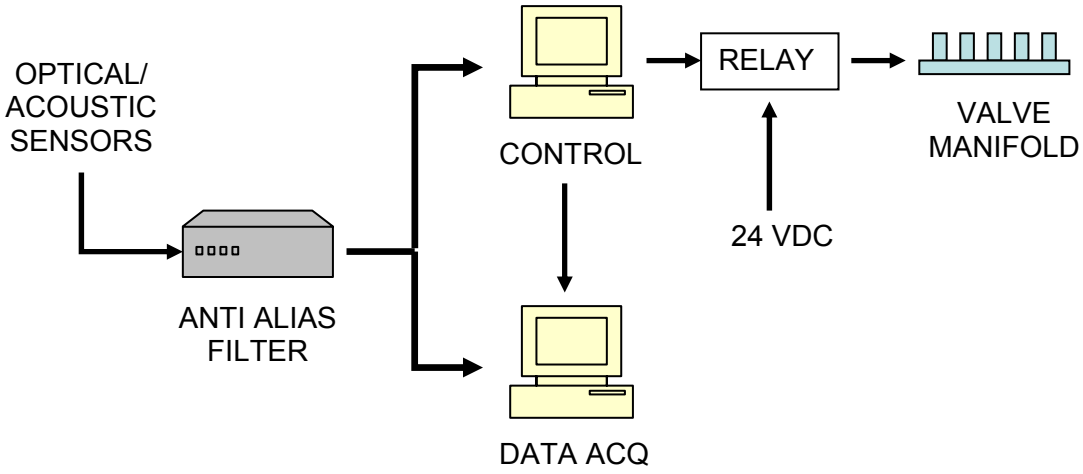

Figure 3-8. Schematic of signal processing, acquisition, and control hardware.

CHAPTER 4. FLAME DETECTION

This chapter describes the various optical and acoustic methods employed to detect flame attributes, such as blowout precursor events. Sensing forms a critical component of any control strategy, and is particularly significant for blowout avoidance. Detection techniques are also easily portable between different types of combustors, and allow empirical characterization of flame behavior near blowout.

4.1 Optical Sensing

Optical sensing techniques are generally methods that rely on the luminosity of the flame. While there are a number of sources for electromagnetic radiation from a combustor, the source most directly connected to the combustion reactions is chemiluminescence. This radiation is from (electronically) excited molecules that are produced by the chemical reactions and which can relax to lower energy states by emitting light. Since the intensity of emission is generally proportional to the chemical production rate of the particular molecule, the chemiluminescence intensity can be related to chemical reaction rates.[60] For this reason, chemiluminescence has been used previously as a rough measure of heat release rate and even equivalence ratio.[61-63]

The primary chemiluminescent species of interest in a hydrocarbon flame are electronically excited OH, CH and C_2 radicals. In lean hydrocarbon flames, OH tends to be the strong emitter, followed by CH with little C_2 emission. As the equivalence ratio increases, the CH and C_2 emission bands become stronger.[64,65] This work used chemiluminescence from OH (near 308 nm) for detecting lean blowout since this emission is the strongest at near LBO operating conditions. The UV spectrum produced

by OH also has very little interference from blackbody radiation (from walls or particles) and thus has good observability.

Since chemiluminescence is directly related to (some) chemical reaction rates, it can provide information on the presence and strength of the combustion process in a specific region of the combustor. This approach is appropriate for monitoring the flame stability and LBO. Also, it inherently has a fast time response providing fast detection of flame instability events. Finally, optical sensing in general is applicable to a combustor, for example, using fiber optic ports on the combustor walls. Acoustic radiation is also emitted by the combustion process, specifically from unsteady heat release, which causes volume expansions in the combustor. Both chemiluminescence (optical) and acoustic pressure measurements have been used for detection of LBO precursors by Muruganandam *et. al*.

4.1.1 Lean Blowout Precursors

Experiments were conducted at various equivalence ratios near the LBO limit. Chemiluminescence signals from the combustor showed intermittent events occurring very close to LBO. Figure 4-1 shows examples of optical sensor outputs at a stable equivalence ratio and one near LBO. Overall, the mean OH chemiluminescence signal decreases as the fuel flow rate is reduced. More importantly, as the LBO limit is approached, a number of sudden reductions in the OH emission are observed, with signal levels going well below the mean value. This is more clearly seen in the expanded optical emission time series data. Often, these events are characterized by an almost complete loss of chemiluminescence quickly followed by strong emission from the imaged region. Muruganandam *et al.* determined that these brief 'dips' in the signal correspond to a

localized extinction pocket in the flame followed by a strong reignition of the same region. These distinctive extinction and reignition events span a period of several milliseconds, and they occur, without any obvious periodicity, prior to LBO. As the LBO limit is approached, more of these events occur in a given time period and thus the time between two such events decreases closer to LBO. The data presented later will show that the above mentioned near-LBO "events" occur in a number of combustor configurations, and operating conditions, e.g., combustor diameter, length of the combustor, equivalence ratio, and flow rate. These temporary extinction-reignition events can thus be considered as precursors to the imminent total flame loss in the combustor. A closer investigation of these events using high speed visualization shows that localized extinction pockets appear in the flame, then the same region reignites with a higher level of luminescence. This intense combustion appears to initiate a regular (more stable) combustion process, until the next event occurs. These unique extinction and reignition events span a period of several milliseconds, and occur randomly in time (with no fixed frequency) prior to LBO. As the LBO limit is approached, more of these events occur in a given time period and thus the time between two such events decreases closer to LBO.

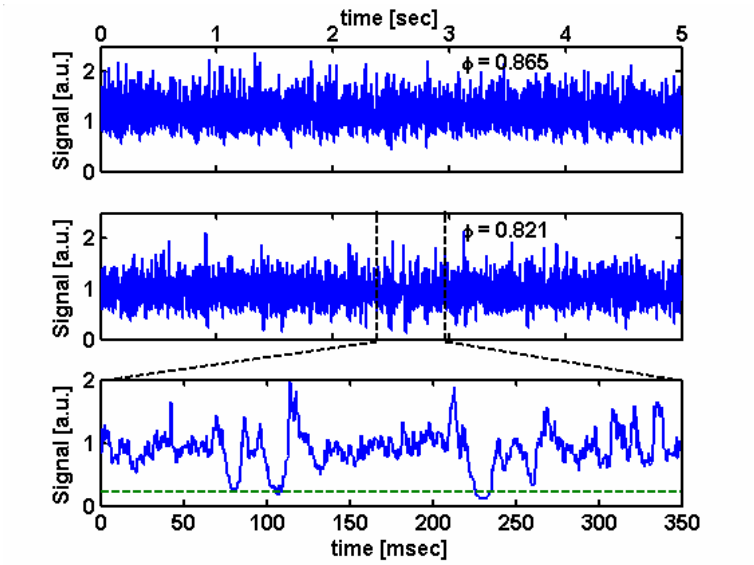

Figure 4-1. Time series data of OH chemiluminescence signal for ϕ = 0.865 and 0.821. (ϕ_{LBO} = 0.802) The expanded time series for the last case is also shown. Image adopted from Muruganandam.[15]

4.1.2 Detection Method

Muruganandam *et al.*[66] proposed a threshold based detection technique to identify and isolate localized extinction events. A detectable 'event' was declared whenever the OH signal dropped below a (somewhat arbitrarily chosen) value equal to about 25% - 35% of the mean signal value. This choice was based on the premise that the precursor signature is initiated by a local extinction event that temporarily lowers the chemiluminescence. Thus the low threshold approach provides the earliest detection of the event. The specific choice of threshold value for detection will vary depending on the combustor, the optical collection location, and the desired sensitivity and noise rejection of the technique. An example of noise effects is seen in Figure 4-2. During an extinction event, noise can cause the signal briefly rise above the event threshold and then fall below again.

To reduce the number of false alarms due to noise in the signal, double thresholding was used (see Figure 4-2). The event starts when the signal drops below a lower threshold, and ends only when the signal goes above the higher threshold. The gap between the two thresholds can be varied based on the noise present in the signal. Examples of conditions under which events are defined are also presented in Figure 4-2. Figure 4-3 shows the variation of average number of identified precursor events per second (averaged over 33 seconds) with equivalence ratio. Since this parameter increases as the LBO limit is approached, it can be used to sense the proximity to LBO.

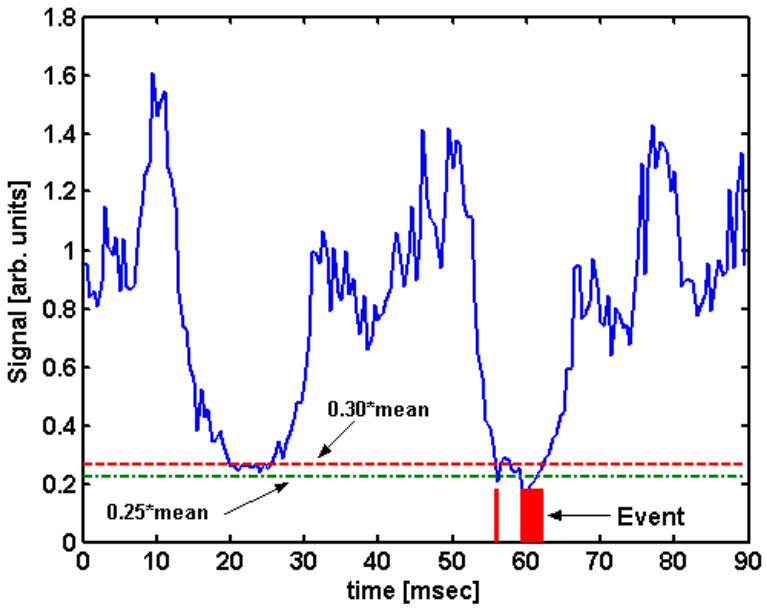

Figure 4-2. Noise rejection approach based on double thresholding used to detect the LBO precursor events. An event starts when the lower threshold is crossed and ends only when the signal returns above the upper threshold. Image adopted from Muruganandam.[15]

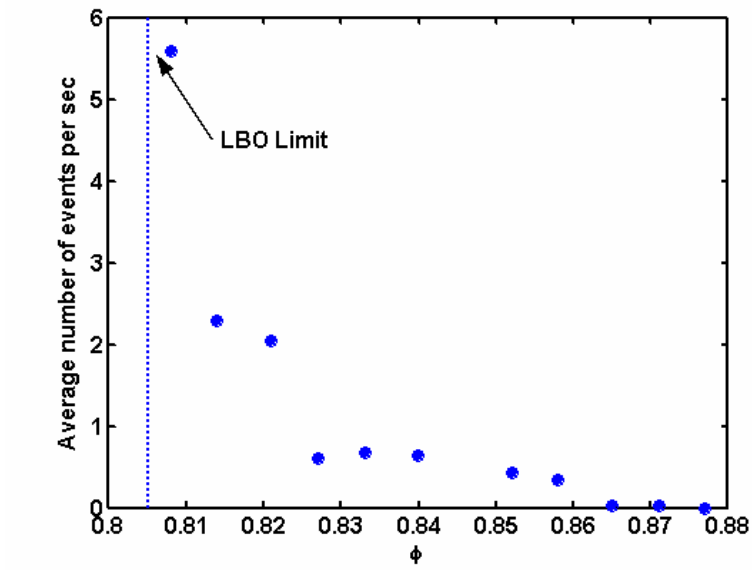

Figure 4-3. Variation of average number of events per second as a function of equivalence ratio. The dotted line indicates the LBO limit for these conditions. Image adopted from Muruganandam.[15]

4.2 Acoustic Sensing

Although optical chemiluminescence techniques can detect localized extinctions directly and with minimal noise, acoustic methods offer several advantages. Many land based gas turbines are already instrumented with dynamic pressure transducers, which can be installed and shielded in a harsh engine environment. Furthermore, unlike optical methods, acoustic sensors are not subject to field of view limitations, i.e. they can sense attributes of the entire combustion region.

4.2.1 Acoustic Signal

Analysis of acoustic emissions provides means for detecting transient flame holding events because they are proportional to the temporal rate of change of heat release. Since combustion noise is generated by the unsteady expansion of reacting gases, the acoustic emissions of turbulent flames are dominated by unsteady heat release[67] processes (as opposed to flow noise) that excite acoustic waves over a broad range of frequencies, typically between ~10 Hz – 25 kHz.[68] Thus, acoustic measurements can be

used to detect either global changes in heat release rate or fluctuations in heat release at certain time scales by measuring their acoustic emissions in the corresponding frequency bands.

Flame chemiluminescence studies have determined that as a lean flame approaches its LBO limit, the frequency of localized extinction – reignition "events" increases and that such events typically last from 10-15 milliseconds. An optical sensor sensing such an event will detect an abrupt drop in OH chemiluminescence during the extinction phase followed by a sharp increase during reignition (Figure 4-4, top plot). On the other hand, the acoustic signal's amplitude slightly increases during extinction, but with reduced amplitude fluctuation and the reignition phase is distinguished by a sudden "appearance" of a large amplitude oscillation as the flame deficient region is reignited with a noticeable 'pop' (Figure 4-4, middle plot). As the flame becomes leaner, the extinction regions may grow larger, and event durations may become longer.

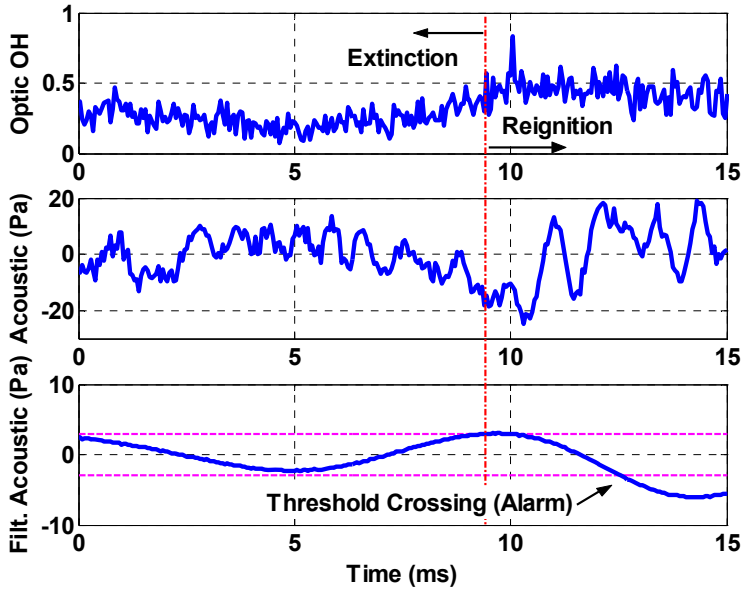

Figure 4-4. Anatomy of an extinction event, as captured by OH chemiluminescence (top), acoustic (middle), and bandpass filtered acoustic, 10.6 Hz to 95.5 Hz (bottom).

4.2.2 Filtering Scheme

Earlier studies[15,16] have determined that localized extinction events boost the low frequency (10 Hz – 200 Hz) content of both the OH Chemiluminescence (i.e. optical) and acoustic signals, as was apparent in Figure 1-4. Since the increase in the localized extinction-reignition events were presumed to cause the low frequency shift in the OH Chemiluminescence signal, the same phenomenon probably drives the low frequency shift in the acoustics as well.

Consequently, a study was conducted to examine the spectral characteristics of the acoustic signal in selected frequency bands. Bandpass filters were designed to attenuate all frequencies outside the range of interest. The filters were Butterworth 8^{th} order (4^{th} order high pass and 4^{th} order low pass) with center frequencies (ω_c) of 15.9 Hz (100 rad/s), 31.8 Hz (200 rad/s) and 63.7 Hz (300 rad/s). The bandpass filter ratio (α) that governed the width of the filters, was varied. In general, the low cutoff frequency was w_c/α while the high cutoff was $w_c*\alpha$. Hence, for a filter ratio (α) of 3, and center frequencies of 15.9, 31.8, and 63.7 Hz, the respective bandpass filters spanned 5.30-47.7 Hz, 10.6-95.5 Hz and 21.2–191 Hz. The magnitude plot of these filters is shown in Figure 4-5.

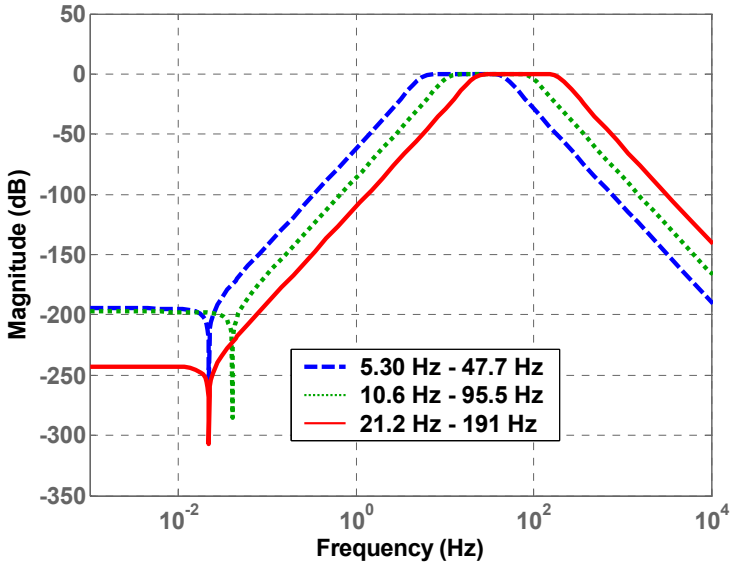

Figure 4-5. Magnitude plot of three bandpass filters with center frequencies at 15.9 Hz (100rad/s), 31.8 Hz (200 rad/s), and 63.7 Hz (300 rad/s), and a filter ratio of 3.

An effective blowout proximity signal should exhibit both sensitivity and linearity. Sensitivity requires a proximity gauge to change noticeably from rich to lean, while linearity implies that the intermediary points should approximate a line. The effect of filtering with different bandpass filters is evident in Figure 4-6. In the two plots, the normalized standard deviation is plotted for a set of filtered acoustic signals over a range of equivalence ratios. The signal standard deviation has been normalized by the value at the richest point ($\phi = 0.695$ for the 127 mm combustor and $\phi = 0.710$ for the 243 mm combustor). Clearly, filtering the acoustic signal improves the overall sensitivity for both combustor lengths. Whereas the unfiltered acoustic signal's standard deviation only increases by about 3% from $\phi = 0.695$ and $\phi = 0.640$, filtering that same acoustic signal with a bandpass between 23.9 and 95.5 Hz produces a signal whose standard deviation increases 37% over the same range. Although the OH chemiluminescence signal's standard deviation increases an impressive 45% at the leanest point, its gain at other

equivalence ratios is similar to the filtered acoustic signals. It is clear from the figure that bandpass filter ranges of 23.9-95.5 Hz, 15.9-143 Hz, 10.6-95.5 Hz, and 7.96-127 Hz all produce signals with decent sensitivity to blowout margin, for both the 127 and 243 mm combustor lengths.

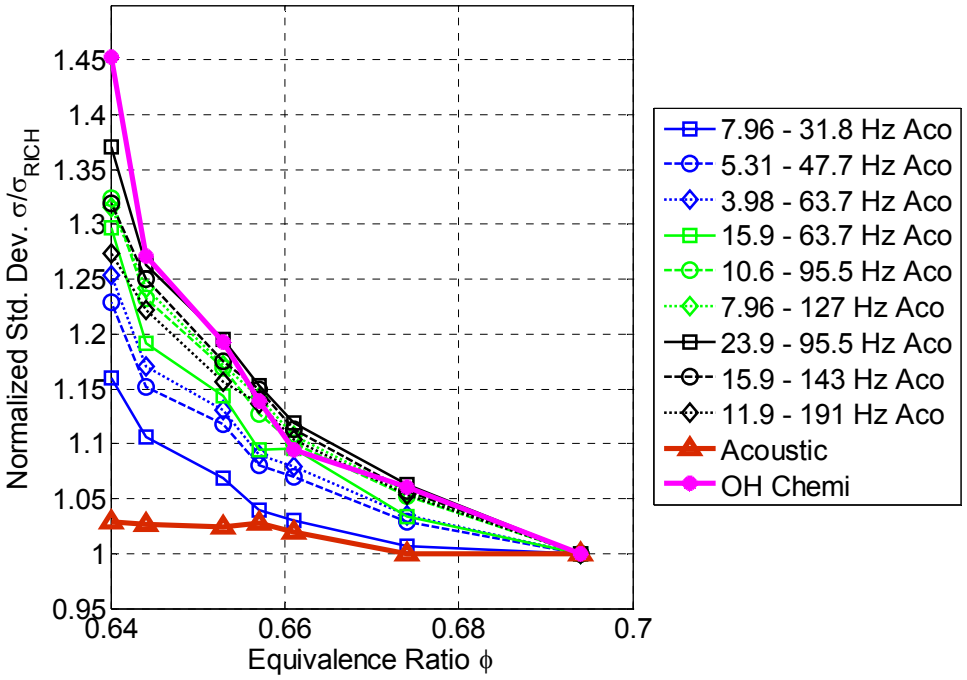

(a) 127 mm Combustor

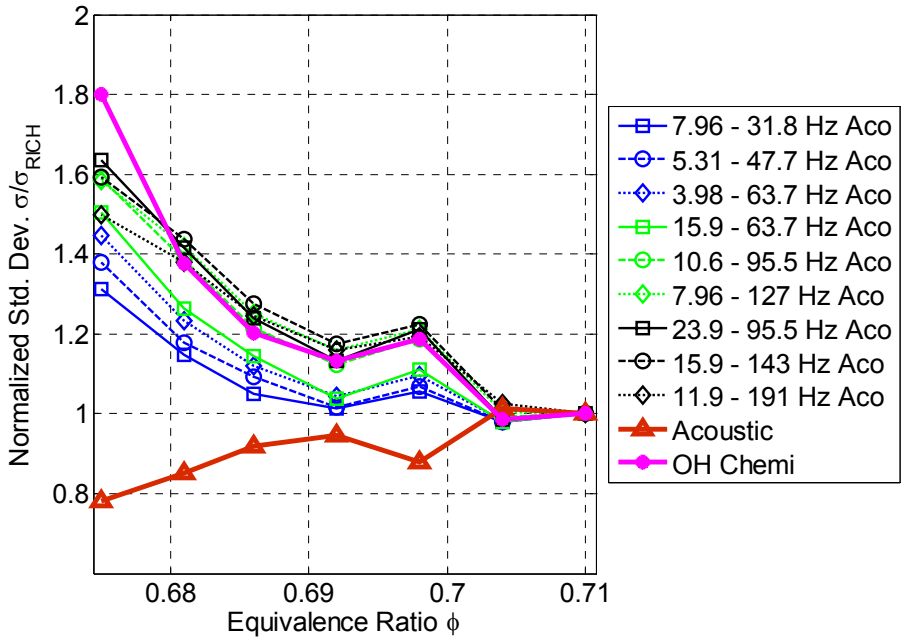

(b) 243 mm Combustor

Figure 4-6. Normalized standard deviation across a range of equivalence ratios for a set of raw and filtered signals collected from 127 mm (a) and 243 mm (b) length combustors. The signal standard deviation at a particular equivalence ratio was normalized by the standard deviation for the richest case (ϕ=.695 in the 127 mm combustor and ϕ=.710 in the 243 mm combustor).

An alternate method to determine signal gain is to measure the bounded area between the signal probability density function (PDF) curves from the richest and leanest recorded cases. A graphical depiction of the PDF area difference (ΔA) is shown in Figure 4-7. In the presented data, the richest case was taken at $\phi = 0.723$ and the leanest at $\phi = 0.694$. Clearly, the signal standard deviation is larger in the leaner case since the signal fluctuates more. The parameter ΔA is computed as the enclosed area bounded by the leanest case PDF above and the richest case PDF below, at the extreme ends of the distributions. A high value of ΔA indicates that thresholding techniques (outlined earlier) will be effective in differentiating between the richer and leaner cases.

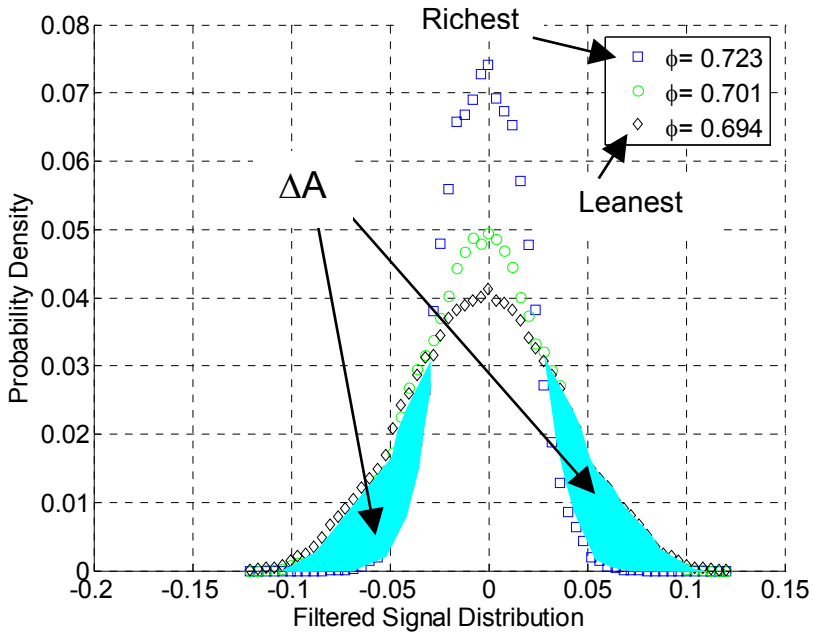

Figure 4-7. Probability density of the acoustic signal for three equivalence ratios, and the method used to determine the area change from richest to leanest.

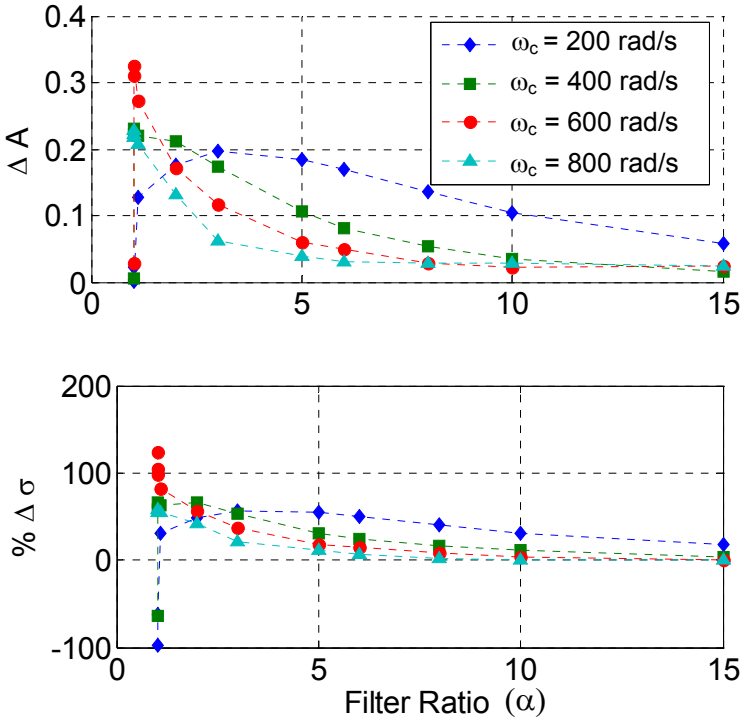

Figure 4-8. The effect of bandpass filtering the acoustic signal at specified center frequencies (ω_c) and filter ratios. The top plot shows the area difference between the richest and leanest case probability distribution functions. The bottom plot shows the percent change in standard deviation of the signal from the richest to leanest cases.

The ΔA values and the percent change in standard deviation from the richer to the leaner case are both shown in Figure 4-8. Each curve corresponds to a unique center frequency (ω_c) while the abscissa maps the filter ratio. Note that at 600 rad/s the signal gain is large only when the filter ratio is very close to one. Apparently, there is some sort of acoustic mode near that frequency that becomes excited at lean conditions. For detection purposes, it is prudent to rely on broad based, robust signals that are not overly dependent on geometry (as are acoustic modes), or filter parameters. In contrast, there is a region about $\alpha = 3$ for $\omega_c = 200$ rad/s curves where the curve has a zero slope for both ΔA and $\%\Delta\sigma$. Clearly, varying the filter ratio by small amounts produces almost no change in the overall gain. This suggests that at those parameters, the filtered signal is highly robust to variations in the filter.

The plots in Figure 4-9 show the normalized standard deviation of the filtered acoustic signals for a range of filter parameters for data taken from both the 127 mm and 243 mm length combustors. In these plots, the center frequencies of 15.9 Hz (100rad/s), 31.8 Hz (200 rad/s), and 63.7 Hz (300 rad/s) were used with a range of filter ratios. It was presumed that this frequency range should produce the most gain from rich to lean as indicated by the previously discussed analysis. Each curve corresponds to a different center frequency and the filter ratio is mapped on the ordinate axis. It is clear that filtering the acoustic signal significantly improves its sensitivity to equivalence ratio. Furthermore, the curves appear to change little with geometry in terms of how much amplification each filter provides relative to the OH chemiluminescence signal.

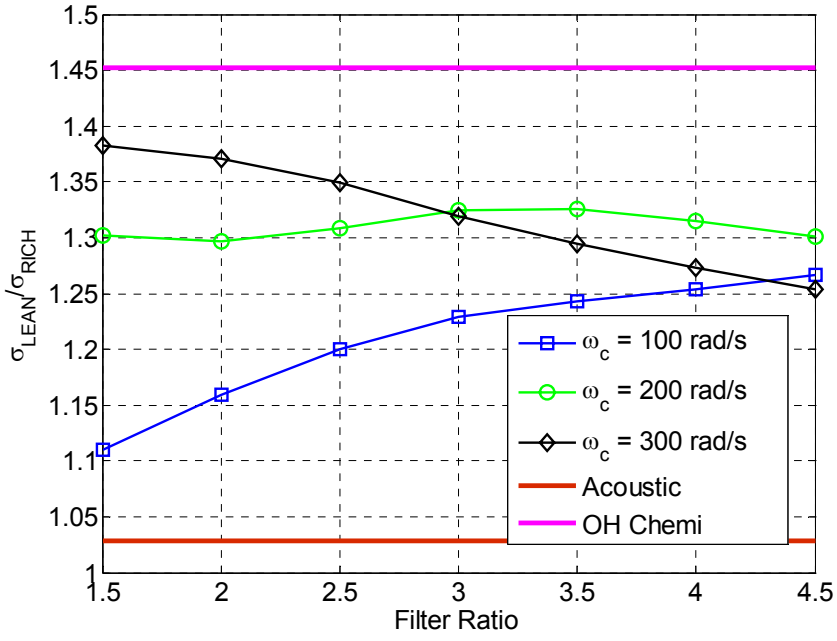

(a) 127 mm

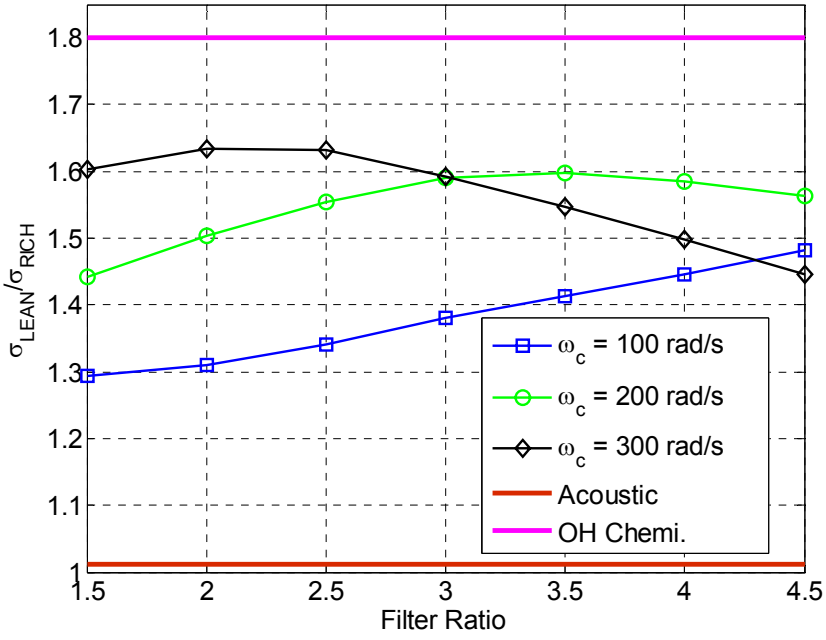

(b) 243 mm

Figure 4-9. The ratio of standard deviation from the leanest case (σ_{LEAN}) to the standard deviation from the richest (i.e. least lean) recorded case (σ_{RICH}) for the acoustic signal bandpass filtered with a range of center frequencies (ω_c) and filter ratios (α). Data shown is from 127 mm (a) and 243 mm (b) length combustors. The center frequencies of 100, 200, and 300 rad/s correspond to 15.9, 31.8, and 63.7 Hz, respectively.

4.2.3 Threshold Analysis

It is evident from the analysis presented so far that an acoustic signal bandpass filtered at the appropriate range will exhibit a significant variation from richer to leaner conditions. This variation can be captured using the same threshold techniques that were outlined previously as applied to the optical OH chemiluminescence signal. The dependence of the average number of threshold crossings (γ), normalized by the corresponding value of crossings at LBO (γ_{LBO}), upon the equivalence ratio is shown in Figure 4-10. While the low frequency (5.305 - 47.75 Hz) filter exhibited the greatest overall (relative) increase in alarm ratio, the rate of increase did not become significant until the equivalence ratio was below 0.72. The middle frequency filter (10.6 – 95.5 Hz) was comparatively more linear and also exhibited a large increase in alarm ratio over the equivalence ratio range. The bottom plot of Figure 4-4 shows how an acoustic signal passed through this filter (10.6-95.5 Hz) behaves during an event cycle. The extinction and reignition phases combined last approximately 15 ms, corresponding to a 66.67 Hz event 'cycle'. Since this frequency lies within the range allowed by the employed bandpass filter, a threshold crossing occurs in the filtered signal.

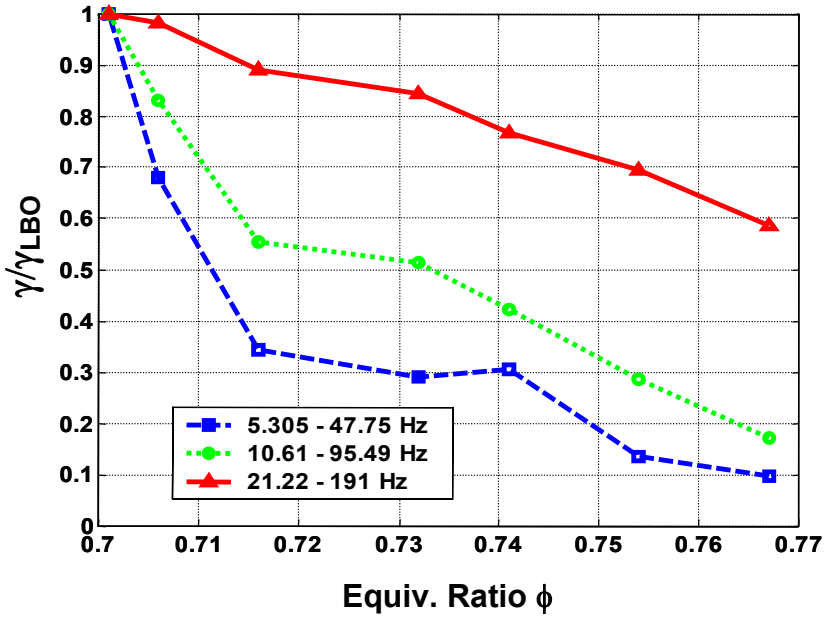

Figure 4-10. Number of threshold crossings by the filtered acoustic signal over a set of equivalence ratios, normalized by the number of threshold crossings at blowout.

4.2.4 Cross Covariance with OH Chemiluminescence

The acoustic signal, once filtered, can detect blowout proximity. Presumably, the spectral range that was isolated by the filter is detecting the same localized extinction-reignition phenomenon that was evident in the optical OH chemiluminescence signal. Yet, the OH signal is only a local measurement with a limited field of view while the acoustic signal detects global attributes of the pressure field. To determine whether the acoustic signal is indeed detecting the same localized extinctions that were evident in the OH chemiluminescence, the cross covariance between the filtered acoustic and optical signals was computed. The cross covariance presents a method for assessing the similarity between two signals and is the mean removed cross correlation. A high cross covariance (near 1) signifies that the two signals are similar.

The cross covariance between the raw (unfiltered) acoustic and optical OH chemiluminescence for a range of equivalence ratios is presented in Figure 4-11. Clearly, the maximum cross covariance value is less than 0.3. The peak occurs at a small

lag time since the acoustic pressure waves travel slower than electromagnetic waves. The cross covariance was computed over a time widow of 30 seconds.

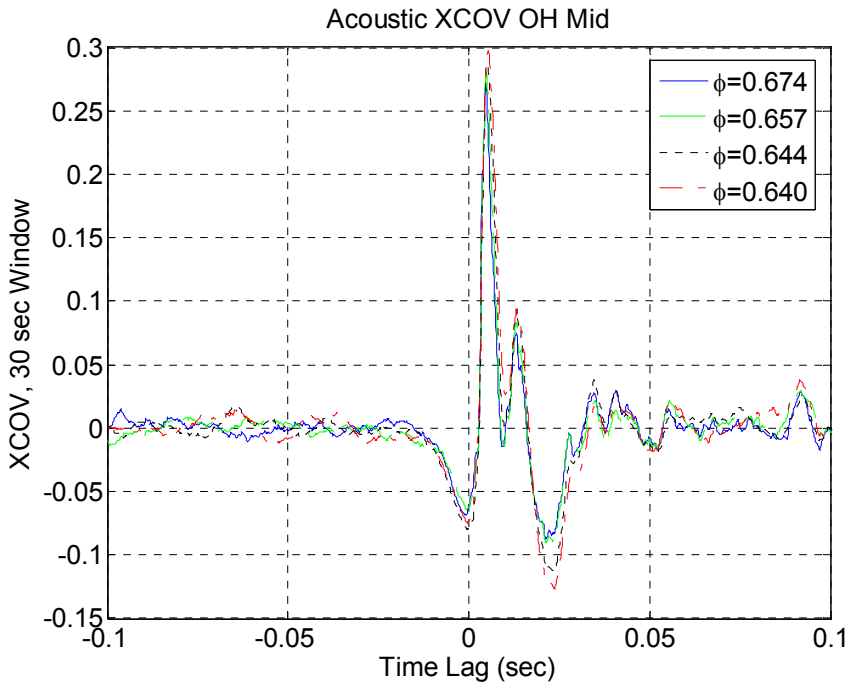

Figure 4-11. Cross covariance between the acoustic and OH Chemiluminescence signals, taken over a 30 second time window at different equivalence ratios.

Filtering the acoustic signal produces a noticeable increase in the cross covariance with the optical OH chemiluminescence. A plot of the peak cross covariance values, between the filtered acoustic and optical signals, for each equivalence ratio is shown in Figure 4-12. Clearly, filters at frequencies of 10.6-95.5 Hz, 7.96-127 Hz, and 11.9-191 Hz produce signals with a consistently high level of correlation with the optical signal throughout the range of equivalence ratios presented, for both the 127 mm and 243 mm combustor lengths. This suggests that the same localized extinctions that cause 'dips' in the optical signal causes a noticeable perturbation in the filtered acoustic signal as well, and that these events can be detected at the same frequency range regardless of combustor length. Figure 4-13 shows the cross covariance between an acoustic signal filtered with a bandpass at 10.6-95.5 Hz, and the optical OH chemiluminescence, for a

range of equivalence ratios. The plot shows data from a 127 mm length combustor. In comparison with the optical signal's cross covariance with the raw acoustic signal from Figure 4-11, it is clear that the filtered signal produces a higher magnitude peak that does not change significantly with equivalence ratio.

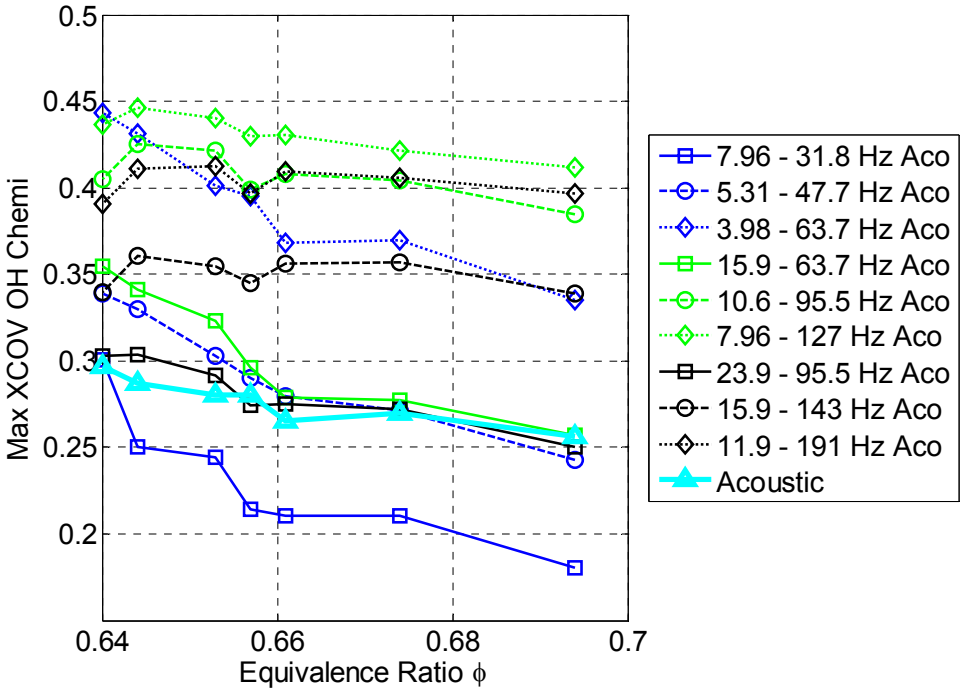

(a) 127 mm

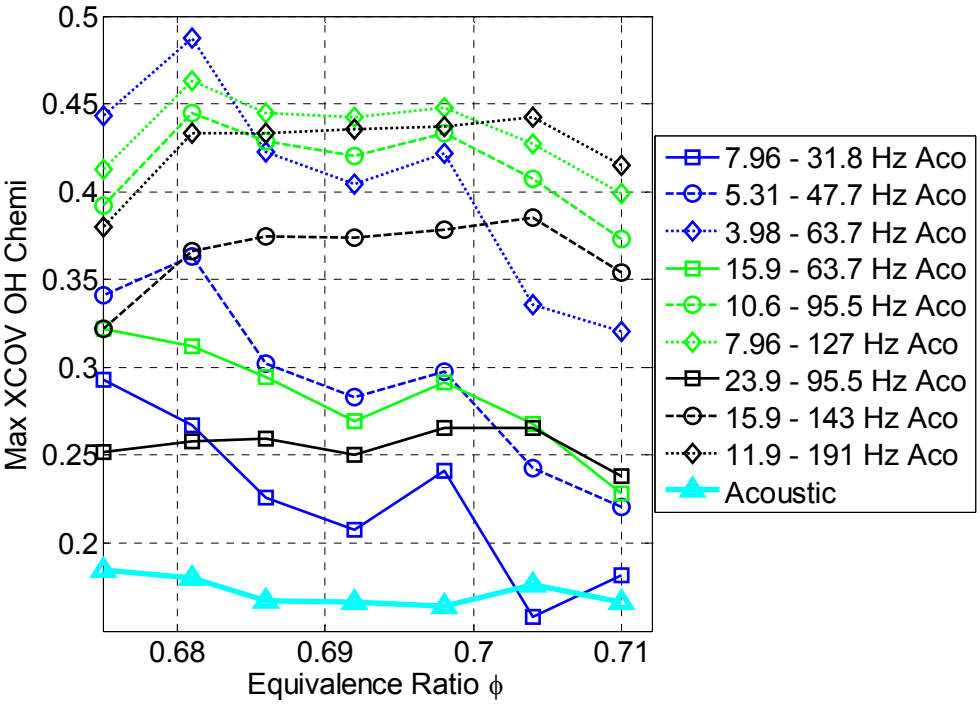

(b) 243 mm

Figure 4-12. Maximum values of cross covariance between filtered acoustic signals and the optical OH chemiluminescence across a range of equivalence ratios. Data shown was obtained from 127 mm (a) and 243 mm (b) length combustors. The unfiltered acoustic signal is designated 'Acoustic'.

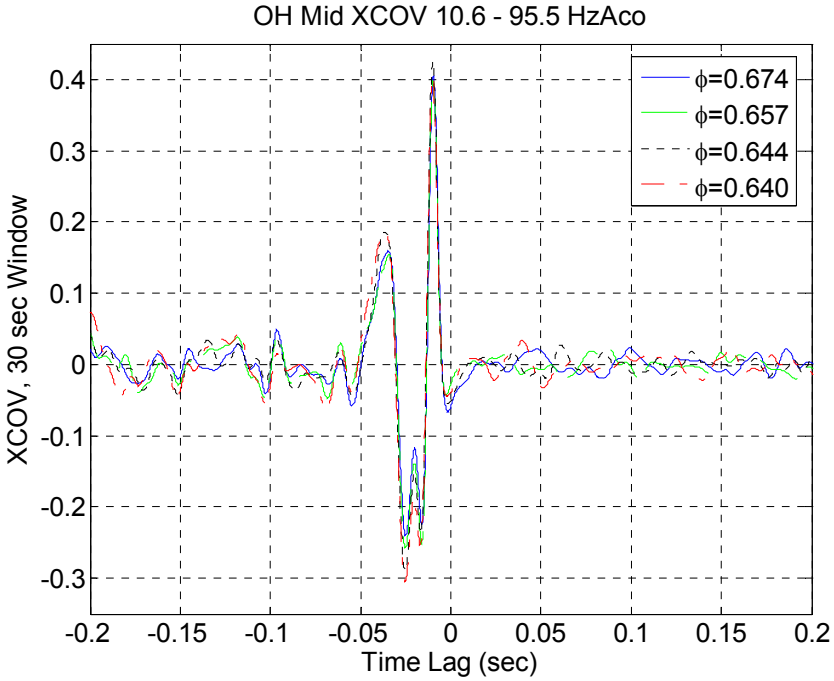

Figure 4-13. Cross covariance between the optical OH chemiluminescence and filtered acoustic signal, filtered with a 10.6-95.5 Hz bandpass filter.

CHAPTER 5. FLAME DYNAMICS

This chapter describes the observed flame structure and flame mode shift dynamics at lean conditions. A simplistic, empirical model is derived from the observed dynamic behavior of the flame, as it shifts from base-stabilized to tornado. While theoretical studies cannot capture the complexity of the flame, the empirical model can be used to predict flame behavior, and improve margin estimation.

5.1 General Observations

The combustor geometry allowed for the stabilization of various flame configurations as the operating conditions varied. Several flame transitions were especially noted as air flow into the combustor was gradually increased, affecting velocity and equivalence ratio throughout the combustion region.

The different observed flame configurations observed in the combustor are shown in Figure 3-3. At sufficiently high equivalence ratios, two flames were visible; a primary flame with a 'v-shaped' base centered near the swirlers and a secondary torus-shaped flame in the dump region around the primary flame's base. At conditions closer to blowout, only the primary flame remained. When the flame transitioned between the two-flame and single flame modes, the secondary flame pulsed, vanishing and reappearing at random intervals. When the secondary flame was present, the primary flame was closer to the inlet, most likely due to the additional heat and radicals generated by the secondary flame.

Several studies have examined the phenomenon of flame mode transitions at lean conditions[17,69,70]. Muruganandam and Seitzman[71] noted that as the flame becomes leaner,

it increasingly moves away from the inlet lip. The detachment points vary along the circumference of the lip, and at very lean conditions, the flame detaches completely. The flame then assumes a narrow 'tornado'-like shape until a reacting packet recirculates back to the lip, reattaching the flame and restoring it to its original form. After a few shape (or mode) shifting episodes, the combustor cools and the flame becomes less likely to reattach. If reattachment does not occur, the flame extinguishes within a few milliseconds. The 'tornado' mode is an unstable state in a 127 mm combustor, but it is stable in a longer combustor. Figure 5-1 depicts these stable and tornado flame modes in time averaged photographs, as reported by Muruganandam and Seitzman. Since the tornado mode was not stable in the shorter combustor (a), the image was taken in a longer combustor tube (b), where the geometry allowed the tornado flame to stabilize. In both images, the orange lines define the boundaries of the combustor. These flame shapes (or modes) were also observed by Bradley et al. in a similar combustor. High speed imagery in the shorter combustor verified that the flame briefly transitions to the tornado mode at conditions near lean blowout.

Muruganandam and Seitzman, as well as Bradley et al. noted that a swirl and dump stabilized flame can also briefly assume a narrow 'tornado' shape at conditions near blowout, as seen in Figure 5-1(b). This 'tornado' mode of the flame was found to be unstable in a 127 mm combustor; the shape was only evident for several milliseconds at a time. For this reason, the time-averaged photograph for Figure 5-1 (b) was taken in a longer, 243 mm combustor, where the tornado mode was stable.

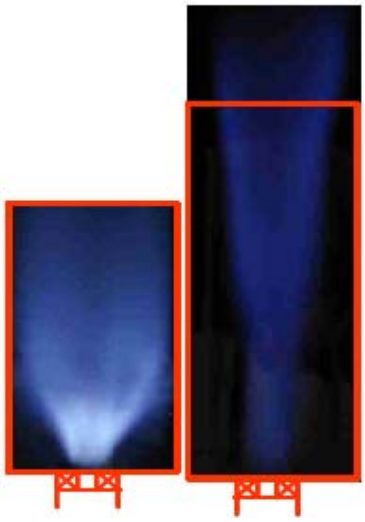

Figure 5-1. Photographs showing the flame shapes in the combustor: (a) a flame at a lean but stable equivalence ratio, (b) transient flame close to blowout in a longer combustor.

High speed imagery in the shorter, 127 mm combustor, as seen in Figure 5-2, verified that the flame briefly transitions to the tornado mode at conditions near, and immediately before, lean blowout. The inner recirculation zone 'bubble' has been marked in frame 1 of Figure 5-2, where the flame appears stabilized at the base of the combustor. Note the variation in the size of the momentum deficient bubble throughout the sequence of images. The fully developed tornado flame, as seen in frames 4-8 and 13-16, has a greatly diminished, and almost nonexistent breakdown 'bubble' zone. For the purposes of this study, the quasi-tornado forms that comprise the transient flame shapes (as seen in frames 2, 3 and 8-12) will also be considered 'tornado' mode. In general, 'tornado' will refer to a degenerate flame with diminishing bubble size that marks a significant deviation from the nominal, base-stabilized flame.

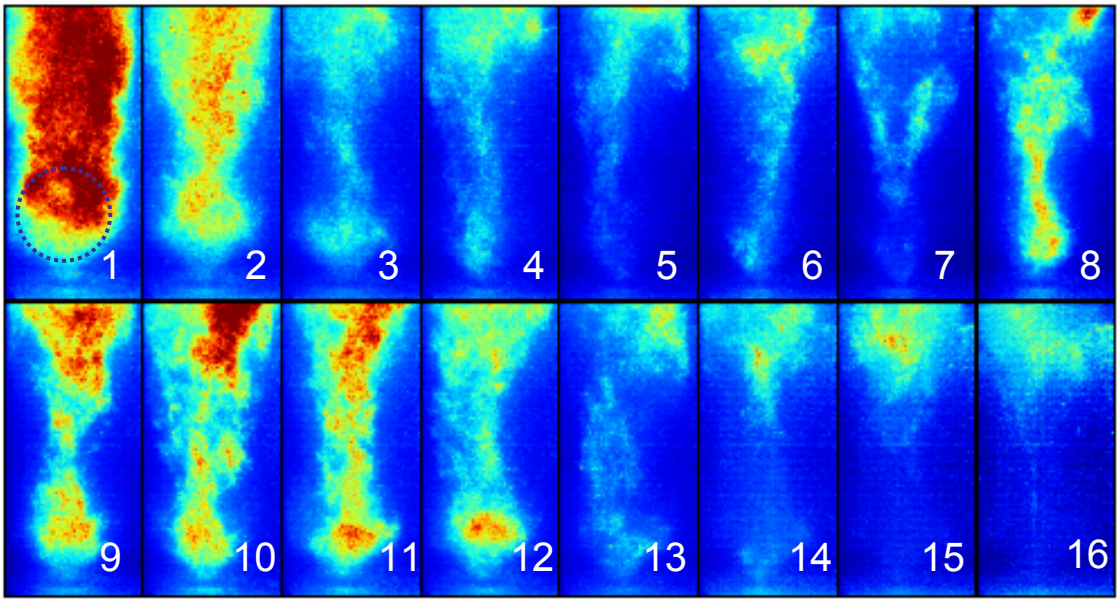

Figure 5-2. Sequence of OH chemiluminescence images showing a blowout event. Separation between each frame is 4 ms. The inner recirculation zone 'bubble' is marked in frame 1, and a fully developed 'tornado' is seen in frames 4-8 and 13-16. The remaining frames show quasi-tornado flame modes. Images adopted from Muruganandam.[17]

5.2 Dynamic Analysis

The aims for this portion of the study were to determine whether the underlying dynamics of flame shape transitions could be characterized, and if so, how such information could be integrated in blowout margin estimation. Flame shape variations are best detected optically, utilizing the optical apparatus discussed in Section 3.3.2 with thresholding methods outlined in Section 4.1.2

Two combustor lengths were used to study flame transitions: 127 mm and 243 mm. The 'tornado' flame mode can stabilize in the longer, 243 mm combustor, while such a mode is a symptom of blowout in the 127 mm combustor. The premise was that the transition to tornado is essentially a transition to blowout. A tornado flame not only indicates loss of the base-stabilized flame structure, it is in itself a very weak and ineffectual flame.

5.2.1 Sensor Placement

In order to identify flame shape variations and local extinctions, two photomultplier transducers were placed such that their field of view corresponded to regions of interest in the combustor, as seen in Figure 5-3. The two sensors were labeled 'mid' and 'high' according to their respective orientations; the light detected by the 'high' sensor was left unfiltered while the 'mid' sensor was filtered for OH chemiluminescence. This arrangement allowed detection of localized extinctions as well as tornado mode bursts.

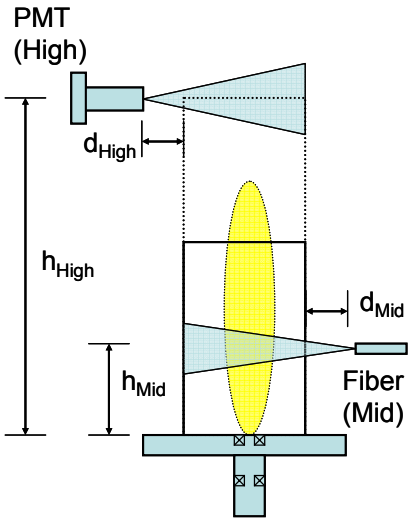

Figure 5-3. Diagram depicting the optical sensor locations.

The upper, or 'high', sensor position was chosen to assure that no flame was detected unless a mode transition 'burst' occurred, indicating a flame shape-altering event (e.g., transition to tornado mode). With both the 127 mm and 243 mm length combustors, the 'high' sensor was approximately 245 mm above the combustor inlet (h_{High}) and ~57 mm laterally from the tube wall (d_{High}). When the longer tube was in place, the high sensor was level with the tube lip. An aperture restricting cover with an opening of 2 mm was placed on this sensor to limit its field of view. The 'high' signal

showed a negative value spike when a burst occurred and zero otherwise, as seen in Figure 5-4. The negative value was due to the polarity setting.

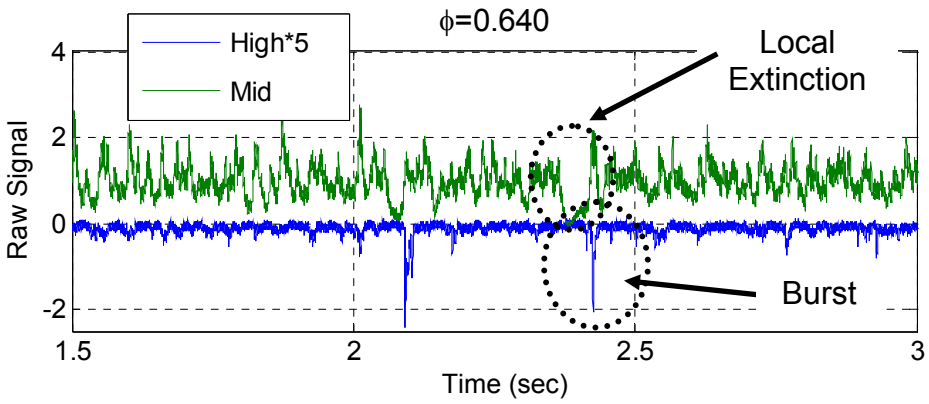

Figure 5-4. Time traces of the optical signals from each sensor. The 'mid' sensor exhibits the dips that correspond to localized extinction events. The 'high' sensor spikes whenever light is detected; these bursts correspond to flame shape transitions.

The other sensor was placed lower, near the inner recirculation zone (as shown in Figure 3-1). Earlier studies have shown that horizontally oriented sensors placed here will detect the maximum number of events[15,71]. The inner recirculation region is also the location of maximum strain rate, so more local extinctions would be expected here. The 'mid' sensor detected radiation from the combustor via a fused silica fiber optic cable. The collected light was then passed through a 308 nm interference filter (OH chemiluminescence) with 10 nm FWHM and onto a miniature photomultiplier (Hamamatsu H5784-04). For both combustor lengths, h_{Mid} and d_{Mid} were approximately 57 mm and 25 mm respectively. The fiber had an acceptance cone half angle of about 12º. The 'mid' sensor detected a flame at all times while the combustor was lit. However, localized extinctions presumably caused the OH-filtered signal to 'dip' below a percentage of its mean for the duration of the extinction, as was explained in Chapter 4, and depicted in the time trace in Figure 5-4. These localized extinction episodes had

been previously found to increase in both duration and occurrence frequency as the blowout limit was approached.

As was discussed in Section 4.1.2, localized extinctions can be detected in the OH chemiluminescence signal by noting when the signal drops below a certain percentage of its mean. Hence, the signal designated 'mid' is mean-normalized over a 30 second window. This allowed the threshold to be set at a static, mean-normalized value and facilitated comparison between different data sets.

5.2.2 Signal Distribution

The evolution of the sensor signals was examined as the fuel air ratio was reduced. An increase in precursors was expected to increase signal variance. The signals' cumulative distribution was considered for a range of equivalence ratios, and for both combustor lengths. The cumulative distribution function (CDF) at a certain signal level x is the definite integral of the probability distribution function (PDF) from negative infinity to x. As a result, the cumulative distribution is 0 at negative infinity and 1 at positive infinity.

Figure 5-5 shows the cumulative distributions from the 'high' sensor for both the short (127 mm) and long (243 mm) combustors. As more light bursts are detected from tornado bursts, more 'spikes' occur in the signal and the signal distribution curves shift accordingly to the left to reflect the presence of increased negative values. In both combustor lengths, the distributions appear to shift gradually. However, the leanest distribution in the 243 mm combustor, at ϕ=.675, shows a marked departure from the curves at the other equivalence ratios (Figure 5-5-b). At this condition, the flame starts to linger longer in the tornado mode, which is also stable in this combustor length. Apart

from this aberration, the short and long combustor curves appear to behave in a similar manner.

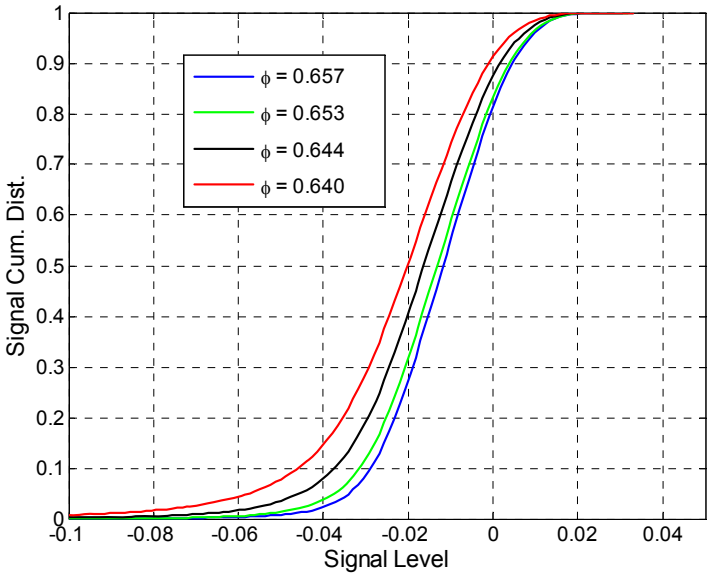

(a) 127 mm

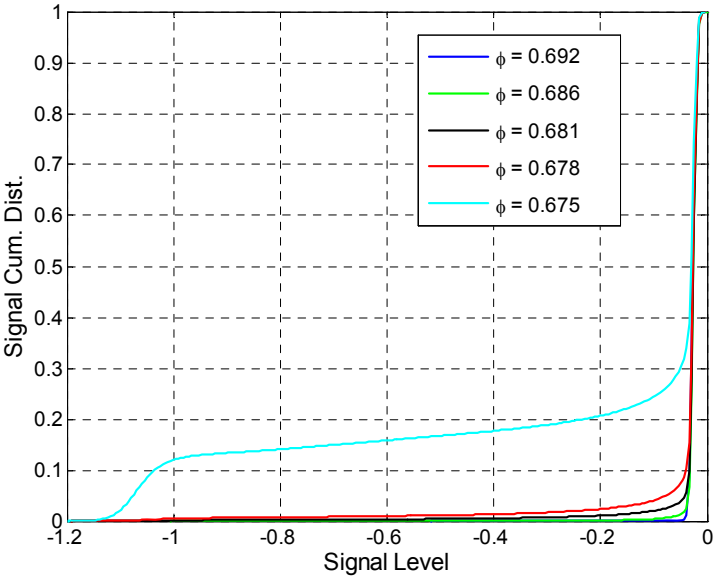

(b) 243 mm

Figure 5-5. Signal cumulative distributions taken across a range of equivalence ratios for both the standard 127mm (a) and long 243 mm (b) tube lengths, from the 'High' sensor location.

Figure 5-6 shows the cumulative distribution functions for the 'mid' sensor signal, measured in the standard (a) and longer length (b) combustors at different equivalence

ratios. .Once again, the trends appear similar for both geometries with the exception of the leanest equivalence ratio in the 243 mm combustor (see Figure 5-6 (b), $\phi = 0.675$).

It is clear that the transition to a stable tornado mode in a 243 mm combustor is similar to the transition to blowout in the 127 mm combustor. The traces from both 'high' and 'mid' sensors depict a gradually evolving system which begins to increasingly adopt a different mode for brief periods of time. In the case of the 243 mm combustor, the new mode is also stable. In the case of the 127 mm combustor, the state is not stable, and the flame cannot be sustained.

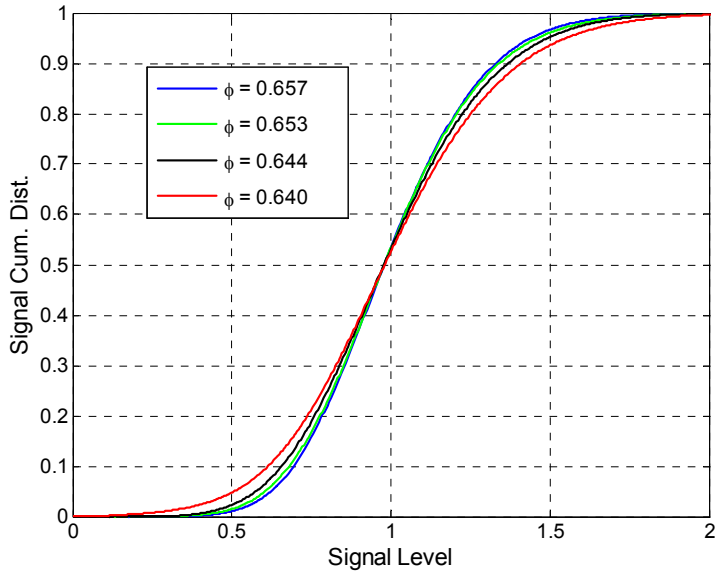

(a) 127 mm

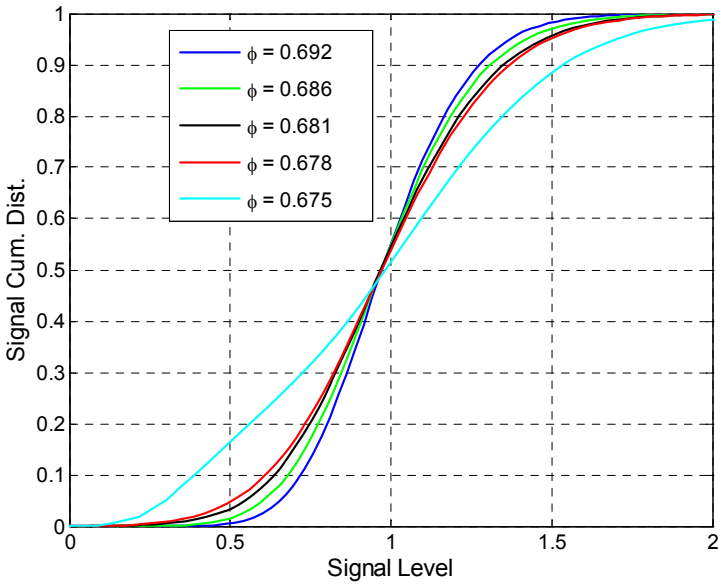

(b) 243 mm

Figure 5-6. Signal cumulative distributions taken across a range of equivalence ratios for both the standard (a) and long (b) tube configurations, from the 'Mid' sensor location. Note that the tornado mode appears as an extinction in this sensor's field of view.

5.2.3 Signal Cross Correlation

Cross correlating the 'mid' and 'high' sensor signals provides a method for determining when and to what degree large scale changes, such as tornado bursts, are present in the flow, and how activity in one region affects another. As seen in Figure 5-4, a localized extinction causes the 'mid' signal to dip to lower positive values and a tornado burst causes the 'high' signal to spike towards larger negative values.

Fundamentally, cross correlation provides a measure of how two signals evolve relative to each other over a range of positive and negative time delays. More appropriately, cross covariance (XCOV) provides a mean-removed cross correlation that captures how the signals increase and decrease with respect to each other. The cross covariance of two signals (x and y) is defined by Hayter[72] as:

$$XCOV_{x,y}(k) = \frac{\sum_{i=1}^{n}(x(k)-\bar{x})(y(k)-\bar{y})}{\sqrt{\sum_{i=1}^{n}(x(k)-\bar{x})^2}\sqrt{\sum_{i=1}^{n}(y(k)-\bar{y})^2}} \tag{5.1}$$

In Equation (5.1), overbars denote the mean, and summations are carried out over a prescribed time window. The index 'k' refers to the k^{th} time sample. The cross covariance is zero when the two signals are independent, and tend towards 1 or -1 depending upon whether the signals are correlated positively or negatively. Values near 1 or -1 indicate a highly linear fit.

Figure 5-7 shows the plot of the cross covariance between the 'high' and 'mid' sensor signals for both the 127 mm and 243 mm length combustor geometry. Note the slight negative correlation at zero lag for both combustor geometries. This is due to the fact that when the 'mid' signal detects a local extinction, the 'high' signal also detects

less light. The opposing polarity between the two sensors translates into a negative correlation.

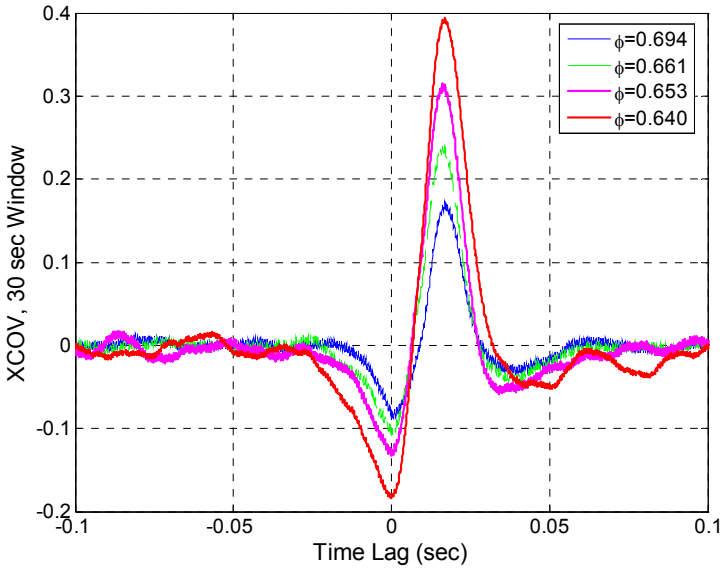

(a) 127 mm

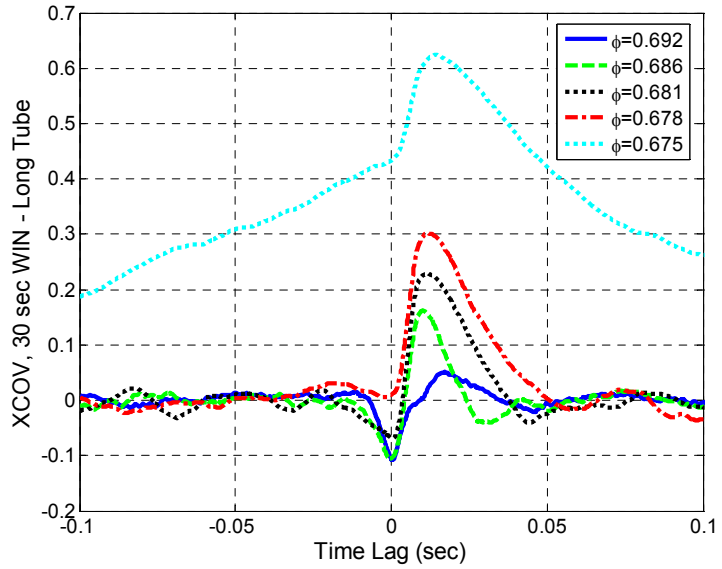

(b) 243 mm

Figure 5-7. Plots of the cross covariance between the 'High' and 'Mid' sensor signals from the standard (a) and long (b) tubes. The peaks increase in magnitude and shift towards larger lag times as the equivalence ratio decreases.

At the covariance peaks, which are much more pronounced compared to the valleys at zero lag, the high signal correlates positively with the mid signal. Once again, there is a similarity between both geometries except for the leanest case in the 243 mm combustor. In all cases, the peak increases in magnitude as the equivalence ratio decreases, and slightly shifts towards a larger time lag. In the long tube, the peak shifts from 10 ms (for ϕ=.686) to 12 ms (ϕ=.678), then to 15ms (for ϕ=.675). The peak in the short tube stays near 17 ms for all equivalence ratios.

The high degree of similarity across the curves and a near concurrent, prominent peak suggest that there is some deterministic process which is occurring with greater frequency or amplitude as the combustor approaches blowout. The process can be considered distinctive because of the definitive causality as suggested by the cross covariance peak.

The cross correlation peak at ~15 ms lag corresponds to a delay time between extinction in the lower sensor and light in the higher sensor. Since the combustor mean axial flow velocities are at the order of 10-15 m/s; the flow should therefore take about 13 - 19 ms to cover the 190 mm distance between the lower and upper sensors. This affirms that the cross correlation peak is primarily due to convection time scales and is not a result of other effects such as pressure waves. Interestingly, the convection time increases slightly as the flame becomes leaner, and as a result, weaker. The fact that the peak lag corresponds to the convection time suggests that a tornado burst occurs a convection period after a local extinction.

The time traces in Figure 5-8 confirm the conclusions derived from the ensemble cross correlation analysis. In the top plot of the figure, a tornado burst is detected by the

high sensor about 20 ms after the local extinction dip is detected by the mid sensor. The bottom of Figure 5-8 shows the cross covariance of the high and mid signals over a 10ms time window, for both zero and convection time lag. As seen in the bottom part of he figure, a clear peak occurs in the cross covariance at convection time lag during a tornado burst. This is because the spike corresponding to the burst in the 'high' signal is correlating with the extinction dip in the 'mid' signal. The polarity setting is such that both signals move lower with respect to their means, producing the positive correlation. It is plausible that the initial local extinction triggers the tornado event.

At about the time the localized extinction occurs, we see a negative correlation at zero lag (bottom of Figure 5-8). Since the localized extinction reduces the overall flame luminosity, both optical sensors detect less light. Therefore, when the 'mid' signal dips, the 'high' signal moves upwards (due to the reversed polarity). This causes the negative correlation at zero lag.

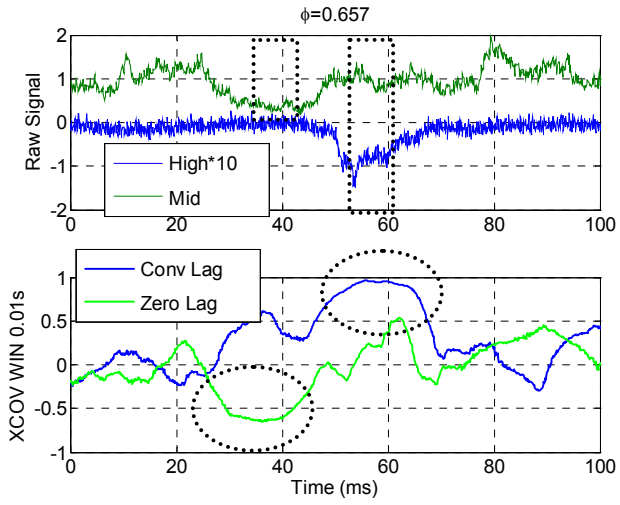

Figure 5-8. Effect of an extinction/ tornado event couple on the 'high' to 'mid' cross covariance. Data was taken from the 127 mm length combustor. The top plot shows the signals over time, with the vertical lines showing the convection delay. The cross covariance traces in the bottom plot were computed over a 10 msec window at lag times of 17 ms (the convection time) and zero.

According to Muruganandam, the flow expansion that accompanies chemical reaction is lower when the equivalence ratio, and hence the reaction rate, is reduced. As a result, the inner recirculation zone 'bubble' in a swirl and dump stabilized flame reduces in size. The flow surrounding the bubble will exert greater pressure on it since the swirl number is reduced, i.e., there is less flow deflection from the axial to the radial direction. The tornado mode then develops when the 'bubble' completely collapses.

Hence, the mid signal 'dips' that precede the tornado are probably and indication of the recirculation zone's collapse. The remaining reacting regions are then convected upwards and the tornado burst appears in the 'high' sensor signal after the convection period. When the 'high' sensor detects the burst, the 'mid' detects a flame again as the tornado mode becomes fully formed. Next, the unstable tornado begins to shrink and the signal from the High sensor shows a reduction in light. Then, according to Muruganandam, a reacting packet is circulated back to the base, where the flame reattaches. At about 80 ms in Figure 5-8 we see a sudden burst of light in the 'mid' sensor, presumably from the successful flame reattachment.

5.3 Event Analysis

When considering mode transition events in the high sensor or local extinctions in the mid sensor, it is useful to isolate such occurrences from the signal and analyze their characteristics. For this purpose, thresholds have been extensively used as a means for precursor detection. Muruganandam et. al. detected localized extinction events in the OH chemiluminescense signal using dual thresholds – a lower one to determine the initiation of the event and a higher one to determine the termination of the event. The dual threshold reduced the likelihood that one actual event (whether burst or extinction) will cause multiple threshold crossings.

By nature, precursors are discrete events. The statistics of the time between events and the duration of the events can provide useful information about the physics of

the precursors and improve margin detection techniques. Furthermore, understanding the behavior of precursors will help in determining sensing and processing requirements (e.g., signal resolution and sample rate), and aid in isolating events from the background signal.

In objective of the 'high' signal is to isolate the tornado type precursors while in the mid signal, the objective is to determine when localized extinctions are occurring. To study the metrics of these blowout precursors, a threshold approach is adopted for defining and isolating precursor events. Since the high and mid signals dip towards "negative infinity" during either a tornado burst or a localized extinction, a threshold 'crossing' is declared when the signal crosses from the threshold's positive side to its negative side.

The thresholds on the high signal are at a fixed voltage value, since the signal itself is mostly near zero except when a tornado burst occurs. In contrast, the mid signal is derived by normalizing the raw signal from the mid sensor by its 30-second mean. Therefore, the threshold level, as applied to the normalized signal, is a percentage of the mean of the non-normalized signal. Figure 5-9 shows an illustration of the dual threshold approach. The first threshold level (designated 'Th 1') corresponds to the upper threshold while the second (Th 2) is the lower, event-initiating threshold. An event 'beginning' is defined at the time the signal crosses the lower, more extreme threshold. The event terminates only when the signal returns above the upper threshold. Before this, the signal may cross the lower threshold multiple times but these crossings will not be counted as new events while an event is ongoing. The time between the beginning and ending of an event is its duration.

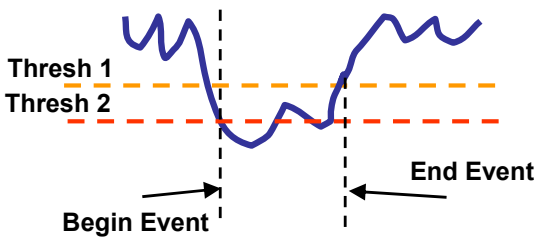

Figure 5-9. Illustration of the dual threshold method used to isolate precursor events. The signal must cross the more extreme threshold to signal the initiation of an event, and return above the less extreme threshold for the event to be terminated.

5.3.1 Event Spacing

Using the described threshold criteria, the statistics of event spacing (i.e. mean, median, and standard deviation) are shown in Figure 5-10. Note the similar trends across geometry. While the spacing between events in detected by both sensors decreases closer to blowout, as expected, the trends in the 'mid' signal events appear almost linear for both combustor lengths. In contrast, the 'high' event spacing increases almost exponentially in both combustor lengths. Also, note that the mean and standard deviation appear to be almost equal for all the data points presented.

The cumulative distributions of event spacing for certain cases are displayed in Figure 5-11. Note that the curves describing event spacing in both signals can be approximated as

$$F(x) = 1 - \exp(-x/\mu), \qquad (5.2)$$

which is the cumulative distribution function (CDF) of an exponential distribution with mean μ. The exponential distribution has the additional property that the mean is equal to the standard deviation, as was shown to be the case in Figure 5-10.

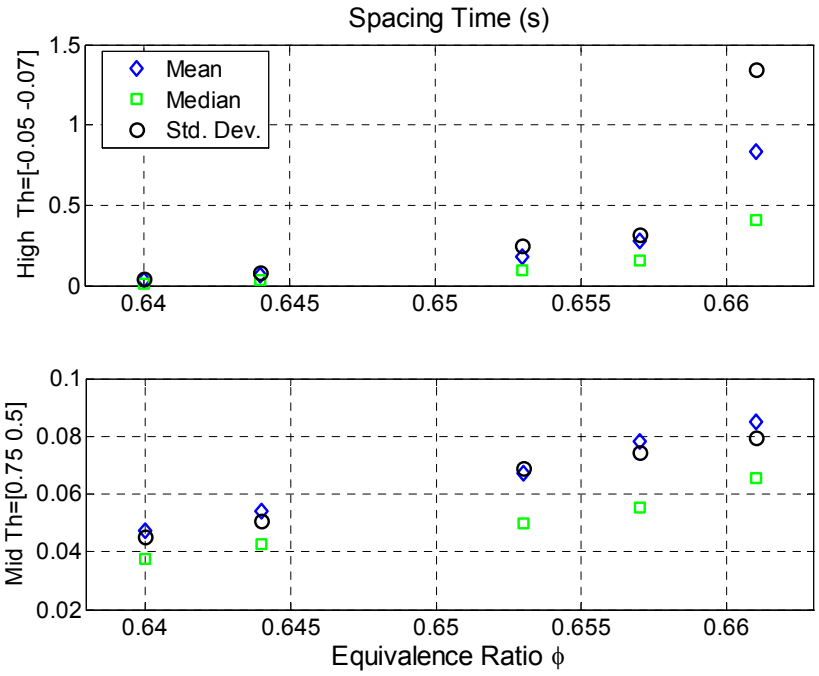

(a) 127 mm

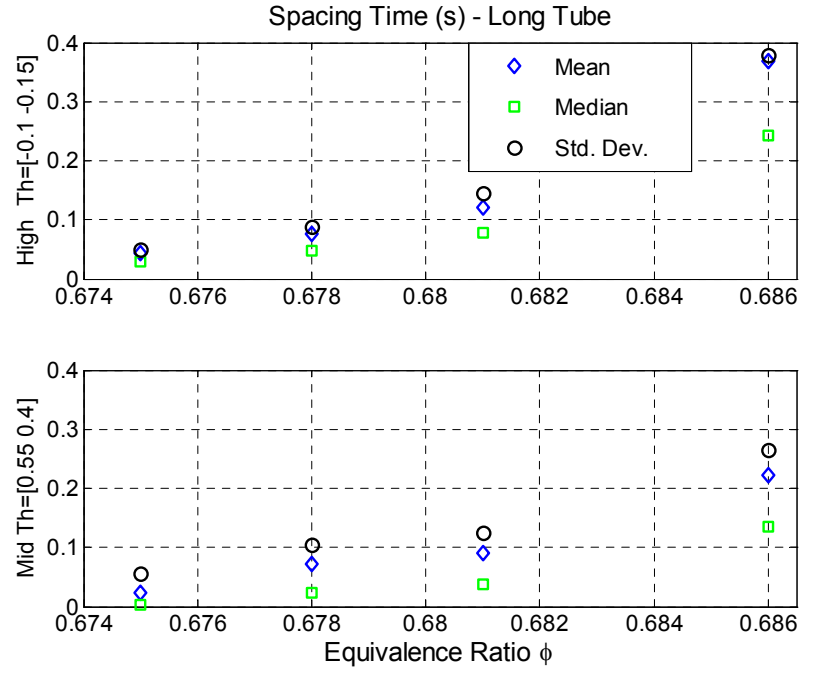

(b) 243 mm

Figure 5-10. Distribution statistics of 'event' spacing from (a) the 127 mm combustor and (b) the 243 mm combustor. Threshold values are displayed on the y-axis labels.

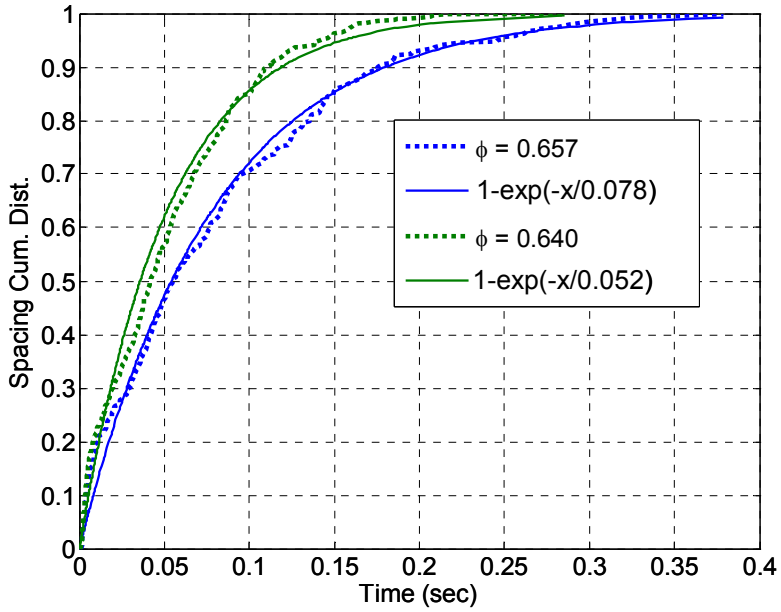

(a) Mid PMT

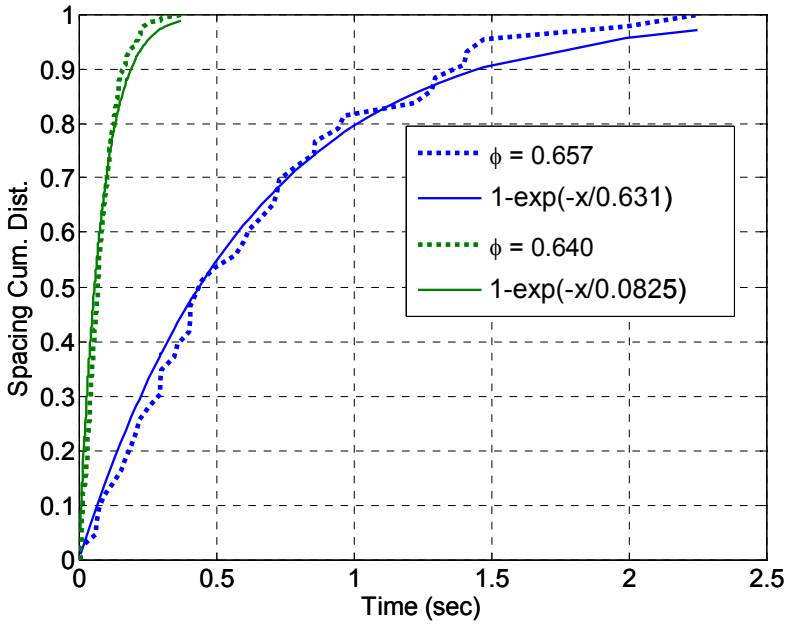

(b) High PMT

Figure 5-11. Cumulative distribution of 'event' spacing from (a) the mid signal and (b) the high signal. The data appear to follow an exponential distribution, indicating a Poisson process. Data shown was collected from the 127 mm combustor.

When the time intervals between discrete events are exponentially distributed, the process is 'Poisson'. In a Poisson process, the number of events within a specified time interval (T) has a Poisson distribution, where the probability of observing k events in interval T is given by:

$$P(N_T = k) = (T/\mu)^k \exp(-T/\mu)/k! \qquad (5.3)$$

Poisson processes are 'memoryless' whereby the time until the k+1 event is independent of time elapsed since the k^{th} event. A Poisson process is employed in modeling scenarios such as failures in an assembly line or the number of traffic accidents at a particular intersection. In these cases, there is no deterministic method to predict when the next event will occur. Similarly, a localized extinction or tornado burst may be considered a failure in a stable combustion process.

While a particular type of precursor does not influence the future occurrence of the same precursor type, it is evident from the previous section that one type will precede the other. Thus, even if each precursor is a memoryless Poisson process, a cause-effect relationship between precursors still appears evident.

5.3.2 Event Duration

The distribution statistics of event duration are presented in Figure 5-12 for both the 127 mm and 243 mm combustor lengths. Generally, the duration of events seem less affected by equivalence ratio than the spacing. One possible explanation for this is that events (whether localized extinctions or bursts) arise from turbulence driven flow processes which behave in a prescribed manner regardless of equivalence ratio. Hence, fluid dynamics are more significant than chemical kinetics in determining the duration of an event.

Also worth noting is that at leaner conditions, when events occur with increasing frequency, a long duration event may actually be two or more closely spaced events which were indistinguishable from the signal trace. This effect probably caused the notable increase in outliers at leaner equivalence ratios.

Figure 5-12 (b) once again shows that the leanest case in the 243 mm combustor is a significant departure from the other curves, indicating a more sustained mode shift. The median duration of the tornado burst (detected as a 'high' event) remains around 5 ms in the 127 mm combustor, and within about 2-3 ms for the 243 mm combustor for most cases. However, for the leanest case (ϕ=0.675) in the 243 mm combustor, the median tornado duration remains around 3 ms but the mean jumps to almost 10 ms and the standard deviation rises to 28 ms. As noted earlier, this is the case where tornado mode shifts become more sustained in the 243 mm combustor. The fact that this does not occur in the 127 mm combustor suggests that there is a critical tornado burst duration beyond which the flame will not readily transition back. A likely explanation is that the flame stabilization surfaces cool during a tornado burst. A sustained burst causes excessive cooling, which inhibits the flame from recovering to its base-stabilized mode.

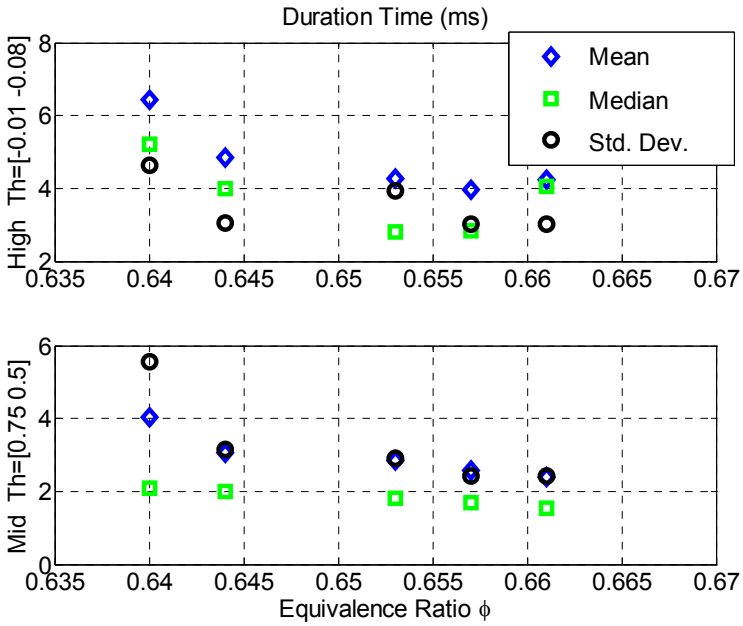

(a) 127 mm

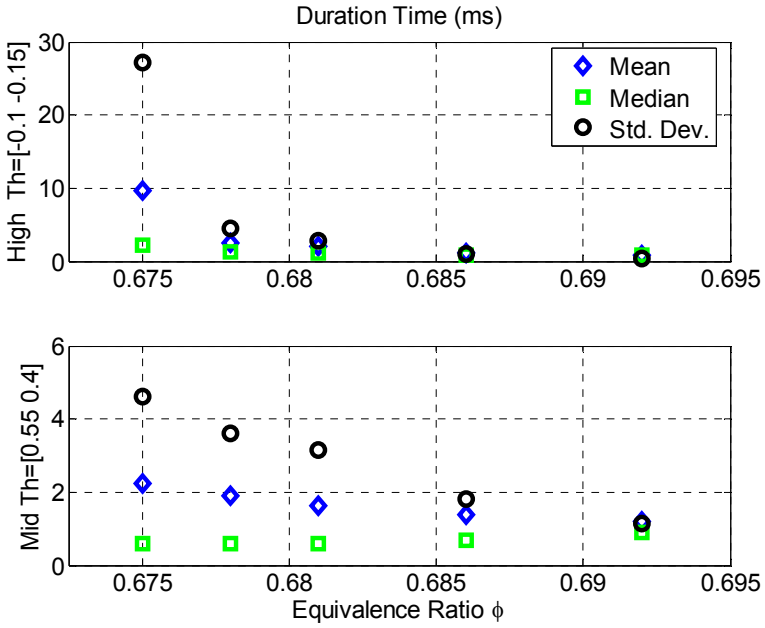

(b) 243 mm

Figure 5-12. Distribution statistics of 'event' duration from (a) the 127 mm combustor and (b) the 243 mm combustor. Threshold values are displayed on the y-axis labels.

5.4 Predicting Mode Shifts

While it is clear from the cross covariance analysis that a detected localized extinction 'dip' will precede the tornado 'burst' by about the convection time, not all such dips are followed by a tornado. It is useful, therefore, to develop a means to distinguish between the tornado preceding dips and more 'benign' dips. More generally, a technique is sought to predict the tornado burst from OH fluctuations detected by the 'mid' signal.

As explained previously, OH chemiluminescence is proportional to the reaction rate and, thereby, the rate of heat release. Flame degeneration into a tornado mode probably occurs when there are excessive disruptions in this heat release, as caused by localized extinctions. This is conceivable since a premixed flame propagates only when the incoming reactant mixture can be heated to the ignition point in a rapid enough manner. More specifically, flame sustainability requires that the chemical time scale (τ_{chem}) be sufficiently small compared to the flow, or residence, time scale (τ_{res}). The Damkohler number, as defined by Noble et al.[73], provides the necessary nondimensionalized timescale ratio:

$$Da = \frac{\tau_{chem}}{\tau_{res}} = \frac{S_L^2 d}{\alpha U_{ref}} \tag{5.4}$$

In the above equation, S_L is the laminar flame speed, d is a characteristic length, such as the size of the recirculation zone, α is the thermal diffusivity, and U_{ref} is the characteristic velocity scale. The ratio S_L^2/α is also proportional to reaction rate, as per Equation (2.4). Therefore, OH chemiluminescence is essentially a measure of instantaneous Damkohler number, as suggested by the following similarity:

$$\text{OH Chemiluminescence} \sim \text{Reaction Rate} \sim \frac{S_L^2}{\alpha} \sim \text{Da}$$

The above similarity holds when the reference velocity (U_{ref}) remains relatively constant. The Damkohler number is a useful metric to determine the lean blowout margin of the flame. Interestingly, the momentary drops in Damkohler number, which correspond to the dips in OH chemiluminescence, do not necessarily destabilize the flame. The small scale disturbances are probably not severe enough by themselves to cause blowout.

5.4.1 Filtering Mid OH Chemiluminescence Signal

Conceivably, the flame transition to tornado mode and blowout itself are caused when the OH chemiluminescence fluctuations become comparatively 'severe', characterized either as a single, long duration event, or several short fluctuations that occur within a short period of time. In order to test these hypotheses, the OH chemiluminescence signal was filtered with a first order, lowpass filter with varying time constant. The resulting signal excluded isolated, momentary dips, and responded only when several dips occurred close together, or when a single dip had sufficient magnitude and duration.

The first order, lowpass filter was chosen for its simplicity; the filter's time constant, τ, solely governs the dynamic response. The first order low pass is expressed in the Laplace domain as:

$$H_{lp}(s) = \frac{1}{\tau s + 1} \tag{5.5}$$

The time constant τ is the inverse of the cutoff frequency in radians/sec.

Since the filtered signal is sensitive to the more severe and closely spaced events, the filtered signal should therefore correlate better with the high tornado sensor compared

with the unfiltered signal. More specifically, the cross covariance results presented earlier (e.g., Figure 5-7) should produce higher magnitude peaks after filtering. Results of this filter and cross covariance analysis are shown in Figure 5-13. In the figure, the maximum cross correlation over all lag times (abscissa) is plotted for each filter time constant on the ordinate axis. The different curves correspond to different equivalence ratios. The values for zero time constant (i.e. unfiltered signal) correspond to the cross covariance peaks for the 243 mm combustor, presented in Figure 5-7. Evidently, filtering the 'mid' signal with the appropriate parameters can improve the cross covariance with the 'high' tornado sensor. A time constant of about 0.02 seems to maximize the correlation between the filtered signal and the high sensor.

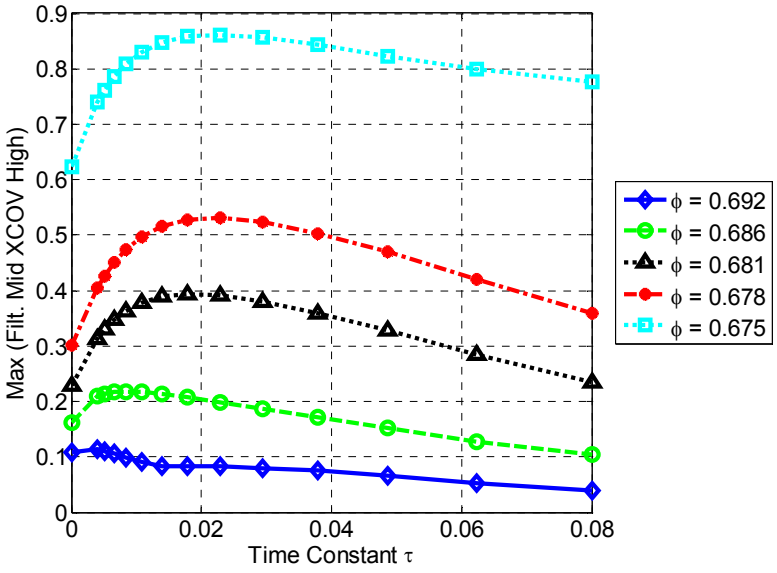

Figure 5-13. Effect of filtering the mid signal with different filter time constants on the cross covariance (XCOV) peak value. Filtering the mid with a time constant of 0.02 provides a considerable improvement from the unfiltered ($\tau = 0$) case. Data shown is from the 243 mm combustor for mean velocity of 2.7 m/s.

A time plot of the 'high', 'mid', and filtered 'mid' signals is shown in Figure 5-14. The low pass filtered signal clearly responds to the more severe fluctuations (at .8,

1.5, and 3.6 sec). The figure shows that the longer duration events are consistent with the tornado bursts detected by the 'high' signal.

Significantly, this method provides a way to detect the tornado bursts by filtering the 'mid' signal. The same 'mid' signal can be thresholded to detect localized extinctions and filtered to predict tornado 'bursts'. Since two precursor types can be detected from the same signal, margin estimation routines can now be more robust. The threshold-sensitive margin, determined by the localized extinctions, can be calibrated in real time using tornado burst predictions. Finally, the effectiveness of filtering confirms that longer duration extinctions and closely spaced, shorter extinctions both will precede the tornado flame transition.

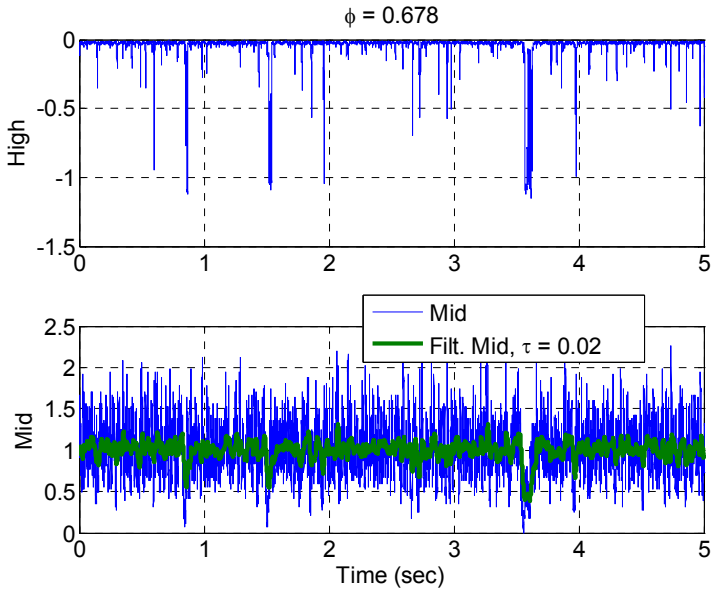

Figure 5-14. Low pass filtering the mid signal to predict tornado bursts, shown in time series. The top plot shows the high signal, which primarily detects tornado bursts, and the bottom plot shows the mid signal and the filtered mid after low pass filtering with time constant 0.02.

5.4.2 Effect of Varying Velocity

The transition to tornado mode was studied in flames stabilized at different flow velocities to better characterize the dynamic behavior. As was discussed in the previous sections, the cross covariance peak between the 'mid' and 'high' sensor signals

corresponds to about the convection time delay between the two sensors. The effect of varying combustor loading was examined by repeating the cross covariance analysis (shown in Figure 5-7) for a range of air and fuel flow rates. The results are shown in Figure 5-15, where the cross covariance is plotted for a set of equivalence ratios for 2.3 m/s (a) and 3.1 m/s (b) mean flow through the combustor. Clearly, the cross covariance peak shifts to smaller lag times as the flow velocity is increased. This verifies the earlier hypothesis that the peak cross covariance occurs at the convective time lag.

The effect of low pass filtering the mid signal was examined as well. Specifically, the filtering analysis (see Figure 5-13) was repeated for a range of mean flow rates in the combustor. The plots shown in Figure 5-16 also show the maximum cross covariance peak as a function of filter time constant. In this case, the velocity of the reactants in the combustor was set at 2.3 m/s (Figure 5-16 (a)) and 3.1 m/s (Figure 5-16 (b)). Note that the peak cross covariance occurs for a filter time constant of 0.02 regardless of flow velocity. This indicates that the OH fluctuations which precede the tornado mode exhibit the same dynamic behavior regardless of flow velocity. Furthermore, the time constant of 0.02, which characterizes the flame and flow response to OH fluctuations, is essentially a response characteristic of the chemical kinetics. In other words, the dynamics of the flame appear to reflect the dynamics of the reaction.

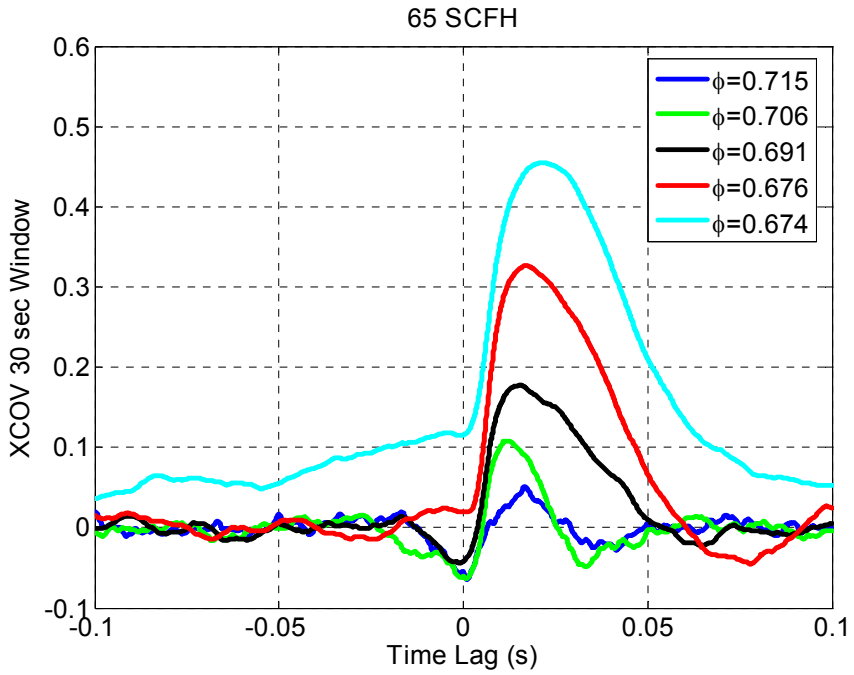

(a) 2.3 m/s

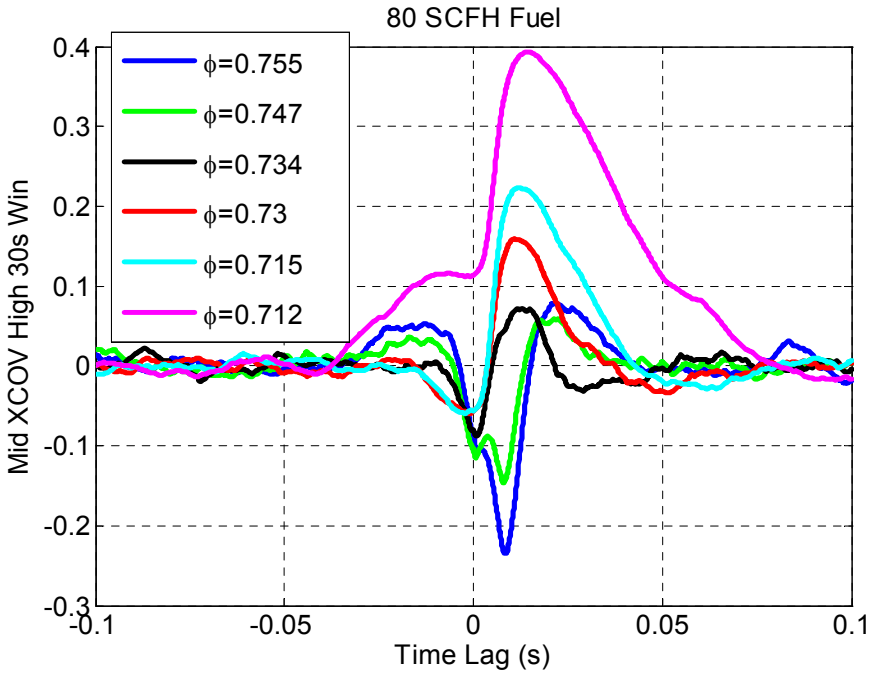

(b) 3.1 m/s

Figure 5-15. Cross covariance of the OH chemiluminescence signal from the 'mid' sensor with the PMT signal from the 'high' sensor for mean flow velocities of 2.3 m/s (a) and 3.1 m/s (b).

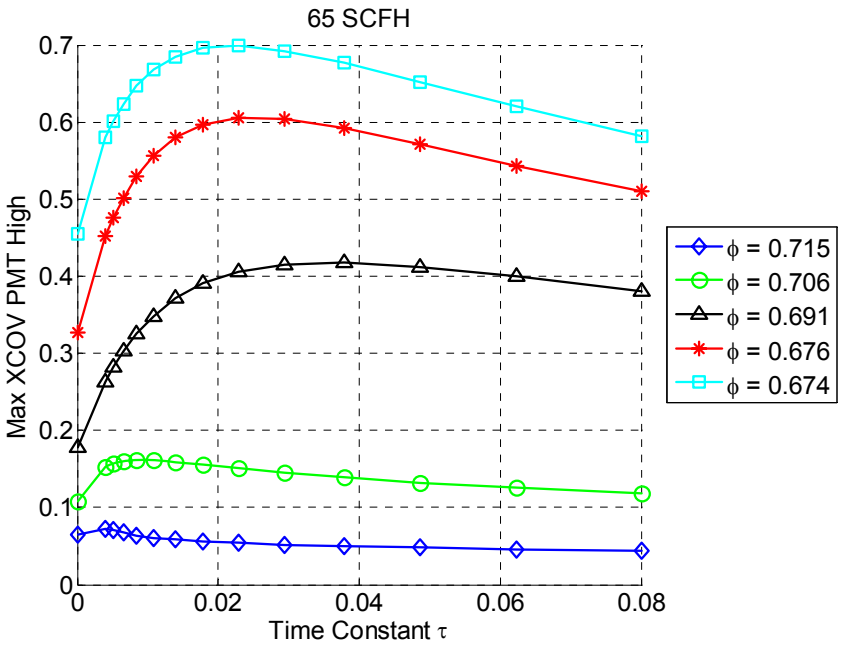

(a) 2.3 m/s

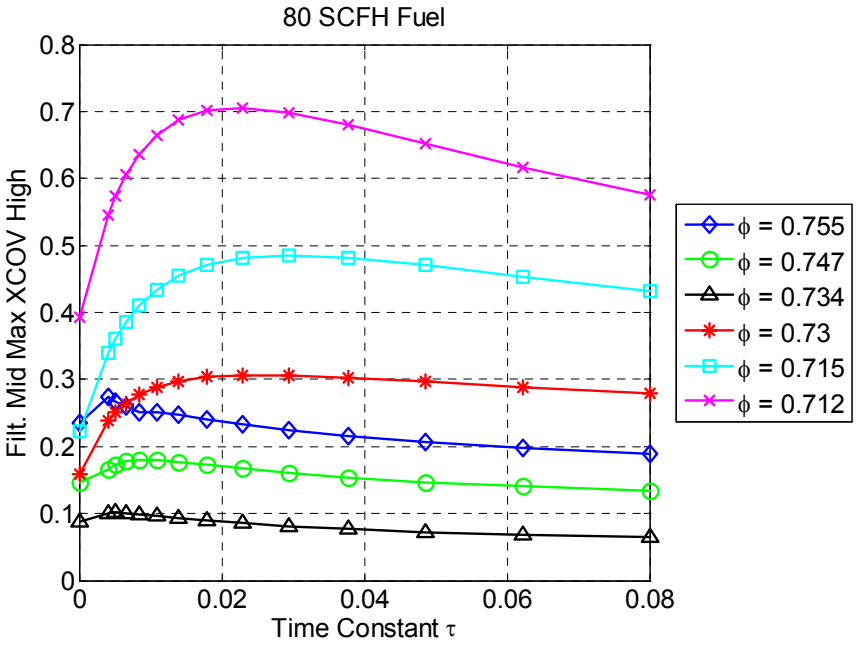

(b) 3.1 m/s

Figure 5-16. The effect of filtering the mid signal with different time constants, as shown for the 243 mm combustor for mean velocities of 2.3 m/s (a) and 3.1 m/s (b). The time constant of 0.02 maximized the cross covariance with the 'high' tornado sensor regardless of flow velocity.

5.5 Perceived Dynamics and Modeling

As was seen in the previous section, low pass filtering the OH chemiluminescence with the appropriate time constant effectively allows prediction of flame transition. The filter and correlate analysis indicates that an identifiable time constant characterizes the flame response to disruptions in reaction rate (as measured by OH fluctuations). The data suggests that the flame shape dynamics are similar to the low pass filter with a time constant of 0.02 sec., since this filter maximizes the correlation between the perturbations (i.e. OH fluctuations) and response (flame transition to tornado mode).

According to the Poincare-Bendixson theorem, a nonlinear system may be approximated as a linear system near equilibrium if perturbation amplitudes are sufficiently small. Hence, while the actual system may not be linear or even purely dynamic, the fact that the flame mode transition can be predicted by a linear filter suggests that such complexities may be neglected as long as the nonlinear bifurcation does not occur. Furthermore, since a theoretical framework for understanding lean flame pulsations does not exist, the simplified first order linear model provides the best characterization of the observed behavior. The first order low pass filter will henceforth be considered a best approximation of flame dynamics while the flame remains in its base stabilized configuration (i.e. 'small perturbations').

The representation of the base stabilized flame as a linear first order system can be used to further understand and analyze its dynamic qualities. A stable, linear, dynamic system will, in absence of perturbations, remain at a point of minimum energy, or equilibrium point. When perturbed, a first order system with the mentioned qualities will decay exponentially to the equilibrium. Similarly, the base-stabilized flame with bubble-type vortex breakdown flow will remain in its configuration in absence of perturbations, and will restore itself exponentially when perturbations occur.

Although the linear approximation becomes invalid once bifurcation occurs, the linear theory can determine the state trajectory up to the point of bifurcation, and

therefore predict the point at which bifurcation occurs. This was verified by analysis that showed how the filtered OH signal predicted the flame shape transition.

5.5.1 Flame Response to Localized Extinction

Thus far, the data show that OH fluctuations can be used to predict flame shape transition via an approximation of the flame as a linear, first order dynamic system. This model can be tested by considering flame response to the detected localized extinctions in the OH signal. The detection of localized extinction events is a characterization of OH fluctuation that was used to detect blowout margin. The 'events' were declared whenever the signal, when not already in an event, crossed a threshold and triggered an alarm. If OH fluctuations in general precede flame transition, the number of threshold crossing events (or 'alarms') should increase before tornado mode as well.

The alarm signal is binary; at each time sample it is either '1', indicating a threshold crossing and beginning of an event (as seen in Figure 5-9), or '0' otherwise. The alarm signal is sampled at the same rate as the OH chemiluminescence signal. Hence, a '1' in the alarm signal that declares the beginning of an event will always be preceded and followed by a '0'. The alarm signal as a whole is therefore a train of impulses whose separation in time is described by an exponential distribution, as was shown in the analysis of section 5.02. A linear, first order lowpass system's response to an impulse is shown in Figure 5-17. Mathematically, the impulse response is described by the transfer function expressed in Equation (5.5). In the time domain, Equation (5.5) becomes:

$$y(t)=(1-e^{-t/\tau})*u(t) \qquad (5.6)$$

Equation (5.6) states that the output (y) of the filter is a convolution (denoted by '*') of an exponential decay and the input (u). A train of impulses that are spaced close together relative to the time constant will cause y(t) to grow. Conversely, impulses that are spaced far apart relative to the time constant will not significantly affect y(t).

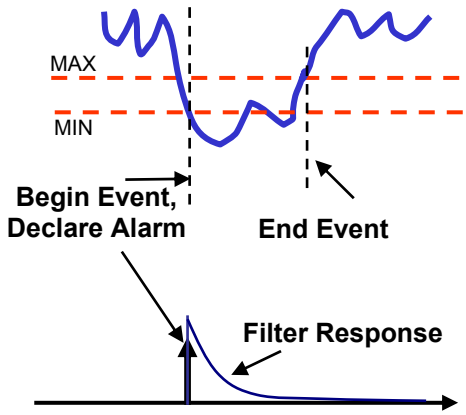

Figure 5-17. Illustration of the filter response to an alarm, which appears as an impulse at the beginning of each event.

To determine whether the number density, or frequency, of localized extinctions increases before a tornado burst, the alarm signal was cross correlated with the tornado-detecting 'high' signal. The results of this analysis are shown in Figure 5-18. Once again, the peak cross covariance occurs for a time constant of 0.02 seconds. Since events are indicative of the identifiable 'dips' in OH, the analysis confirms the conclusion drawn earlier that OH fluctuations will precede tornado bursts. Furthermore, the figure indicates that the number of detectable events will increase immediately preceding a tornado.

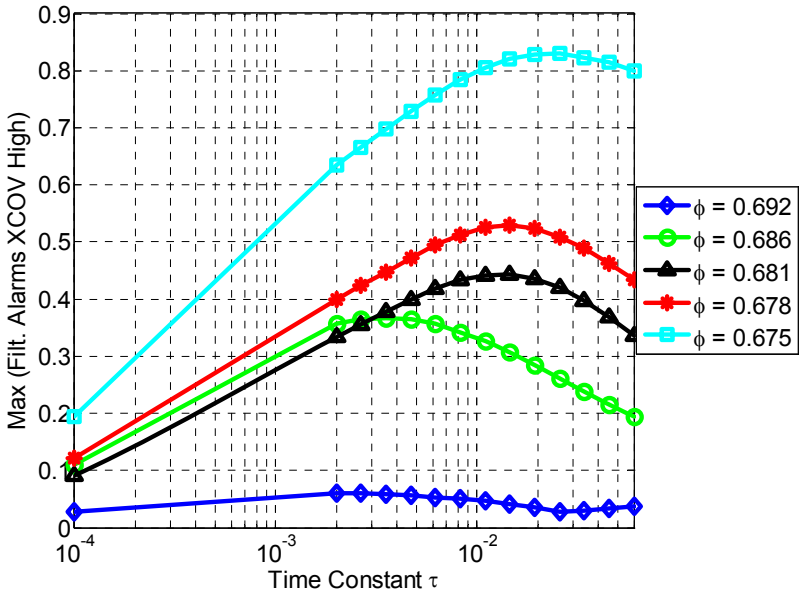

Figure 5-18. Plot showing the cross covariance between the filtered the alarm signal and the tornado detecting 'high' signal. The alarm signal is a train of impulses; the filter is a first order lowpass with time constant τ. At certain time constants, the cross correlation peaks, indicating that the number of localized extinctions will increase before a tornado burst.

According to Muruganandam, the vortex breakdown 'bubble' is sustained by the combustion inside the bubble. The resulting expansion causes the incoming flow to exchange axial momentum for radial momentum. When the combustion in this zone is weakened, the axial velocity of the incoming flow is not effectively converted, and the bubble transitions. The transition is followed by a transition to the double helical, or 'tornado' mode.

Since flame transition is preceded by OH fluctuations detectable as localized extinctions, it is evident that the localized extinctions and/or other events that cause OH fluctuations perturb the heat release inside the bubble, as affect its strength. A weakening bubble may then collapse as per Muruganandam's explanation.

5.5.2 Modeling Flame Behavior

The observed dynamics of the flame appear to describe the response of a linear first order dynamic system for small perturbations. In essence, the flame will favor a base-stabilized state when the perturbations are sufficiently small. The base stabilized configuration can be considered a stable equilibrium, and the OH fluctuations are a measure of the perturbations.

A nonreacting, swirling flow also exhibits similar dynamic behavior. In their theoretical analysis, Wang and Rusak found that for subcritical rotation rates ($\omega << \omega_0$), a swirl flow will stabilize about a columnar flow configuration with a specific swirl number. The results of their analysis are presented in Figure 5-19. The dynamic equilibrium states, which corresponded to steady state solutions of the Squire-Long Equation (see Equation (2.5)) was characterized as a point of minimum flow energy; perturbations that added energy were soon dissipated as the flow returned to the columnar state. Upon increasing the rotation rate ($\omega_0 < \omega < \omega_1$), the energy curve transformed from monotonic with a single minimum to a curve with a global and a local minima. The local energy minimum corresponded to a bubble-type vortex breakdown flow structure. This local minimum tranformed into a global minimum as the fluidic rotation rate was further increased ($\omega > \omega_1$).

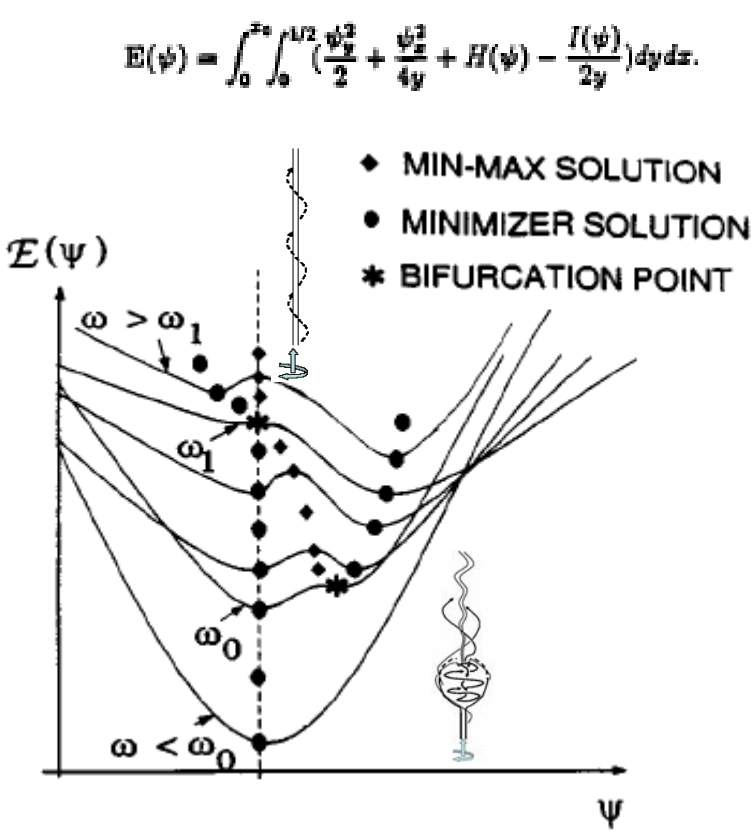

Figure 5-19. Energy diagram depicting favored modes of a nonreacting flow at varying angular rotation (ω) values. The total momentum energy of the flow, E(Ψ), is plotted versus the stream function (ψ). When the rotation reaches a critical value (ω=ω$_0$), the vortex breakdown flow emerges as an alternate flow configuration. At sufficiently high rotation (ω>ω$_1$), the breakdown state is the only stable configuration. Image adopted from Wang and Rusak.[36]

The swirl and dump stabilized flame behaves in a similar manner. At stable equivalence ratios, the flame and flow correspond to the 'bubble' type vortex breakdown. At sufficiently lean conditions, flame pulsations are evident as a new flame configuration (i.e., tornado) is observed. The OH fluctuations are a measure of disturbances that force the flame away from the base-stabilized shape. When the disturbances are sufficiently severe or frequent (as characterized by the response of a low pass filter) the system has enough energy to transition to the alternate minimum configuration, which is the tornado mode.

The observations of lean flame behavior can be combined with the understanding of its dynamics near equilibrium and swirl flow theory to develop a more comprehensive understanding. An energy diagram similar to the one presented for swirl flow is shown for swirl stabilized reacting flow in Figure 5-20. Contours are plotted for constant Re_D. The OH fluctuations at lean conditions are a measure of the perturbations in this model, and the base-stabilized flame shape with bubble-type vortex breakdown flow (depicted at A) and the tornado flame shape with double-helical vortex breakdown flow (at C') are the two equilibrium states. Disturbances such as localized extinction events can perturb the flame from base-stabilized (A) to an unstable, quasi-tornado state (B), and eventually to the double helical tornado flame (C). The weakened reaction in the tornado flame causes a decrease in the combustor temperature. The cooler flow has lower viscosity, and therefore, higher Reynolds number (Re_D). The net effect is analogous to increasing the rotation rate in a nonreacting flow. The flow transitions to a higher contour in the energy diagram (i.e., from C to C') due to the increase in Re_D. The transition from a base stabilized flame to tornado flame is shown in Figure 5-20 with solid arrows.

However, if the flame state arrives at C' with sufficient residual energy, the quasi-tornado state can reemerge (B'). Note that the transition from C' to B' requires less energy than the transition from C to B. Once the state is at B', the size of the inner recirculation 'bubble' increases. The concentration of heat and radicals at the base will enhance the reaction and flame anchoring. The higher temperatures will result in an increase in viscosity and a reduction in Re_D. Hence, the state transitions to a different energy contour, from B' to B. The transition back to A becomes complete when the growing recirculation near the base can sustain a reaction strong enough to reestablish a

base stabilized flame. The return to a base stabilized flame is shown in Figure 5-20 with dash dot arrows.

According to the analysis presented in Section 5.3.2, the tornado duration must be bounded if the flame is to recover. It was proposed that the combustor cools during the tornado burst, and prolonged cooling inhibits reestablishment of the base-stabilized flame. Extinction likely occurs when the tornado duration exceeds a critical value. Furthermore, the cold flow swirl number, 0.66, indicates that the bubble-type vortex breakdown is the stable configuration post-extinction. Thus, the flow must return to the 'bubble' type vortex breakdown state from the double-helical tornado state after extinction.

The return to the bubble type vortex breakdown can be described in the following manner. As the combustor cools during a prolonged tornado episode, flow viscosity decreases and Re_D increases for the same velocity. Hence, the state transitions to a contour with higher Reynolds number, from C' to C". Since C" is dynamically unstable, the state must stabilize at A", which is the cold flow bubble-type vortex breakdown. This transition is shown in Figure 5-20 with dotted arrows, from C' to C", and to A".

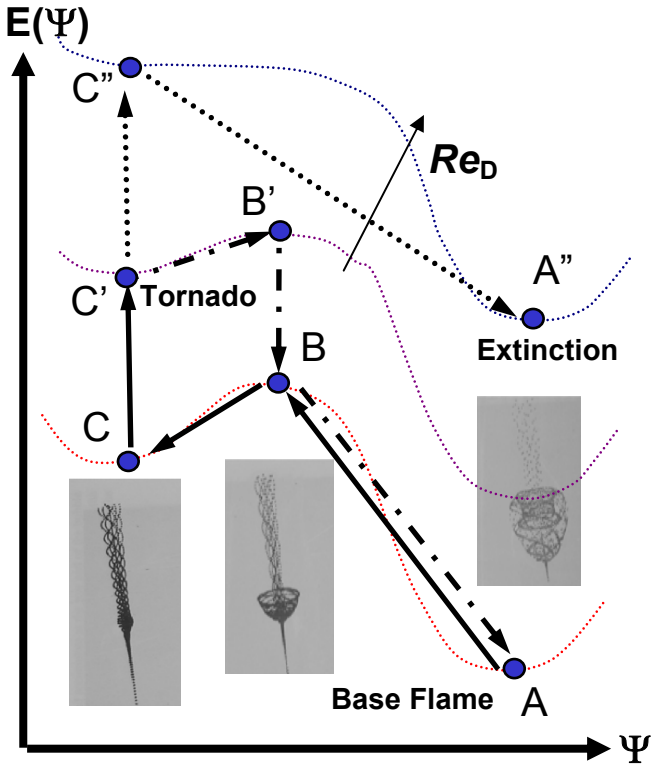

Figure 5-20. Energy diagram for a swirl and dump stabilized flame, showing contours of constant Re_D, plotted versus stream function (ψ). Flame perturbations such as localized extinctions increase at lean conditions. These disturbances may cause the flame to transition from base-stabilized (A) to an unstable quasi-tornado state (B), and eventually to tornado (C'). If the tornado flame persists, the combustor cools and the flame extinguishes (C" and A").

CHAPTER 6. MARGIN ESTIMATION

Margin estimation is critical for lean blowout mitigation. Even in the absence of active control, techniques are needed to asses the health of a combustor and determine the probability of flame loss. This chapter discusses techniques to determine blowout margin in the swirl and dump stabilized combustor based on perceived flame behavior, such as localized extinctions and inner recirculation zone dynamics. Margin estimation is an extension of flame detection, which is discussed in Chapter 4, and involves the incorporation of flame dynamics, which is covered in Chapter 5. Signal processing and dynamic estimation techniques are the focus of this chapter.

6.1 Mapping Event Frequency

Chapter 4 discussed techniques for identifying localized extinction events via acoustic and optical methods. It was noted that such events occur more frequently with diminishing margin. Developing a reliable margin estimate from the frequency of localized extinctions requires resolving two issues. First, for a given safety margin (i.e., $\Delta\phi = \phi - \phi_{LBO}$), the margin estimate should be constant regardless of operating condition. Second, the frequency of discrete events must be determined in a rapid and reliable manner.

While the frequency of localized extinctions are affected by equivalence ratio, the effect of factors such as air flow rate and fuel split must also be elucidated as well in order to develop a robust margin detection technique. Results of varying the air flow rate to the combustor are shown in Figure 6-1. The top plot shows the equivalence ratio variation over time, and the middle plot displays the bandpass filtered acoustic signal,

obtained using the techniques covered in Chapter 4. The threshold crossing frequency was computed in a moving window summation. The 'alarms per second' value (γ_{1sec}) was computed at a given time instant by summing the total threshold crossings over the previous 1 second. This parameter is displayed in bottom plot of Figure 6-1.

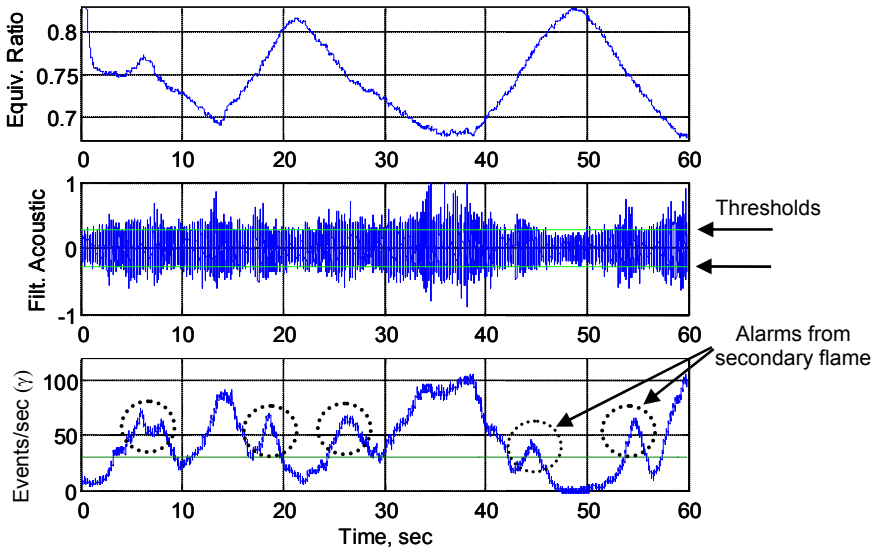

Figure 6-1. Characteristics of a flame undergoing air flow variations over time. The equivalence ratio is shown in the top plot and the bandpass filtered acoustic signal (10.61 to 95.49 Hz) with thresholds is shown in the middle plot. The bottom plot displays the number of events per second, as computed by a one second moving window.

Generally, the frequency of threshold crossings (events) increases as the flame approaches its LBO limit and vice versa. However, there is an intermediary increase in the events per second as the secondary 'torus' flame in the recirculation zone also exhibits LBO precursors. After the secondary flame extinguishes (below an equivalence ratio of approx. 0.75) the relationship between events per second and equivalence ratio becomes quasi-linear again.

The results indicate that below a certain equivalence ratio, the threshold crossings increase linearly with proximity to the LBO limit, causing the events per second signal to mirror the time dependence of the equivalence ratio. The events per second signal can

now be used as a basis of mitigation techniques that sense the onset of LBO and improve safety margin.

Figure 6-2 shows how changing the fuel split ratio (i.e., the percentage of fuel that is redirected toward the central, premixed pilot) affects the number of detected events per second, as detected by the acoustic signal. While the blowout limit shifts to leaner equivalence ratios with increasing pilot fraction, the number of detected events per second remains constant regardless of the fuel split. This verifies that the event frequency alone can determine blowout margin regardless of pilot fuel fraction.

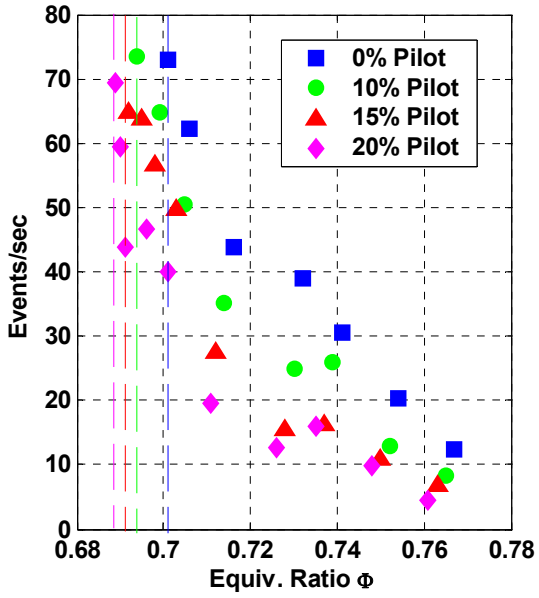

Figure 6-2. Effect of pilot fraction on the LBO limit, as determined by acoustic based sensing. Increasing the fraction of fuel directed to the pilot effectively shifts the LBO limit to leaner equivalence ratios. Note that the same number of events per second occur at blowout regardless of pilot fraction.

6.2 Signal Processing

Since the system's LBO margin is determined by event frequency (i.e. number of events per second), an efficient method is required to calculate this parameter. In this

section, different methods will be investigated for determining event frequency in real time.

The following nomenclature will be used to simplify the explanations. A is the alarm signal. It consists of a series of '1's and '0's in time, where '1' indicates the beginning of an event. γ is the alarm frequency, or alarms per unit time, which will be calculated using different algorithms, and f' is the sample frequency, in Hertz.

6.2.1 *'Moving Window' One Second Summation*

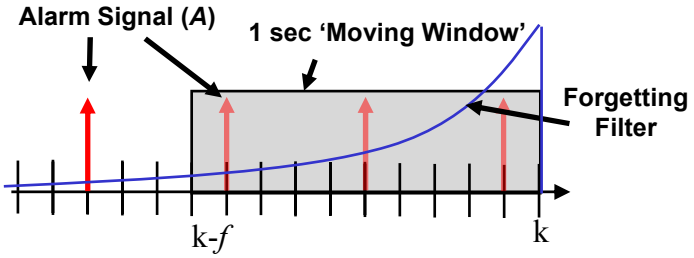

Figure 6-3. Schematic explaining the different filters used for alarm averaging. The alarm signal (A) is either 1 or 0 in time indicating when the signal crosses the threshold. The one second 'moving window' summation weights all alarms in the window equally while the forgetting filter favors the more recent time samples.

The simplest way of determining the number of events per unit time is to sum the number of threshold crossings in a moving, one second window. The number of events per second determined at the k^{th} time instant is the sum of all events over the previous one second:

$$\gamma_{win}(k) = \sum_{n=0}^{f} A(k-n)\,, \tag{6.1}$$

which can be implemented recursively as:

$$\gamma_{win}(k) = \gamma_{win}(k-1) + A(k) - A(k-f-1) \tag{6.2}$$

Determination of the alarm frequency with a one second moving window summation was shown for varying air flow rate in Figure 6-1. Figure 6-3 shows a schematic of the moving window which sums all alarms over the previous one second.

The one second sum may also be represented as a discrete transfer function in the z-domain:

$$H_{win}(z) = \frac{\Gamma_{win}(z)}{A(z)} = \frac{z^{f+1} - 1}{z^{f+1} - z^{f}}, \tag{6.3}$$

The transfer function represented by Equation (6.3) relates output (threshold crossings over previous 1 second in the z-domain, $\Gamma_{win}(z)$) to the input (threshold crossing flag in the z-domain, A(z)). Figure 6-4 shows the frequency response of the one second summation for different sampling frequencies. Clearly, as the sample frequency increases, the frequency response of a one second summation filter approaches that of a zero order hold, which is shown in cyan in the figure. Used for digital to analog conversion, the zero order hold (ZOH) operation holds a sampled signal's value for the time interval until the next value becomes available. The periodic frequency response imposed by the ZOH is normally corrected with a low pass filter. The zero order hold has the following continuous time transfer function representation :

$$G_{h0}(s) = \frac{1 - e^{-Ts}}{s} \tag{6.4}$$

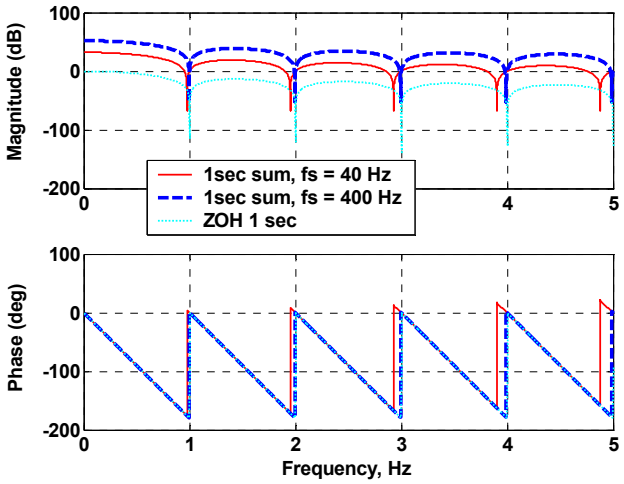

Figure 6-4. Frequency response of one second summing windows at 40 and 400 Hz sampling frequencies, compared with a 1 second zero order sample and hold (ZOH).

Discrete, sampled signals have a periodic frequency response, with a "folding frequency" at the Nyquist frequency (half the sample frequency). However, in this case, the Nyquist frequency of the summation signals shown in Figure 6-4 (20 and 200 Hz for the two cases) are well above the frequency where the periodicity first occurrs (1 Hz). As sampling frequency is increased, the frequency response of the moving window summation appears more identical to the 1 second zero order hold, differing only by a DC offset. The periodic frequency response produces undesirable amplification of higher frequencies. The response time remains of the order of 0.5 seconds, irrespective of the sampling frequency. To improve the response time, the window can be truncated to a 0.5 or 0.25 second moving window summation. However, the effects of digitization will persist: the frequency response will remain periodic, and high frequencies will be not be properly attenuated.

6.2.2 Forgetting Filter

The calculated time response and frequency characteristics of the event frequency may be improved by choosing an appropriate 'forgetting' filter. Such a filter accentuates

recently measured data over previously measured data. The forgetting filter used to calculate event frequency in this study is given by:

$$\gamma_{ffilt}(k) = L\sum_{n=0}^{\infty} \zeta^n A(k-n), \tag{6.5}$$

which can be implemented recursively as

$$\gamma_{ffilt}(k) = L\left[A(k) + \zeta \cdot \gamma(k-1)\right] \tag{6.6}$$

The forgetting parameter, ζ, is set to some value between 0 and 1. The filter scales the current input by 1, the input at the previous sampling instant by ζ, the input two samples ago by ζ^2 and he input n samples ago by ζ^n. The weighted values are theoretically summed over an infinite history of weighted inputs and multiplied by an overall gain (L). In practice, the filter is implemented recursively as shown in Equation (6.6). For $0<\zeta<1$, the forgetting filter "exponentially forgets" old values and gives recently measured samples maximum weighting. An illustration of the exponentially diminishing weights is shown graphically in Figure 6-3 and compared with the one second summation, which weights all data in the window equally. The forgetting filter assigns greater importance to recent data and hence is more responsive to rapid changes.

The forgetting filter may also be represented as the following discrete transfer function:

$$H_{ffilt}(z) = \frac{\Gamma_{ffilt}(z)}{A(z)} = \frac{Lz}{z-\zeta} \tag{6.7}$$

For stability, the parameters must be chosen so that the transfer function in Equation (6.7) has singular values (poles) within the unit circle. Hence, ζ must be between -1 and 1 for stability. Since the filter is intended to handle the input over time in an accumulative manner, all the weighting values (ζ^n) must be positive for all integers n, and therefore ζ

must be positive. If the ratio is set to 1, the filter becomes an accumulator; i.e., the input is continually summed and there is no exponential decay of previously measured data. A value less than but close to 1 can provide the desired summing characteristic. A frequency response plot of the forgetting filter is presented in Figure 6-5. Unlike the moving window summation, the frequency response is not periodic below the Nyquist frequency and higher frequencies are more completely truncated. Furthermore, the 1 second summing window had a bandwidth of 0.44 Hz, compared to the 'forgetting filter' bandwidth of 0.8 Hz.

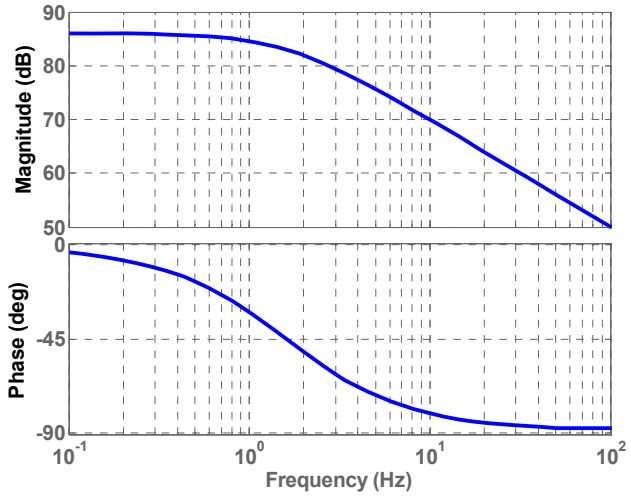

Figure 6-5. Frequency response of the 'Forgetting Filter' transfer function used to determine event frequency, for ζ=0.9995 and L=1.125*10^6. The response is similar to a first order lowpass filter with time constant τ=0.2 and K=2.25*10^4.

Note the similarity of the forgetting filter frequency response with a continuous, first order lowpass filter. Indeed, the discrete transfer function in Equation (6.7) can also be expressed as a first order lowpass in the continuous domain. The approximation is valid for frequencies sufficiently lower than Nyquist (5 kHz in this case). The Laplace representation of Equation (6.7) is

$$H_{ffilt}(s) = \frac{\Gamma_{ffilt}(s)}{A(s)} = \frac{K}{\tau s + 1}, \tag{6.8}$$

where the DC gain K and time constant τ are related to the filter parameters as follows:

$$K = \frac{-L}{f \cdot (\ln \zeta)} \tag{6.9}$$

$$\tau = \frac{-1}{f \cdot (\ln \zeta)} \tag{6.10}$$

From Equations (6.9) and (6.10) it is evident furthermore that $L = K / \tau$.

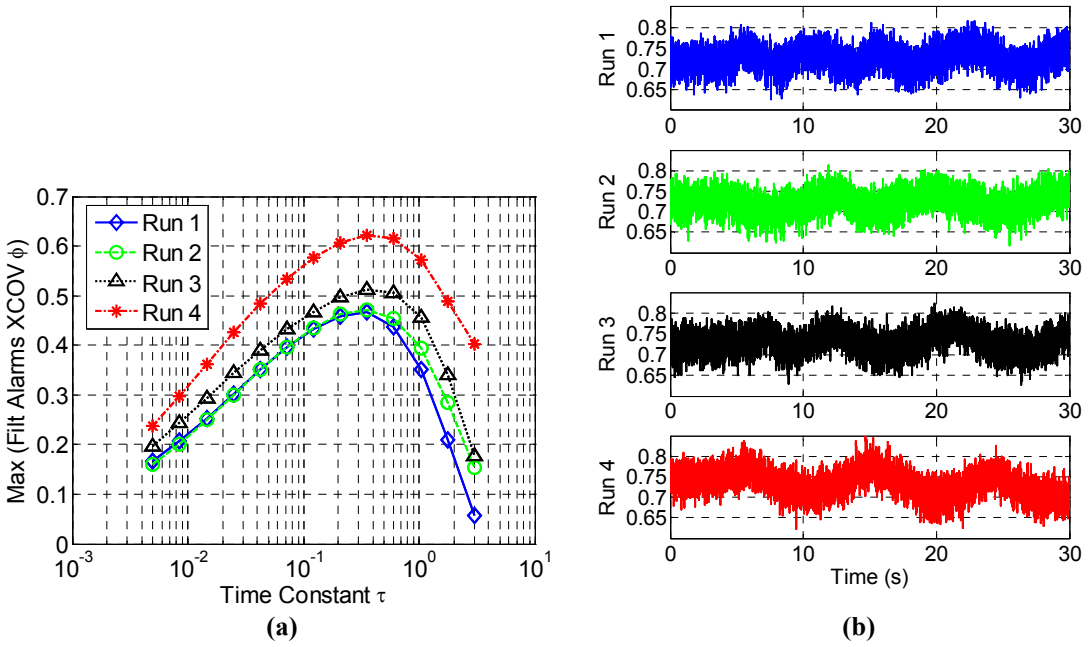

Figure 6-6. Determination of the optimal forgetting filter time constant. The alarm signal was filtered with a first order lowpass with varying time constant, and then cross correlated with the equivalence ratio. The results are plotted for a set of runs over a range of time constants (a). The time trace of each run is shown as well; equivalence ratio as computed with an air flow orifice meter is plotted versus time(b).

In this study, the optimal value for ζ was empirically determined by filtering the alarm signal using the lowpass continuous filter in Equation (6.8) and correlating the filtered signal with the equivalence ratio, as determined using an air flow sensor signal. The implication is that since the equivalence ratio is indicative of the LBO margin, correlation with equivalence ratio translated into correlation of the filtered response to

margin. The results are shown in Figure 6-6; the plot on the left (a) shows the results of the filter and correlate operations while those on the right show the time traces of each run's air flow sensor signal. Clearly, time constants in the range between 0.2 and 0.4 (corresponding to ζ=.9995 and ζ=.9998, respectively) produce the maximum correlation with equivalence ratio. However, this could be a result of the limitations of the air flow rate sensor. The sensor was an orifice meter; air flow was computed using the pressure difference between the upstream and downstream sides of the orifice. The noisy signal is probably limited in its dynamic range; hence, higher frequencies cannot be clearly detected. Undocumented observations suggest ζ values between 0.9995 and 0.9996 produce the best estimate of blowout margin.

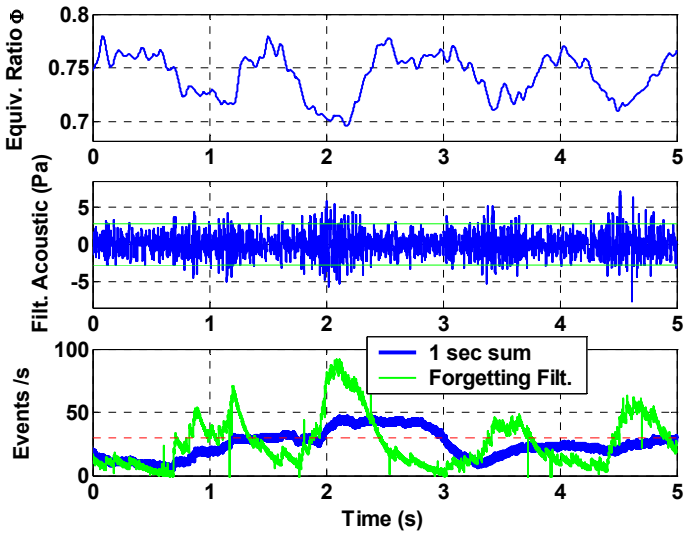

Figure 6-7. Characteristics of an unpiloted flame undergoing equivalence ratio variations over time. The equivalence ratio is shown in the top plot and the bandpass filtered acoustic signal (10.61 to 95.49 Hz) is shown in the middle plot. The bottom plot compares the 1 second moving window event summation with the result produced by the forgetting filter with ζ=0.9995.

A comparison of the performance of the 1 second moving window and the forgetting filter is presented in Figure 6-7. In this case, the air flow rate was varied manually at about 1 Hz. The 1 second moving window was unable to capture the variation while the forgetting filter was able to replicate it.

6.3 Issues in Estimation

Margin detection methods for blowout mitigation have largely relied on discrete events such as localized extinctions or other blowout precursors, such as tornado bursts. This approach has been pursued because precursor detection provides a direct gauge of the combustor stability. A combustor is nominally operated within some safe parameter space determined by equivalence ratio and velocity; these may be monitored separately to map the operating point in relation to the blowout limit. However, precursor detection offers a simpler alternative; the existence of precursors is indicative of dangerous situation from which recovery is mandatory. Once the flame is no longer in danger of blowout, the nominal combustor-operating control can resume.

This section considers the robustness and effectiveness of relying on localized extinctions and tornado bursts to determine the LBO margin. The experimental setup discussed in section 5.2.1 will be referred to with the aim of analyzing the effectiveness of the sensor signals.

6.3.1 Sensing Robustness

Several issues must be addressed in order to determine a margin detection routine's effectiveness and reliability. The first issue is sensor placement. Optical based methods in particular are highly sensitive to sensor location; Muruganandam has shown that an optical sensor's field of view affects the number of detected precursors. To address this limitation, acoustic approaches have been developed, but acoustic signals are also affected by placement, though to a lesser degree.

A second issue that limits the effectiveness of margin detection is observability. Blowout precursors should be identifiable in the signal with a minimum of false alarms.

This means that the threshold values must be set judiciously. As was seen in Figure 5-4, and Chapter 5, tornado bursts are clear features in the signal from a photomultiplier placed downstream of the main flame zone ('high' sensor). By contrast, the localized extinctions, as detected by an OH-filtered photomultiplier further upstream, were relatively more ambiguous ('mid' sensor). Therefore, discerning a tornado burst with a threshold was much more straightforward in the 'high' signal compared to distinguishing a localized extinction in the 'mid' signal.

Figure 6-8 shows the effect of translating the threshold on the number of threshold crossings in a 30 second time window for both the 'mid' and 'high' signals. At equivalence ratios greater than 0.657, the curves for the high signal appear comparable as the threshold value is altered. Furthermore, no events appear in the signal for all threshold levels when the equivalence ratio is 0.661 or greater. This indicates that the condition where tornado is first evident ($\sim\phi = 0.657$) can be determined without much regard to the precise threshold level.

In contrast, the entire threshold crossing curve translates significantly when the mid threshold value is changed (Figure 6-8, bottom). Clearly, threshold placement has a greater effect on detecting localized extinctions than detecting the number of tornado bursts. This threshold level ambiguity is compounded in a blowout mitigation application, where the critical number of threshold crossings over a given time frame must be declared explicitly. If the threshold is adjusted, the critical number of tolerable events must be adjusted as well, and the entire control system may need to be retuned to the updated values.

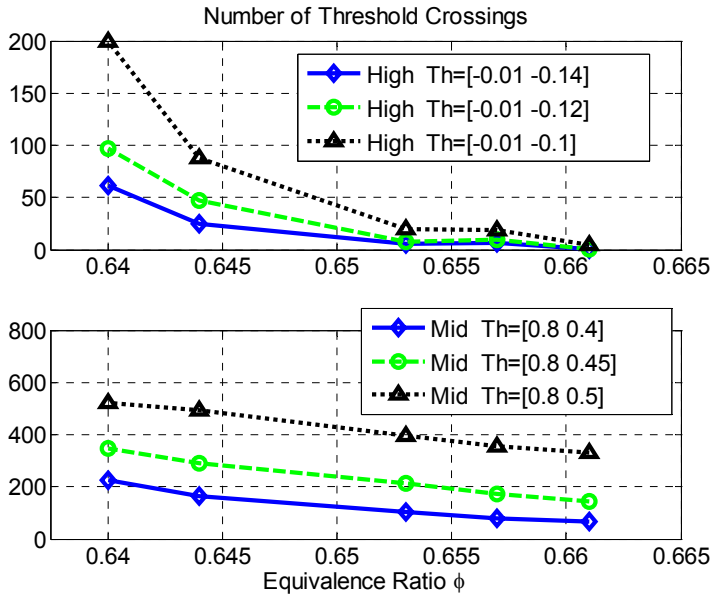

Figure 6-8. Effect of translating the lower threshold (second Th value) on the number of detected threshold crossings over 30 seconds in both the high (top) and mid (bottom) signals. Data obtained from 127 mm combustor.

The third issue affecting margin detection effectiveness is the speed of the detection routine. LBO mitigation strategies are limited by the rate at which meaningful data can be collected and processed. Since blowout mitigation is in essence a safety net intended to safeguard against mishaps in operating adjustments or rapid, undetected disturbances, the speed (i.e., bandwidth) of this safety net becomes critical. Thus, margin estimation routines should be as efficient as possible.

The fourth issue is generality. A margin detection scheme should be effective across the entire range of operating conditions in the combustor, and should remain effective when blowout avoidance measures are in effect. Blowout mitigation techniques that attempt to restabilize the lean flame without increasing power rely on methods which alter the flow characteristics of the combustor, such as fuel redistribution, swirl modulation, or plasma assist. Once the flow has been altered, the margin detection scheme associated with a particular actuation type should not lose effectiveness while the actuation is in effect.

The fifth issue is survivability. Sensor failure poses a serious problem for any control system. The margin detection routine should therefore rely on as few sensors as possible in order to allow for redundancy and robustness.

6.3.2 Margin Estimation Using Localized Extinctions

With the described criteria, precursor detection techniques can be critiqued with regards to their ability to effectively estimate margin. As stated previously, the detection of localized extinction precursors via OH chemiluminescence is strongly affected by sensor placement and the signal thresholds. In order to address the placement issue, acoustic methods have also been developed to detect localized extinctions, as explained in Chapter 4. Hence, the first issue has been partially addressed. In section 6.2.2, a 'forgetting' filter was shown to rapidly detect margin based on localized events; this procedure addresses the third issue. It was also shown that for fuel split actuation, the margin determination technique remains effective. This addresses the fourth issue. Finally, since detection of localized extinctions is possible with a single sensor, the fifth issue, survivability, is addressed.

The remaining key issue with localized extinction is its observability. As was seen in Figure 6-8, there is ambiguity regarding the proper placement of the threshold. Furthermore, there is also ambiguity regarding the significance of the threshold violation. In the reported experiments, 0.66 was still a 'stable' equivalence ratio; i.e., the flame was not in danger of imminent blowout. This is confirmed by the fact that there are almost no tornado bursts detected by the high signal. Yet, there are still a considerable number of localized extinction events, or what appear to be such events detected as threshold crossings of the mid signal. Either there are random dips in chemiluminescence that are

not extinction-related or extinctions also occur, at slightly diminished rates, at 'stable' conditions as well.

Since the principal issue here is developing a margin detection technique, the performance of the mid signal will be addressed in that capacity. Looking at the bottom plot in Figure 6-8, the ambiguity is in terms of offset; the number of threshold crossings will increase with diminishing margin regardless of the threshold level. Furthermore, the rate of increase appears fairly constant over equivalence ratio to the extent that it may be termed somewhat linear.

6.3.3 Margin Estimation Using Tornado Bursts

The high signal events have less ambiguity than the mid events. Tornado bursts are clear distinct features in the signal that are easily detected using thresholds. Furthermore, since the tornado mode is part of the blowout process, the existence of a burst is a clear signal of danger.

While tornado based detection is unambiguous, there are several drawbacks. First, there is a field of view limitation; acoustic methods do not yet exist for detecting tornado bursts. Second, the spacing of tornado burst events are much larger than the spacing of localized extinction events, as shown in Figure 5-10 and Figure 5-11, and this will adversely affect the rate at which margin can be determined. Third, while tornado events are a clear indication of blowout proximity, the phenomena are nonexistent at stable equivalence ratios. It is therefore possible to transition from stable to marginal without any warning. Only within parameter spaces close to blowout will there be any indication of diminishing margin, and when the margin information comes there may not be enough time to prevent flame loss.

From a control perspective, tornado based detection is undesirable because the signal does not increase linearly with diminishing margin. Therefore, it is difficult to stabilize the operating point with feedback based on tornado events alone. There is also a tendency for the state to drift due to the long delays required to estimate margin. If disturbances have sufficient amplitude or if the state transitions too rapidly, the delay would render the controller powerless to stabilize the flame.

6.3.4 Incorporating Flame Dynamics

Each precursor type provides unique information about the blowout margin. As explained in the following sections, this dual information stream can be combined to enhance overall determination of margin. However, information about both tornado bursts and localized extinctions are only directly attainable using separate, dedicated sensors, as discussed in Chapter 5. While using two sensors reduces the uncertainties in margin estimation, the drawbacks of cost, complexity, and vulnerability may outweigh the advantages.

Fortunately, both localized extinctions and tornado bursts can be detected using the same signal stream from a single sensor. As discussed in section 5.4.1, filtering the OH chemiluminescence signal from the 'mid' signal enabled prediction of the tornado bursts. Hence, while the unfiltered 'mid' signal can be thresholded to detect localized extinctions, the filtered 'mid' can be thresholded to identify the tornado bursts.

Since it is intended as a tornado sensor, the mid signal should exhibit large variation in a narrow parameter space near blowout, and reduced variation elsewhere. Figure 6-9 shows the standard deviation of the filtered signal, normalized by the standard deviation of the same signal at the richest recorded case. Plots are shown for both the 127 mm (a) and 243 (b) combustors. The normalized standard deviation of the unfiltered

signal is also plotted for comparison. It is clear that the normalized standard deviation of the filtered signals increase at a higher rate than the unfiltered signal.

Figure 6-10 shows the number of detected threshold crossings, or events for the filtered mid signal versus equivalence ratio for the 243 mm combustor. The results are plotted for a range of threshold values. Clearly, the threshold sensitivity is not as great as the unfiltered mid signal. However, the number of detected events is lower. Both of these are also characteristics of the tornado 'high' sensor. The result verifies that the filtered 'mid' signal can substitute for the tornado sensor in determining when the combustor is critical.

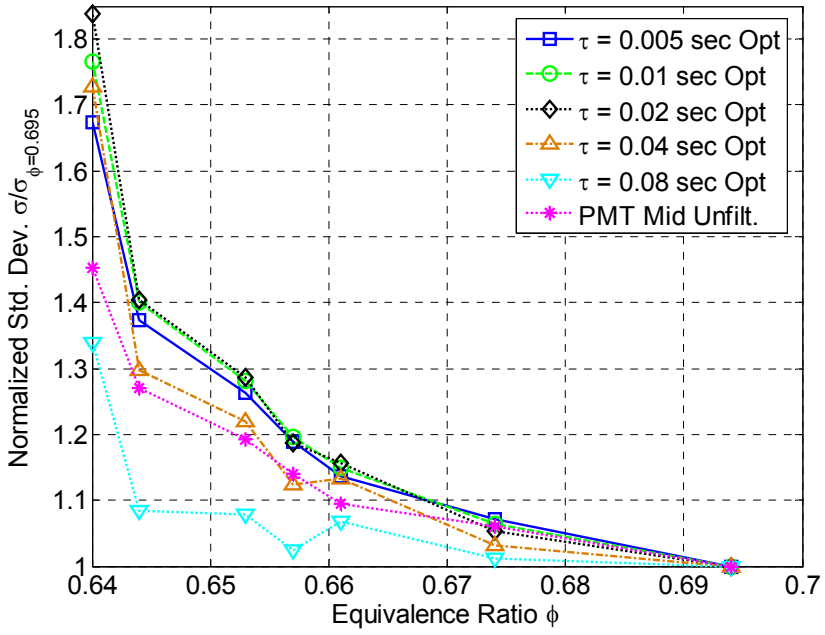

(a) 127 mm combustor

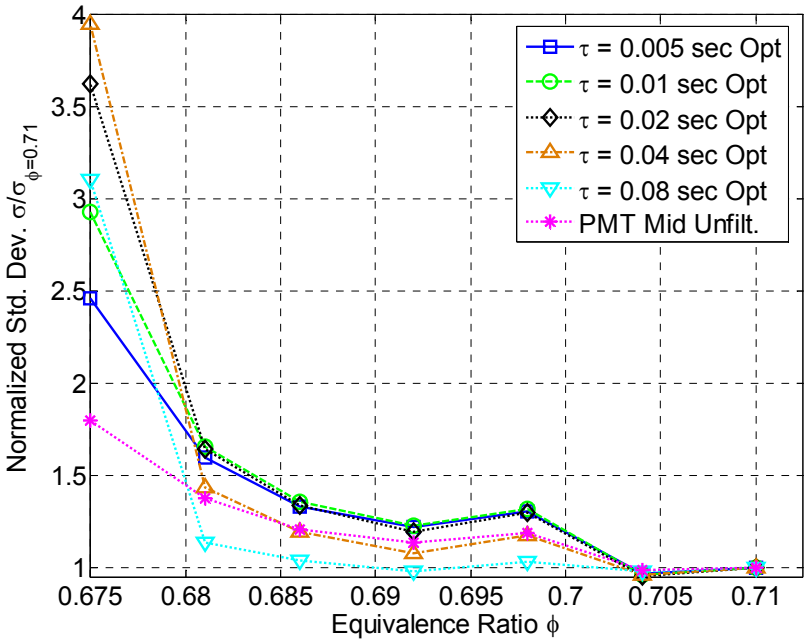

(b) 243 mm combustor

Figure 6-9. Normalized standard deviation of the filtered OH chemiluminescence 'mid' signal versus equivalence ratio, for a set of filter time constants. The filter is a first order lowpass; standard deviation values at each equivalence ratio are normalized with the standard deviation at the 'richest' (i.e. least lean) condition in the data sets. Data is shown for the 127 mm combustor (a), where standard deviation values are normalized by the standard deviation for the ϕ=.695 case, and for the 243 mm combustor (b), where the richest case was ϕ=0.71.

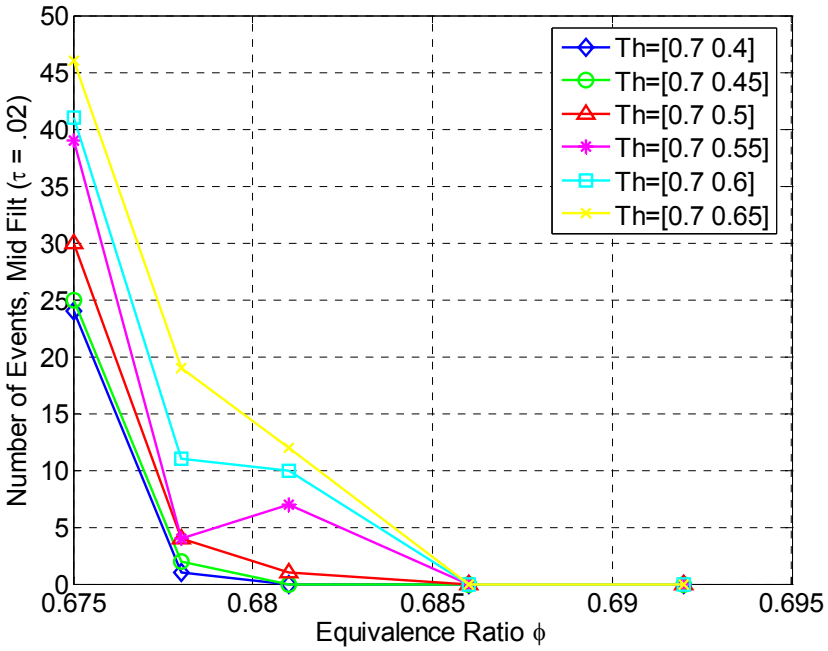

Figure 6-10. The number of events detected using thresholds on the filtered 'mid' signal, versus equivalence ratio for a range of threshold values.

6.4 Sensor and Data Fusion

In section 6.3.2, two margin detection schemes were evaluated, each relying on a different precursor type. Combining the two detection methods can address the limitations of both and provide an improved estimate of margin. As was seen earlier, detecting localized extinctions is rapid and otherwise robust except for the ambiguity regarding thresholds and observability. The number of threshold crossings rises linearly with diminishing margin but there is no reference point. In contrast, the presence of tornado bursts indicate a clear sign of danger, but the tornado signal is useless outside a very narrow parameter space near the blowout limit.

6.4.1 Combining Two Precursor Types

If we sacrifice survivability and rely on two sensors – one for localized extinction and one for tornado bursts – the overall scheme will be much more robust and efficient

than relying on any one precursor type alone. Essentially, the tornado sensor can provide the absolute reference needed by the localized extinction sensor to determine the location of the danger point. This can be compared with the desired operating point, and the parameter space in between will be linear with regards to the number of events detected by the localized extinction (mid) sensor.

Information from both sensors can be fused by an adaptive algorithm that updates the critical threshold crossing rate for the mid signal based upon tornado bursts detected by the high sensor. Let the actual operating state be denoted by the Greek letter η. The objective is to determine margin (M), or the difference between the present state and the blowout state:

$$M = \eta - \eta_{LBO} \tag{6.11}$$

Due to threshold ambiguity in the mid signal, η_{LBO} is not known precisely and the estimated margin from the mid signal ($\hat{M}_{mid}$) is different from the actual margin:

$$\hat{M}_{mid} = M + e_{mid} \tag{6.12}$$

The mid signal estimation error, e_{mid}, is the offset that results from threshold ambiguity. Equation (6.12) can be restated as

$$\hat{M}_{mid} = \eta - \hat{\eta}_{LBO,mid} \,, \tag{6.13}$$

where

$$\hat{\eta}_{LBO,mid} = \eta_{LBO} - e_{mid} \tag{6.14}$$

In Equation (6.14), $\hat{\eta}_{LBO,mid}$ is the estimated blowout state.

The state where tornado bursts are first detected can be declared a critical value, η_{crit}. η_{crit} is always a fixed distance Δ removed from η_{LBO}:

$$\eta_{crit} - \eta_{LBO} = \Delta > 0 \tag{6.15}$$

Δ in Equation (6.15) is assumed constant. Combining Equations (6.13), (6.14), and (6.15) gives the following expression

$$\hat{M}_{mid} - \Delta = \hat{M}_{mid,crit} = \eta - \eta_{crit} + e_{mid} \tag{6.16}$$

The point where tornado first appears (η_{crit}) can be considered a de facto blowout limit. While it is more conservative than the actual limit, it is a point where leaner operation would mean more tornado bursts and more unsteadiness. We can therefore consider $\hat{M}_{mid,crit}$ as defined in Equation (6.16) as a modified blowout margin.

As the flame approaches blowout from a stable condition, the first appearance of tornado bursts signifies that $\eta=\eta_{crit}$. At this state, $\hat{M}_{mid,crit}$ will equal e_{mid}. Once e_{mid} is known, $\hat{\eta}_{LBO,mid}$ can be updated by applying Equation (7.4) such that e_{mid} for the next iteration is lower:

$$\hat{\eta}_{LBO,mid}(k+1) = \Lambda * e_{mid}(k) + \hat{\eta}_{LBO,mid}(k) \tag{6.17}$$

The parameter k in Equation (6.17) is the update iteration and Λ is a positive scaling factor less than 1. The update described in (6.17) will occur whenever $\hat{\eta}_{LBO,mid}$ exceeds η_{LBO} in such a manner that M will become small and tornado bursts will become evident.

If $\hat{\eta}_{LBO,mid}$ is too conservative, tornado bursts will not occur, even when $\hat{M}_{mid,crit}$ is zero. The absence of tornado events over a sufficient amount of time will indicate that $\hat{\eta}_{LBO,mid}$ must be adjusted slightly towards leaner values until bursts are detected and the update method described earlier can take effect.

6.4.2 Probabilistic Estimation

The event spacing analysis of subsection 5.3.1 indicated that events, whether tornado bursts or localized extinctions, are a Poisson process; the spacing between events follows an exponential distribution with a cumulative distribution defined by the mean spacing, μ:

$$P(\delta < \delta_{ref}) = 1 - \exp(\delta_{ref}/\mu) \tag{6.18}$$

Equation (6.18) expresses the probability that the time spacing between two successive events (δ) is less than a reference value (δ_{ref}). Furthermore, the probability that the number of events in time period T (N_T) equals an integer κ is expressed by:

$$P(N_T = \kappa) = (T/\mu)^{\kappa} \exp(-T/\mu)/\kappa! \,. \tag{6.19}$$

The cumulative density function of a Poisson distribution, i.e., the probability that $N_T < \kappa$, is found by summing (6.19) from 0 to κ:

$$P(N_T < \kappa) = \sum_{i=0}^{\kappa} (T/\mu)^{i} \exp(-T/\mu)/i! \tag{6.20}$$

The analysis presented in Section 5.5.1 indicated that the number of localized extinctions, detected as threshold crossings of the OH chemiluminescence signal, will increase before the tornado burst. The low pass filtered alarm signal, A_{filt}, correlated best with the equivalence ratio when the filter time constant was 0.02. Since the alarm signal was a train of impulses, the filtered signal reflected the relative time spacing between successive impulses. Hence, multiple impulses spaced close together produced a larger amplitude filter response than isolated events. The fact that filtering the alarm signal improves correlation with the margin implies that there is a certain critical event spacing below which multiple events can destabilize the flame.

The estimation of flame dynamic response to localized extinction events can be combined with event statistics to develop a blowout probability model. Since multiple events spaced closely enough will destabilize the flame, the probability of this spacing can be inferred from the Poisson process. Hence, for a given mean event spacing, the probability that the spacing between any two events will be below a critical threshold is given by

$$P_{LBO} = P(\delta < \delta_{LBO}) = 1 - \exp(-\delta_{LBO} / E(\delta)), \tag{6.21}$$

where $E(\delta) = \mu$ and spacing between events is the inverse of the number of events per unit time, i.e. $\delta = \gamma^{-1}$.

The uncertainty in determining P_{LBO} from Equation (6.21) will arise mainly from the uncertainty in calculating the mean time between events, μ. For a given uncertainty in the mean spacing, ΔE, the corresponding blowout probability uncertainty can be expressed as:

$$\Delta P_{LBO} = \left|\exp(-\delta_{LBO} /(E(\delta) + \Delta E)) - \exp(-\delta_{LBO} /(E(\delta) - \Delta E))\right| \tag{6.22}$$

The uncertainty in mean spacing can be determined as follows. Equation (6.19) gives the probability that the number of events detected in time window T will be less than κ. The equation can be solved for κ to determine the 95 and 5 percentile values, $\kappa_{95\%}$, and $\kappa_{5\%}$. If the number of events in time period T is the mean value, $\bar{\kappa} = T / \mu$, then a time window estimate of $\mu = E(\delta)$ over that same time interval will result in the actual $E(\delta)$. However, since there is a 90% probability that the number of events will lie between $\kappa_{95\%}$, and $\kappa_{5\%}$, the 90% confidence interval for the $E(\delta)$ estimate will correspond to those values of κ. The normalized uncertainty $\Delta E^*(\delta)$ can be computed as:

$$\Delta E^*(\delta) = \frac{\Delta E(\delta)}{E(\delta)} = \frac{\Delta \mu}{\mu} = \frac{\kappa_{95\%} - \kappa_{5\%}}{\overline{\kappa}} \tag{6.23}$$

The normalized uncertainty is plotted against the normalized time interval, T/μ for a Poisson process in Figure 6-11. The curve $\Delta E^*(\delta)=3.3444(T/\mu)^{-0.5043}$ is plotted as well since it best fits the normalized uncertainty for T/μ values greater than 5. It is clear that the mean estimate improves with increasing time window and that, for a certain absolute uncertainty (ΔE(δ)), a much smaller time window is needed if μ is small. A smaller time window responds faster to signal variation but can become susceptible to noise when it is too small.

Since a blowout probability uncertainty will always exist, the question is how to manage this uncertainty. Clearly, blowout probability uncertainty is immaterial when the flame is far from blowout, but crucial when blowout is imminent. A nondimensionalized parameter (ΔP^*) may be defined that scales blowout uncertainty by the probability of 'not blowout', or the probability that the flame will be stable:

$$\Delta P^* = \frac{\Delta P_{LBO}}{1 - P_{LBO}} \tag{6.24}$$

The purpose of P^* is to quantify the observability of the flame. The flame can operate closer to extinction, for instance, if the probability uncertainty is low and margin can be determined with high certainty.

As discussed above, the uncertainty in E(δ) (i.e. ΔE(δ)), and therefore the uncertainty in P_{LBO} (i.e. ΔP_{LBO}), are both dependent upon the time interval (T) used for calculating E(δ). Furthermore, it is clear from Equation (6.21) that an operating point with lower P_{LBO} and a short time interval, T, can have the same ΔP^* value as an operating

point with higher P_{LBO} but longer time interval. Essentially, the normalized observability uncertainty is the same for a case far from blowout but short averaging time and another case close to blowout but longer averaging time. Clearly, the shorter time interval is desirable since it allows for more rapid determination of both $E(\delta)$ and P_{LBO}. An acceptable operating point can be characterized by mean event spacing $E(\delta)$ that optimizes between ΔP^*, the emissions performance of the combustor and the maximum time interval required (T_{max}).

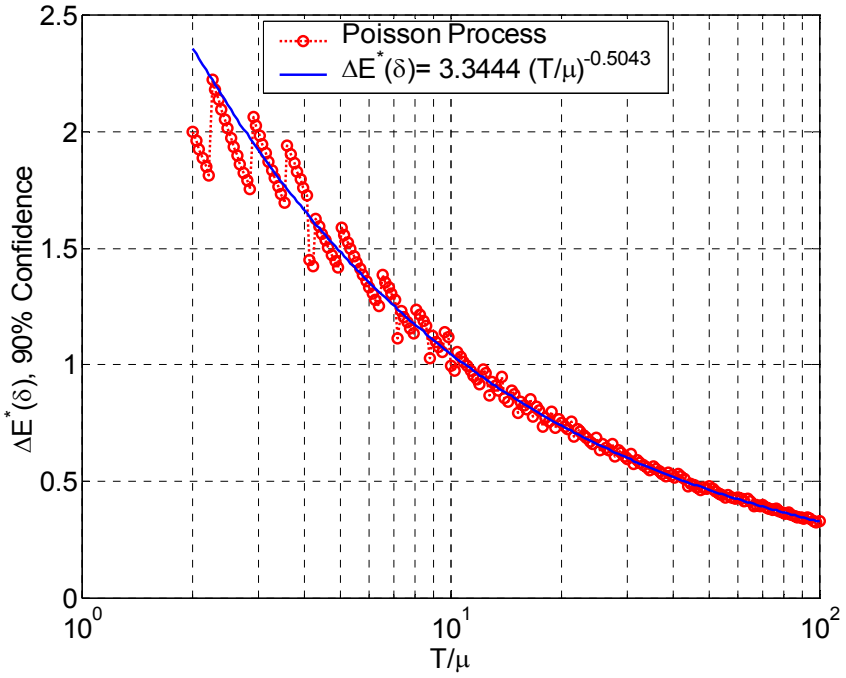

Figure 6-11. Normalized mean uncertainty ($\Delta E^*(\delta)$) as a function of normalized time interval (T/μ) for a Poisson process, where μ is the mean event spacing. Also shown is the curve corresponding to the best fit to the mean uncertainty for time intervals greater than 5μ.

CHAPTER 7. ACTUATION

The primary goal of actuation techniques is to provide an alternate stabilization mechanism for the flame or to increase the strength of the current stabilization point. In this study, the redistribution of the fuel inside of the combustor was chosen for its simplicity and practicality. The redistribution of the fuel in the combustor was accomplished by changing the fraction of the fuel injected through the premixed pilot injector located near the inlet of the combustor.

Most of the material presented in this chapter is a review of work done by Muruganandam on pilot stabilization of a premixed flame in a swirl and dump stabilized combustor. Dynamic characterization of the actuator, developed for this study, is presented as well.

7.1 Piloting Options

In the combustor employed, flame stabilization occurs due to the central recirculation zone created by the swirl, the outer recirculation created by the dump plane, or a combination of these. Muruganandam explored different piloting options with the current combustor; the locations that were considered are shown in Figure 7-1. The central pilot injects the fuel into the inner recirculation zone, and thus will stabilize a flame anchored on it by increasing the local equivalence ratio and flame speed. However, the central pilot will also reduce the amount of recirculation in the central region by increasing the axial momentum there. The annular pilot injects fuel into the outer shear layer between the main premixed jet and the outer recirculation zone through a set of 8 holes along the perimeter of the primary jet. The radical and heat feedback from

the enhanced recirculation zone could act as an anchor for the flame, by igniting the incoming mixture.

Muruganandam[17] further showed that both central and annular pilots were not very effective unless the pilot split fraction was relatively high (no effect for pilot fuel less than ~12%). This was conjectured to be due to the movement of the recirculation zone due to the pilot jets, which might move the stabilization point in the combustor. Another possibility could be that the fuel injected mixes with the main flow so fast that by the time it reaches the flame zone, there is no effect of the piloting. Schlieren photography was used to study the mixing of these pilot jets with the main flow. The pilot fuel was replaced by helium and the main flow was air with similar flow rates as the combustor operating conditions. The Schlieren images (Figure 7-2) show that the pilot fluid mixing is extremely rapid and support the rapid mixing argument.

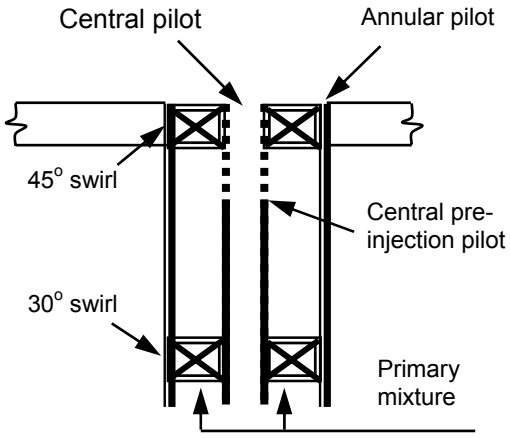

Figure 7-1. Schematic showing the various pilot options discussed. The central pre-injection pilot is the case used in the control experiments. Image adopted from Muruganandam[17]

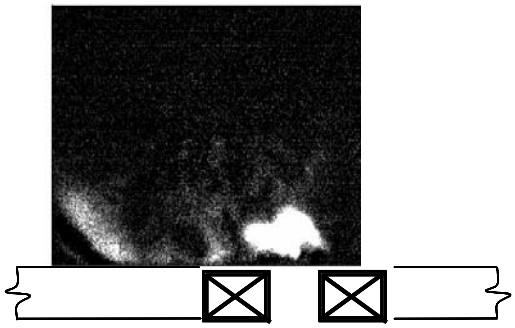

Figure 7-2. Schlieren image of the central pilot injected into cold flow. Lighter regions correspond to higher density gradients. Clearly, the jet does not penetrate more than one diameter into the combustor. Bright region at the left bottom corner of the image is an artifact of aberrations in the glass. Image adopted from Muruganandam.

The pre-injection pilot is a modification of the central pilot, where the pilot tube is not inserted all the way up to the inlet of the combustor. By introducing a richer reactant mixture ahead of the final swirler, the fuel species have some time to mix with the outer, primary fuel/air mixture. The main flame holding method in this case is most likely swirl based. The injection of a richer mixture directly into the central recirculation zone increases the reaction rate in that region, and hence assists in stabilizing the flame without increasing fuel flow rate. This pilot was found to be effective in decreasing the LBO limit for a pilot fuel fraction above ~5% of the total fuel flow.

In this work, a constant fraction of the total air is sent through the pilot injector always, to maintain a nominally constant velocity field. The total fuel was kept constant while changing the fractional fuel through the central, pre-injection pilot.

7.2 Effects of Piloting

This section considers the effect of fuel redistribution to the pilot. The effect of piloting on LBO limit, precursor detection, and NOx emissions will be investigated.

7.2.1 Effects on LBO and Sensing

Since the pilot injection can change the dynamics of the combustor near the LBO limit or change spatial extent of the active combustion region, it might influence the efficacy of the LBO precursor sensing. Thus the effect of piloting on the sensing technique was investigated through open loop tests. Figure 7-3 shows the effect on the LBO limit for various pilot fuel fractions. As indicated by the vertical lines, the LBO limit moves to leaner mixtures as pilot is increased. The average number of events sensed per second, as detected by the bandpass filtered acoustic signal, is also indicated for each pilot case. The acoustic based sensing approach, as described in Section 4.2.1, successfully tracks the change in the LBO limit, with the same number of events per second occurring at blowout regardless of the pilot fuel split.

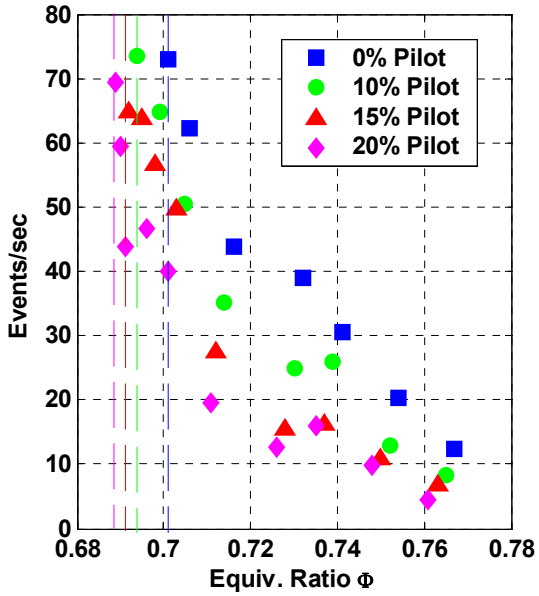

Figure 7-3. Average number of events per sec (detected via a filtered acoustic signal) as a function of equivalence ratio for various pilot fractions, with nominally same velocity field. The dotted lines indicate the respective LBO limits for each case.

7.2.2 *Effect of Pilot on NOx*

Since the pilot introduces local regions of higher equivalence ratio, it will also increase the overall NOx. However, since the LBO limit for the piloted system is leaner, the piloted combustor allows operation at a lower overall equivalence ratio (and thus reduced NOx) without loss of safety.

A comparison of piloted and unpiloted cases is shown in Figure 7-4, which indicates the NOx index as a function of the safety margin. The overall equivalence ratio for the piloted case was maintained at the LBO limit of the unpiloted combustor. It should be noted that NOx decreases with a decrease in pilot split fraction, but this also decreases the safety margin. Also, it can be seen that piloted combustor has a lower NOx index compared to zero-pilot combustor *for the same safety margin*. For example at a safety margin of 0.04 (6.5% pilot fraction), the NOx index is reduced by 23% compared to the unpiloted case.

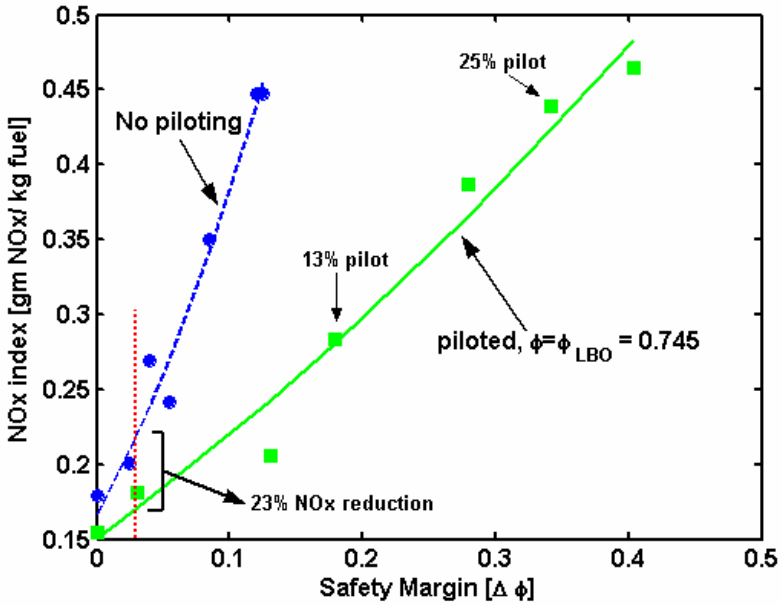

Figure 7-4. NOx reduction achieved with piloting for a fixed safety margin. Although piloting at fixed equivalence ratio increases NOx, it also boosts safety margin by decreasing the value of ϕ_{LBO}. For a given safety margin, piloting significantly reduces NOx. Image adopted from Muruganandam.

7.3 Actuator Dynamics

Understanding the flame's dynamic response to pilot actuation is fundamental for control. Observations suggest that piloting produces a non-minimum phase response with respect to alarms (and flame stability), i.e. piloting initially increases alarm frequency before reducing it in the steady state (Figure 7-5). This necessarily places a constraint on controller design, since the potential for blowout exists when the response magnitude is too large. Furthermore, it is evident that control actuation will not produce the desired response until the overshoot period has elapsed.

A crude linear expression for the effect of pilot on alarm frequency may be deduced from the observed response. Figure 7-5 shows how the alarms vary in time in response to a step increase in commanded pilot fraction. We can apply our understanding of alarms as a gauge of flame stability. Evidently, the flame becomes less stable in the transient before becoming more stable in steady state. This behavior gives rise to an 'undershoot', where the system initially moves in the opposite direction.

A linear, continuous system with 'undershoot' behavior would have an odd number of real zeros in the right hand s-plane[74]. If we assume linear dynamics (over some finite range), the Laplace domain transfer function between alarm frequency output and piloting input might take the following form:

$$\frac{\Gamma(\mathrm{s})}{\mathrm{P}(\mathrm{s})} = \frac{K(\mathrm{s}-z_{1,rhp})\ldots(\mathrm{s}-z_{2k-1,rhp})(\mathrm{s}+z_{2k})\ldots(\mathrm{s}+z_{m})}{(\mathrm{s}+p_1)(\mathrm{s}+p_2)\ldots(\mathrm{s}+p_n)} \tag{7.1}$$

The capital letters Γ and P represent the Laplace transform of alarm frequency and pilot fraction, respectively. The m zeros and n poles are respectively denoted by z_i and p_i, and K is a DC gain. As a further approximation, we can consider the following simplified, second order version of 7.1 with time delay:

$$G(s) = e^{-sT_d} \frac{K(s - z_{nmp})}{(s + \sigma + j\omega_d)(s + \sigma - j\omega_d)} \tag{7.2}$$

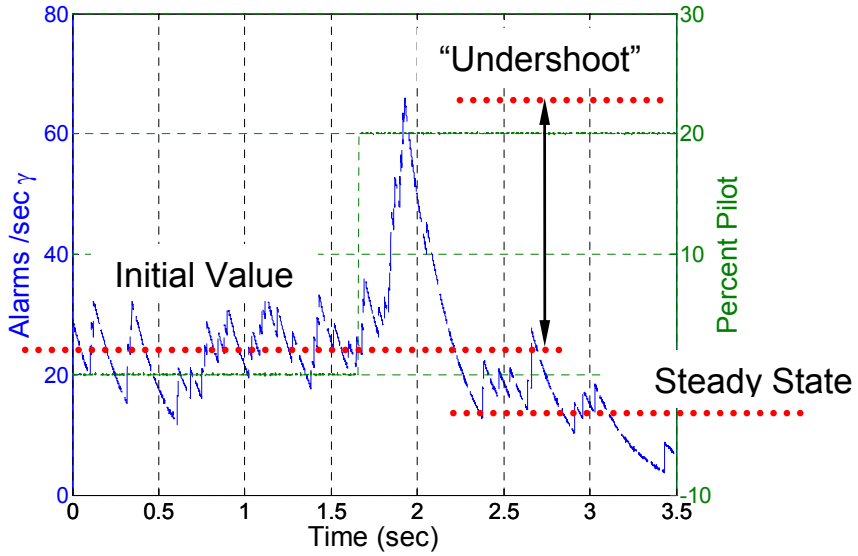

Figure 7-5. Response of alarm frequency to a step increase in pilot fraction. Alarms rise initially during the transient, before settling at a lower value.

The parameters in Equation (7.2) may be determined by examining the time response in Figure 7-5 and identifying the set of model parameters that can best replicate the observed response. In this case, the delay time (T_d) was determined to be 15ms, the single non minimum phase zero (z_{nmp}) was estimated at 1.33, the gain K has an estimated value of 27.95, and the real and imaginary part of the poles (σ and ω) were determined at approximately 6.00 and 6.20, respectively.

Figure 7-6 shows how the model described in Equation (7.2) compares to the actual response. The linear model seems to predict the undershoot whenever there was a step increase in pilot. The exception of course was at about 2 seconds when the nonminimum phase behavior was not evident at all. Note that the system never exhibits the nonminimum phase response during 'turn-off'.

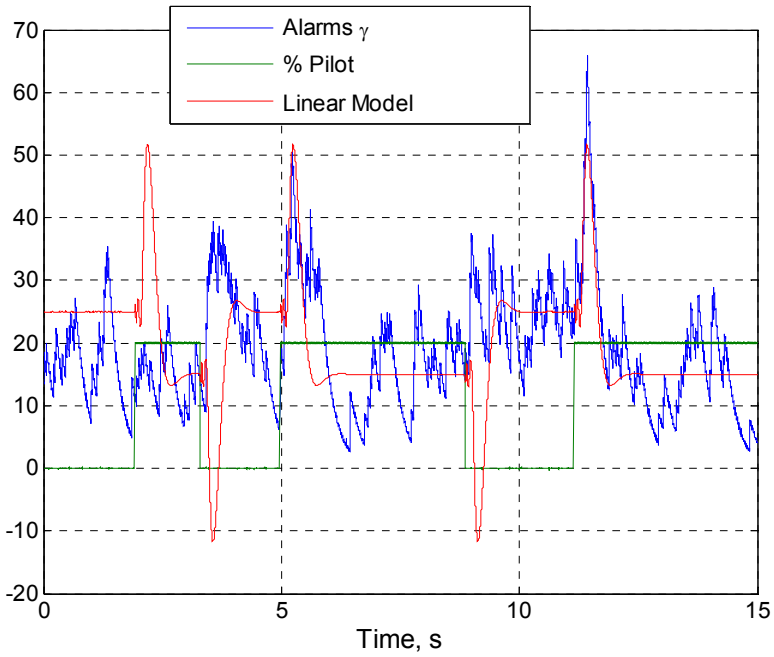

Figure 7-6. Response to change in pilot, with second order non minimum phase model.

It is evident from the results that the model is very crude. Most likely, there are unmodeled disturbances and nonlinearities that also have a significant bearing on the system. The prudent approach would be to treat actuator dynamics as a pure time delay and limit control gains such that the overshoot stays limited.

CHAPTER 8. CONTROL

This chapter describes the evolution of controller logic that was implemented to actuate the pilot split valves and mitigate blowout. Some of the margin estimation techniques, presented in Chapter 6, were implemented to determine the amount of actuation required. The nonminimum phase actuator dynamics, as discussed in Section 7.03, inhibited the implementation of a more complex control based on flame dynamics.

The role of the controller is to close the loop between margin estimation (as discussed in Chapter 5) and actuation (Chapter 7). A schematic of the system's signal and fluid flow is shown in Figure 8-1. The sensor detects either acoustic or electromagnetic radiation. Preprocessing involves filtering for alias and for prescribed bandwidths that respond to the flame's reaction rate (e.g., OH chemiluminescence at 390 nm). The threshold operation distinguishes the extreme features of the signal, which have been shown to correspond to localized extinction events or other precursors. Each threshold crossing is counted as an alarm. Proximity to blowout is a function of how many such precursors are detected per unit time, or alarm frequency. Two methods to determine alarm frequency were presented in Chapter 6. Specifically, these were the moving window summation and the forgetting filter. It was also shown that alarm frequency is a direct measure of blowout probability.

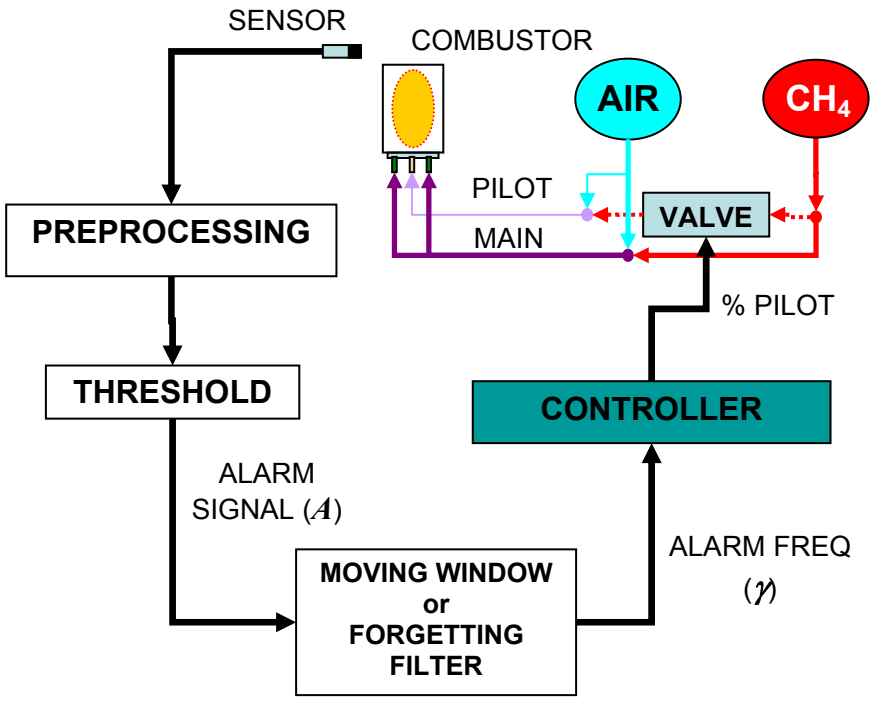

Figure 8-1. A schematic of the air, fuel, and signal flow. The controller converts the margin estimation (from alarm frequency, for instance) into an actuation command for the fuel split valve. The air flow split was fixed while fuel split was governed by the valve.

The controller's role now is to convert the estimate of margin into a command for the fuel split valve. Chapter 7 showed that for a fixed safety margin, there is a reduction in NOx for the piloted flame. However, for a fixed equivalence ratio, piloting will actually increase NOx due to the presence of a 'hot spot' in the flame. The control logic must, therefore, judiciously command the valves such that piloting is only applied when necessary. Furthermore, it is evident from the nature of blowout that control actuation must be rapid.

8.1 Rule Based Control

The simplest control algorithm is one that increments actuation when the system is critical, and decrements actuation when the system has been safe for a time period.

This rule based algorithm comprised the first iteration of a viable feedback blowout mitigation controller.

8.1.1 Algorithm

The rule based algorithm is shown in flowchart form in Figure 8-2. The signal (either OH chemiluminescence or bandpass filtered acoustic) is sampled in the initial, parallelogram box, and its absolute value ($|S|$) subsequently compared with the two thresholds, as was explained in Chapter 4. If the signal exceeds a more extreme MAX threshold, an event is declared if one is not already ongoing. An alarm is also declared at the beginning of the event, and a timer, which tracks time since last alarm, is reset. When the number of alarms per second (γ), calculated with a one second moving window summation, is greater than a critical value, actuation (i.e., pilot fraction) is incremented.

If the $|S|$ is between thresholds, i.e., between the MIN and MAX values, no action is taken until the next sample period. If the signal absolute value ($|S|$) is below the MIN threshold, then any ongoing events are declared terminated.

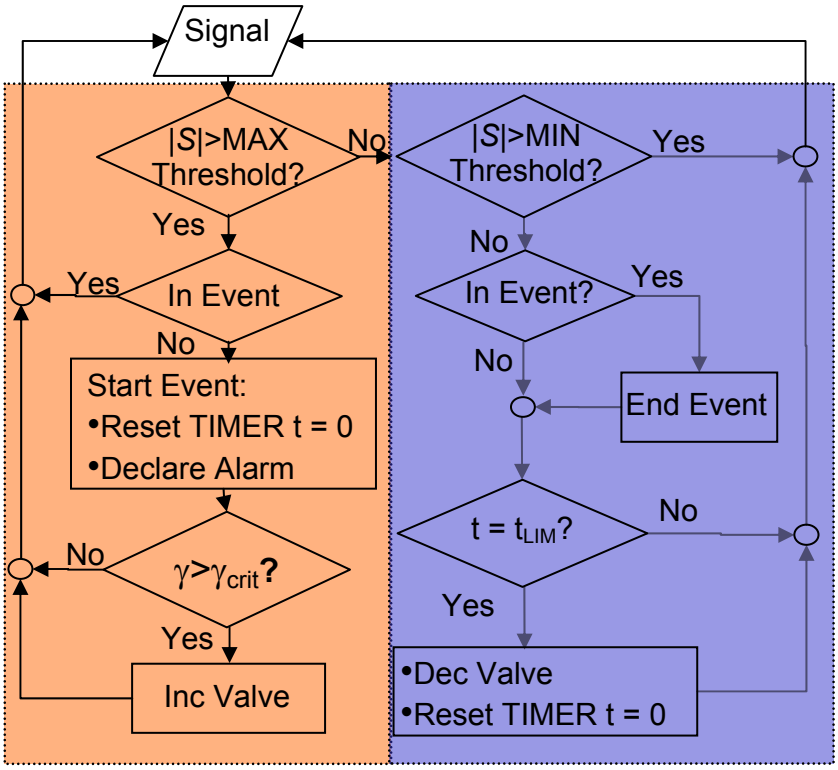

Figure 8-2. Flowchart of the rule-based blowout mitigation control algorithm. The algorithm has actuation increment (left) and actuation decrement (right) logic paths.

Each time a time interval ($t = t_{LIM}$) lapses without alarm activity, the valve is decremented. When precursors are detected, the control system declares an alarm, and the timer is reset ($t = 0$). The valve is incremented if the number of alarms over a 1 second moving window, i.e., alarm frequency, exceeds the critical value ($\gamma > \gamma_{crit}$).

The control algorithm has to account for a sensor signal that is subject to both drift and noise. The signal drift is mainly due to equivalence ratio changes and is a slow phenomenon. In contrast, the blowout precursors cause a brief, abrupt drop in the signal level. To calibrate for drift, the signal mean value is constantly updated based on the data from a fixed (previous) time window. As noted previously, two threshold levels are used: one for event start, one for event end. This allows for better noise rejection, and can be customized to suit specific combustors. Also, the threshold levels are based on a fraction

of the recent mean signal in order to account for long term changes in the system, and to adapt to changes in operating power.

8.1.2 Tuning

System tuning involves manipulation of the control parameters to achieve an ideal tradeoff between sensitivity and response time. Both the signal mean and the alarm count are updated based on samples and threshold crossings over a 1 second time window. The size of this time window has a direct bearing on the system's response time and susceptibility to noise; smaller time windows respond faster but are more susceptible to noise, and vice versa. Similarly, the critical alarm frequency that triggers actuation (γ_{crit}) and the time limit for alarms and valve decrement (t_{LIM}) also affect system response and noise sensitivity, as do the signal threshold levels and the valve increment and decrement values.

An effective loop gain may be described as a combination of parameters that lead to greater system response. One effective gain can be used to describe the decrement logic, or the left side of logic flowchart, and another may be used to describe the increment logic, or the right side of the flowchart. The time limit (t_{LIM}) and decrement step value contribute to the decrement gain, while the critical alarm frequency (γ_{crit}) and increment step value contribute to the increment gain. While the decrement occurs steadily, the increment has to be more severe and instantaneous to avoid a blowout. Therefore, the decrement loop pushing the system towards minimum pilot fuel split is tempered by a longer timer duration and smaller decrement steps, both of which lower the effective decrement gain. The alarm response loop, by contrast, has a higher effective gain with a low critical alarm frequency and a larger valve increment command.

8.1.3 Closed Loop Results – Optical Sensing

The rule based algorithm described above was implemented with optical-based detection of localized extinction precursors, in a study done in collaboration with Muruganandam[75]. The optical methods involve thresholding the OH chemiluminescence signal from a fiber placed near the midpoint of the combustor, as described in Section 4.1.2.

The control system was tested under two cases: one where the operating conditions were nominally steady and a second case where the air flow rate was independently varied. For both cases, the time window was set to 1 second, and the threshold levels were set at 35% and 40% of the mean signal. In addition, the maximum number of alarms allowed before the system begins to increase the pilot fuel was two (in the 1 second window).

It can be seen from Figure 8-3 that the controller eventually attains a nearly stationary condition. The minimum allowable pilot fraction appears to be 14% based on the effective safety margin set by the chosen controller parameters. Since extinction precursors do occur somewhat randomly and because the controller always tries to keep lowering the pilot fraction in the absence of alarms, the system drifts between the minimum pilot fraction and a higher value of ~18%.

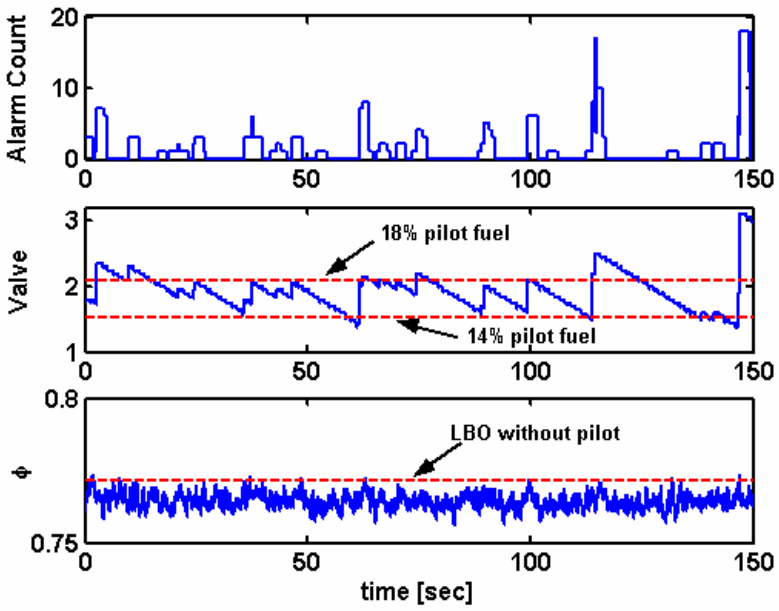

Figure 8-3. Response of the integrated control system to nominally stationary operating conditions. Localized extinctions were detected using optical OH Chemiluminescence. Results were obtained via collaboration with Muruganandam.

Figure 8-4 shows the behavior of the closed-loop system when there are fluctuations in the operating conditions. In this case, the starting conditions were chosen such that the combustor was stable without piloting. The air flow was manually varied, with the overall equivalence ratio changed at a maximum rate of 0.03 sec^{-1}. It can be seen that the controller did not take action until the LBO limit was approached (at $t \cong 54s$). It successfully suppressed blowout by turning on the pilot. For $60<t<100$ s, when the combustor equivalence ratio was below the unpiloted LBO limit but the air flow was essentially constant, the system operated in a nearly stationary mode. When the air was finally decreased to a point where the equivalence ratio was no longer below the unpiloted LBO limit, the controller eventually diverted all the fuel back to the main flow. The relatively slow response of the system in decreasing the pilot is due to the very conservative set of valve decrement parameters chosen.

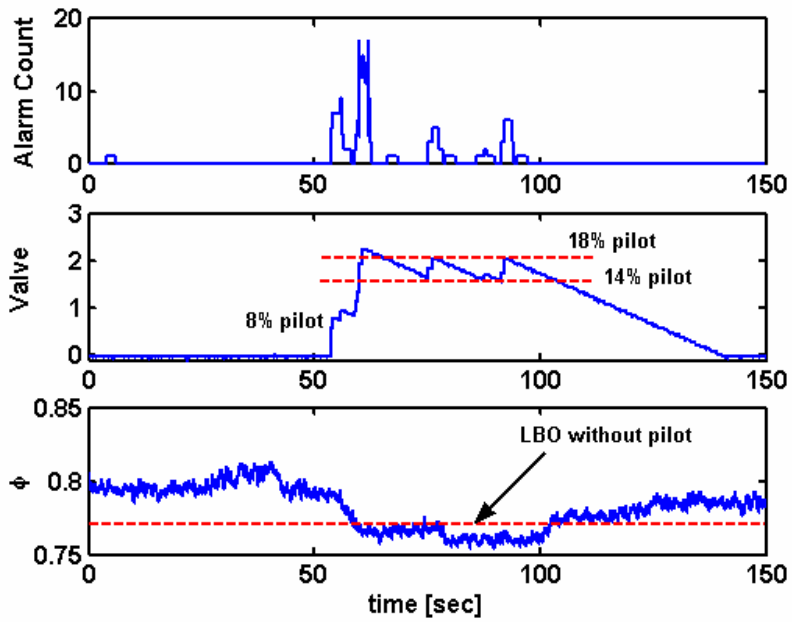

Figure 8-4. Response of the integrated control system to varying operating conditions. Localized extinctions were detected using optical OH Chemiluminescence. Results were obtained via collaboration with Muruganandam.

8.1.4 Closed Loop Results – Acoustic Sensing

As was shown in Chapter 4, the blowout margin can also be detecting by tracking threshold crossings in a bandpass filtered acoustic signal. The rule based control algorithm presented above was implemented with the acoustic based detection of localized extinctions as well.

Figure 8-5 shows the time dependence of various parameters associated with the control system's response to varying air flow rate. The top plot shows how the equivalence ratio varies as air flow changes with time. The next two plots are the filtered acoustic signal and the alarm count signal. As the filtered acoustic signal crosses thresholds, alarms are counted. The alarm sum over a previous 1 second window is the overall alarm level ($\gamma_{1s,win}$), which determines the actuation (valve counts, bottom plot of Figure 8-5). Valve counts are given in whole numbers from 0 to 1000, with 1000 corresponding to 10 valves open and 20% pilot fuel fraction. Each 100 counts

correspond to a fully open valve, and the remainder fractions are sent as pulse width modulation (PWM) commands to the next valve or valves.

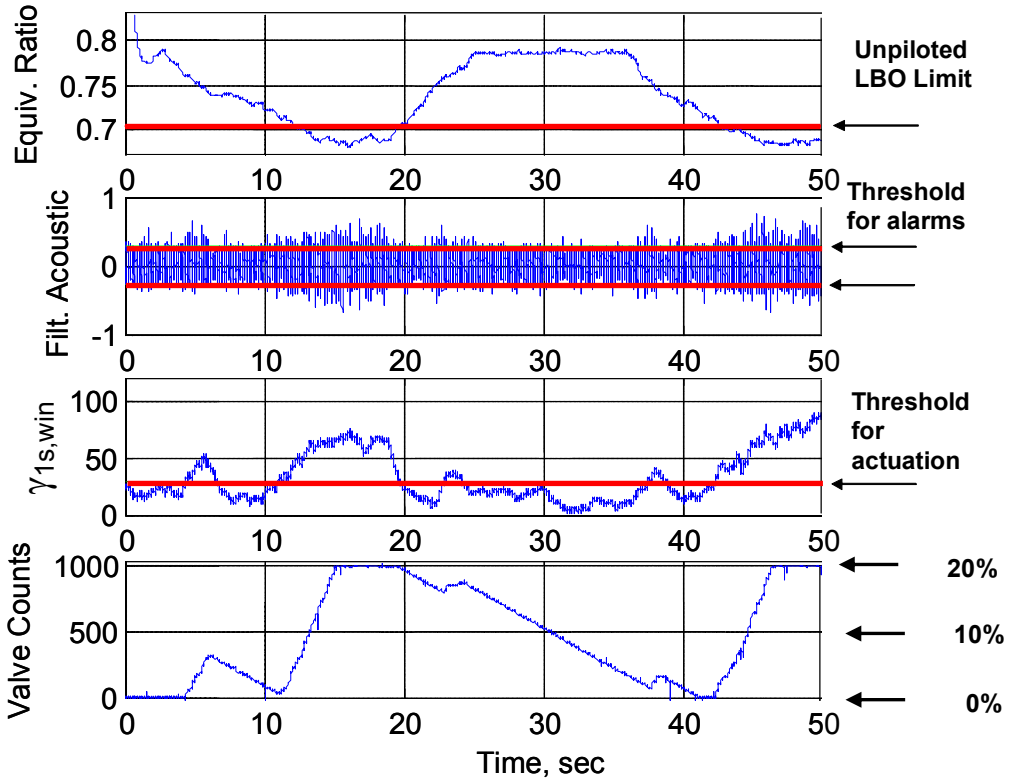

Figure 8-5. Results from varying the air flow rate to the combustor under rule-based feedback control with acoustic based sensing. The top plot shows the equivalence ratio variation, the second plot shows the filtered acoustic signal with thresholds, the third plot shows the number of threshold crossings per second, determined with a moving window, and the bottom plot displays the valve actuation, with 1000 corresponding to 20% pilot.

The results show that as valves are opened to increase the pilot fuel split, the alarms subside. This indicates the flame was made more stable (i.e., safety margin increased) as a result of the actuation. Also evident are the two logic modes. When excessive alarms are detected, the actuation rises rapidly. In contrast, as the flame becomes richer, actuation declines at a steady rate.

8.2 Proportional Derivative Control

The rule based control algorithm is a simplistic, overly conservative approach to blowout mitigation. The algorithm does not take advantage of the linearity between alarm frequency and blowout margin, which was shown for both the acoustic and optical signals in Chapters 4, 5 and 6. Nor does rule based control fully utilize the capabilities of the 10kHz control hardware. The one second summation which it uses to determine alarm frequency has a periodic frequency response with a folding frequency much below Nyquist.

The number of threshold crossings per unit time (or alarm frequency, γ) in both the optical OH chemiluminescence and bandpass filtered acoustic signals increase almost linearly with diminishing margin. Hence, both the margin and its rate of change may be ascertained from those signals. Furthermore, the alarm frequency can be calculated much more efficiently using the forgetting filter compared with the moving window summation used by the rule-based controller. The developed sensing and margin estimation methods have made the system both (fairly) linear (with bandpass filtering) and dynamically well behaved (with the forgetting filter).

8.2.1 Control Algorithm

To capitalize upon the improvements in detection and estimation, a proportional derivative controller was implemented, whereby the pilot fraction actuation was proportional to both the events per second (γ) and its derivative; i.e.

$$\%\text{Pilot} = K_p * (\tilde{\gamma}_e) + K_d * \frac{d}{dt}(\tilde{\gamma}_e)_{Filtered} \tag{8.1}$$

where the relative event frequency is computed as a difference from a fixed set point:

$$\tilde{\gamma}_e = \gamma_e - \bar{\gamma}_{e,set} \tag{8.2}$$

In order to compute a meaningful derivative, this signal had to be filtered of high frequency noise via a low pass filter. For this purpose, a 2nd order Butterworth filter was used. It was designed to balance time response and noise attenuation characteristics. The computation of the derivative term may be characterized as a convolution of derivative and filtering operations; i.e.,

$$\frac{d}{dt}\left(\tilde{\gamma}_e\right)_{Filtered} = D(z) * F_{lp}(z) * (\tilde{\gamma}_e), \tag{8.3}$$

where $D(z)$ is the derivative transfer function and $F_{lp}(z)$ is the 2nd order low pass Butterworth filter. The control law can now be reformulated as the following transfer function relating controller output to input:

$$\frac{\%\text{Pilot}(z)}{\tilde{\gamma}_e(z)} = K_p + K_d * D(z) * F_{lp}(z) \tag{8.4}$$

Figure 8-6 displays a block diagram of the proportional derivative controller.

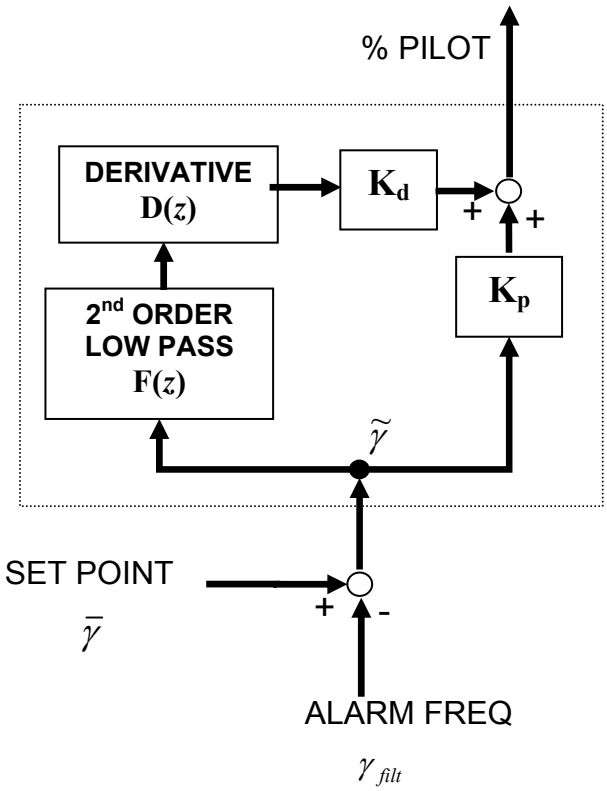

Figure 8-6. Block diagram of the proportional derivative controller.

8.2.2 Tuning

Control parameters were chosen to optimize performance while minimizing noise sensitivity. In the frequency domain, proportional derivative control is a high pass filter, and in combination with a 2nd order lowpass, the controller appears as a 'peak' in frequency, as seen in Figure 8-7. As seen in the figure, the ratio Kp/Kd determines the first corner frequency, where the magnitude rises at a fixed rate of 20 dB per decade frequency. The location (and height) of the peak is determined by the low pass cutoff frequency. The phase lead provided by the derivative term exists up to the low pass cutoff frequency.

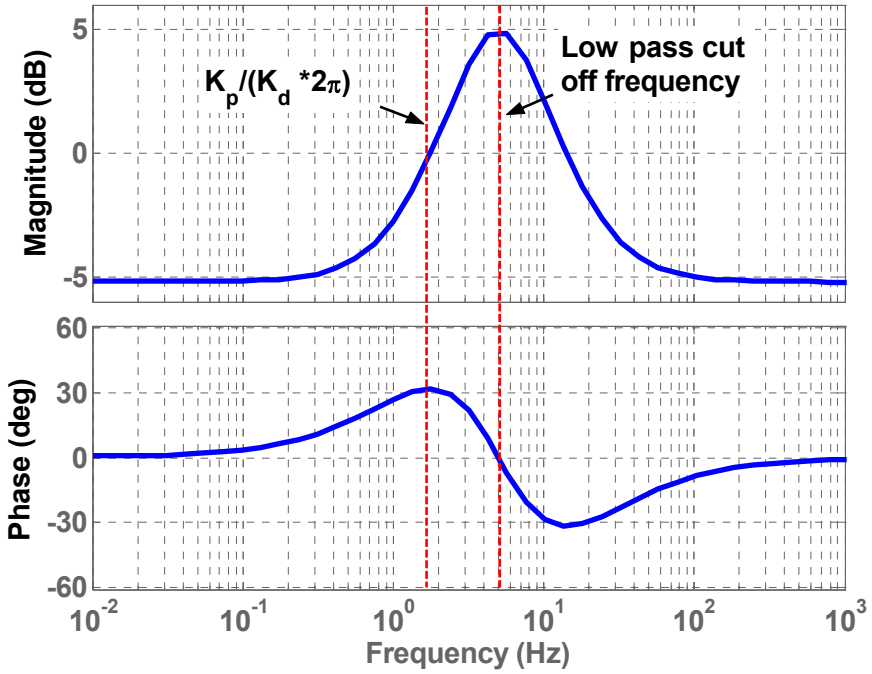

Figure 8-7. Bode diagram of the proportional derivative controller frequency response.

The location, size, and shape of the frequency response should satisfy two requirements: performance and noise attenuation. For the reported experiments, Kp was 0.55 and Kd was set to 5.5. Hence, the first 'corner frequency' of the controller frequency response was 1.56 Hz (see Figure 8-7). The lowpass filter (F_{lp}) cutoff frequency was set at 5 Hz. The set point for event frequency (see Figure 8-6) was 15, and the pilot split was restricted to values between 0% and 20%. The gains could thus set high enough for rapid response, as noise attenuation was provided by the low pass characteristics of the forgetting filter.

Figure 8-8 illustrates the combined effect of the forgetting filter and the proportional derivative (PD) controller in the frequency domain. A one sample delay has been included in the combined system. The controller's main advantage is its speed, i.e., it boosts bandwidth. Whereas the forgetting filter alone has a bandwidth of .8 Hz, with

the controller the bandwidth has been increased to 2.5 Hz. Noise suppression is provided by the low pass part of the controller and the low pass characteristics of the forgetting filter.

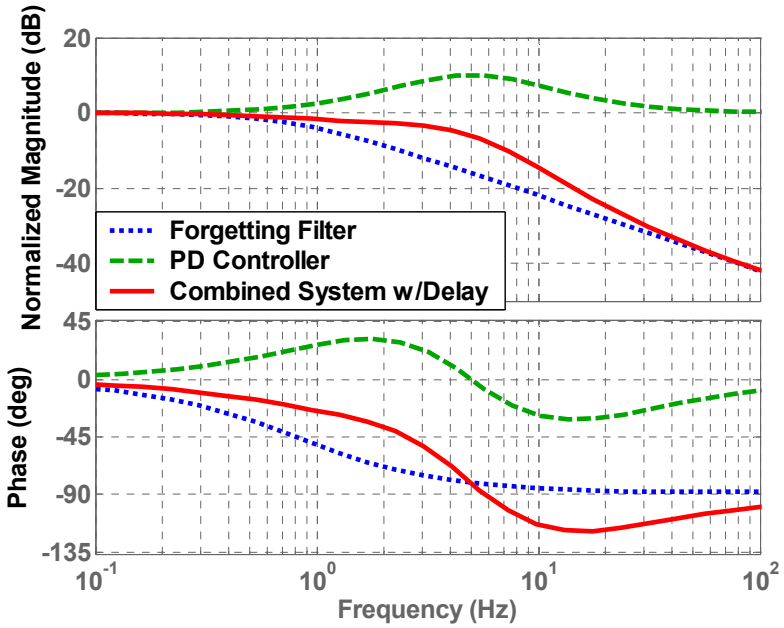

Figure 8-8. Bode diagram of the combined forgetting filter and PD control system with a one sample delay. The magnitudes have been normalized with respect to the DC gain.

8.2.3 Feedback Control Results

A viable control scheme will allow continuous operation below the unpiloted LBO limit, and rapid response to equivalence ratio variations. To investigate the controller's performance, the combustor was subject to air flow variations that dynamically altered the equivalence ratio. The bandpass filtered acoustic signal was used to detect localized extinction events, as described in Section 4.2.1, and margin was estimated using the 'forgetting filter' approach explained in Section 6.2.2.

Figure 8-9 shows a long duration operation interval at an equivalence ratio below the nominal LBO limit. The actuator remained saturated at 20% pilot during the interval, providing the maximum safety margin allowable. The event frequency fluctuated due to

flow disturbances. Since the actuator was saturated, such oscillations could not be attenuated.

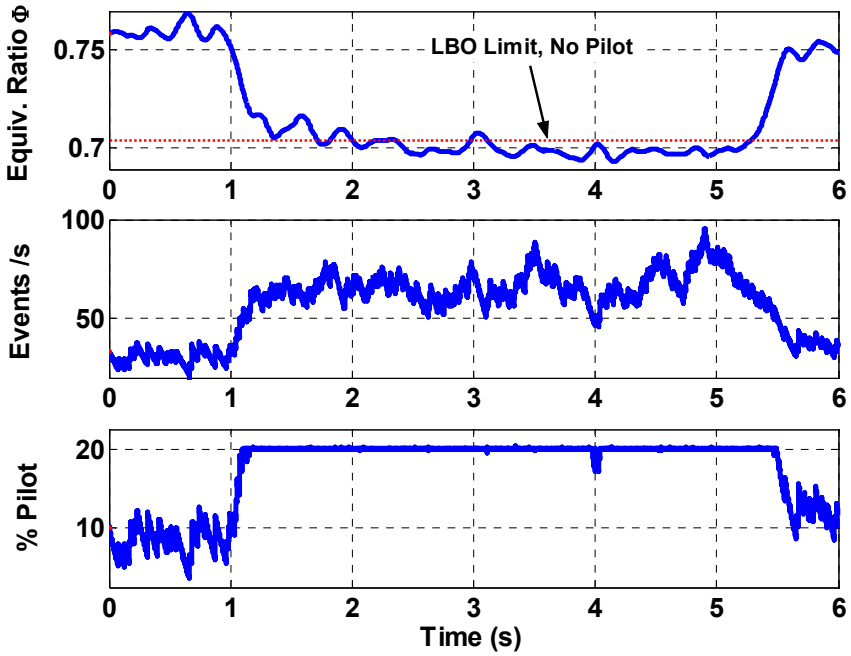

Figure 8-9. Time plot of closed loop, continuous lean operation. The top plot shows the equivalence ratio as it drops below the combustor's nominal LBO limit. The event frequency, as calculated by the forgetting filter, is shown in the middle plot. The bottom plot shows the pilot actuation commanded by the PD controller.

The control system was also evaluated for time response. Rapid performance is necessary due to the nature of LBO. For the reported experiments, a steep drop in the equivalence ratio caused a brief overshoot, providing a quick 'blast' of maximum pilot and stabilizing a potentially unsteady condition. Subsequently, the proportional term allowed the pilot to track the event frequency, which was proportional to real time LBO probability.

Figure 8-10 shows the results of the system response to a series of sharp dips in equivalence ratio caused by a rapidly increasing air flow rate. Once again, the bandpass filtered acoustic signal was used to detect localized extinction events. After each sharp dip in equivalence ratio, a corresponding reaction by the controller is evident. The

proportional derivative controller anticipates each dip and commands the pilot to saturation. A 0.05 drop in equivalence ratio over 0.1 seconds to an equivalence ratio below the LBO limit would normally have blown out the flame but the controller prevented this outcome with rapid actuation.

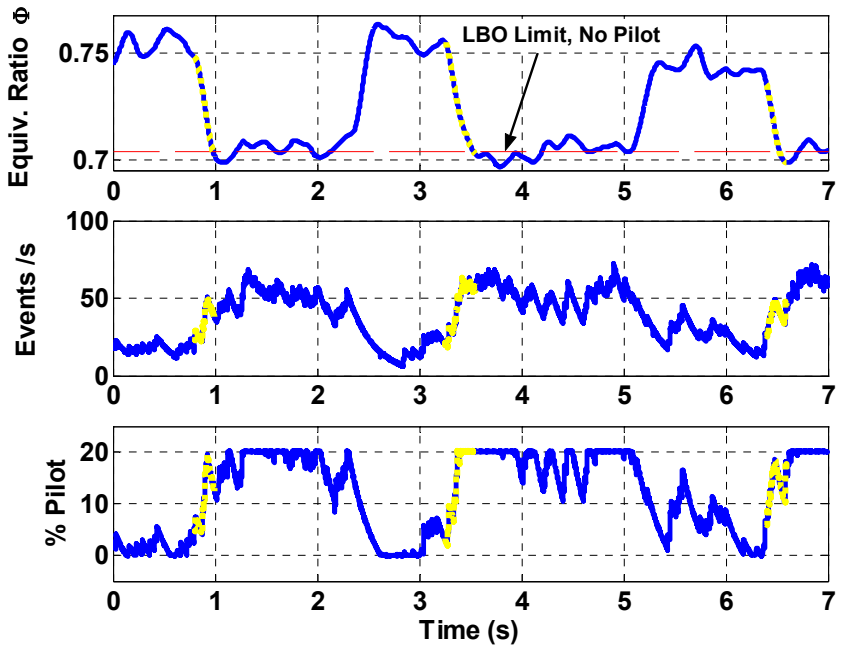

Figure 8-10. System response to rapid change of operating conditions. The plot labels are the same as Figure 8-9. The top plot shows the equivalence ratio as it drops below the combustor's nominal LBO limit. The event frequency, as calculated by the forgetting filter, is shown in the middle plot. The bottom plot shows the pilot actuation commanded by the PD controller.

It is clear from Figure 8-10 that the event frequency remains between 40 to 60 events per second. In contrast, the event frequency reaches almost 100 per second in the open loop case (see Figure 6-7). Figure 8-11 illustrates how the system responds during the steep equivalence ratio dips in terms of events per second. The three traces correspond to the three equivalence ratio drops depicted in Figure 8-10. Initially, there is a linear rise, but below an equivalence ratio of about 0.72, the event frequency saturates as the actuation takes effect.

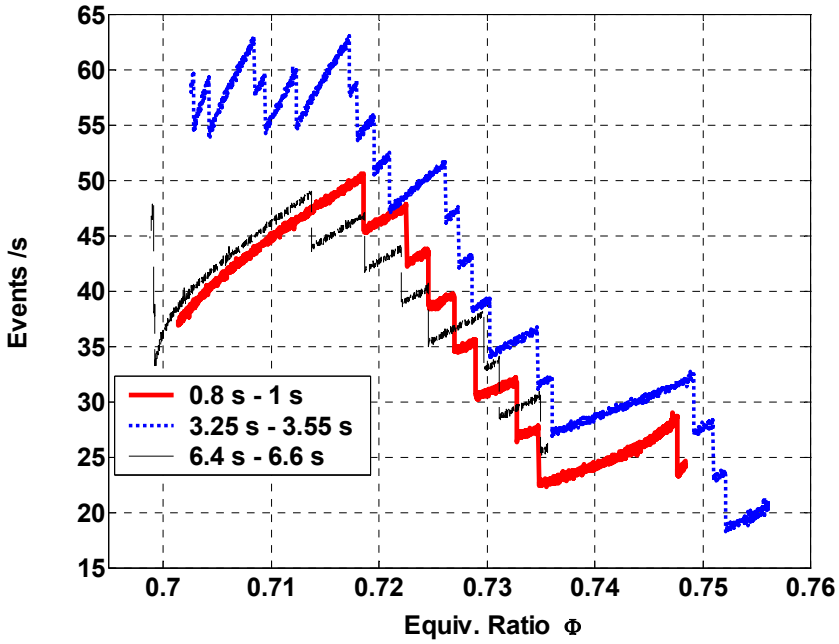

Figure 8-11. System response to rapid drops in equivalence ratio. The event frequency rises linearly until the actuation takes full effect

CHAPTER 9. CONCLUSIONS AND RECOMMENDATIONS

The work presented here constitutes a progression in the understanding of lean flames, the blowout phenomenon, effective margin detection techniques, and blowout mitigation strategies. While much of the work presented relies on experimental data, the expectation is that theories will eventually emerge that draw upon these findings and explain the results in a more fundamental manner.

9.1 State of Previous Work

Previous work has treated blowout either as a singular, sudden event[5,18,19,34] or as a symptom of a 'special' operating state[3,5,17]. A holistic approach to understanding flame evolution from stable to blowout had not yet been developed. Furthermore, control for blowout mitigation was in its infancy.

Previously developed pressure-based methods for detecting LBO precursors required processing techniques that were either sensitive to noise (kurtosis) or prohibitively time consuming (wavelet transform). Optical methods that relied on OH chemiluminescence, on the other hand, were sensitive to sensor placement and field of view. [15]

While flame pulsations near blowout have been the focus of several studies, they have either examined laminar non-premixed as a fundamental study of chaos[6], or have completely neglected time. In all cases, dynamics have only been studied for the regime where the margin was minimal and blowout imminent. Practical combustors will not operate near such conditions because the weakened flame is inefficient and unstable.

Margin estimation has so far relied extensively on mapping the operating regime *a priori*. Margin estimation techniques that rely on mapping are highly vulnerable to sensor failure, noise, and unmodeled disturbances. A further complication arises when the operating regime is *n*-dimensional. Mapping techniques will require *n* sensors (such as fuel and air flow meters) to determine each of *n* states (such as velocity and equivalence ratio) in real time. When the number of sensors is fewer than required, additional processing is required to parse all the state parameters. The imposed delay may significantly hamper control.

Finally, blowout mitigation control applications had not yet taken into account fundamentals of system dynamics[17-21]. Instead, these applications relied on rule based algorithms that placed very minimal faith in their own margin estimation techniques. As a result, the control increased rapidly to saturation when the combustor was in danger and backed off very slowly when it was safe. This overly conservative approach resulted in unnecessary actuation and less than ideal emissions performance.

9.2 Contributions of Present Work

This section highlights the major achievements in the present work. Advancements were made in detecting blowout precursors, modeling lean flame dynamics, estimating margin, and mitigating blowout via actuation and control.

9.2.1 Detection

The first part of this work involved the detection of lean blowout precursor events using an acoustic sensor. Specifically, strain-induced localized extinction events, which were found to increase near blowout, were detectable in a frequency range of the acoustic

signal. These events were previously detectable either via optical means, or acoustically through more calculation-intensive wavelet transforms.

Analysis indicates that the spectrum of both the OH chemiluminescence and acoustic signals rise in the low frequency range at lean conditions. This was attributed to the increase in localized extinction events. Apparently, the time scales associated with such events manifested as low frequency signal content.

The technique developed here involved bandpass filtering the acoustic signal in the frequency range that was most sensitive to margin. These events were clearly discernable in the bandpass filtered acoustic signal and could be detected using thresholds. The filtered acoustic signal correlated better with the OH chemiluminescence signal compared with the raw, unfiltered acoustic signal. This confirmed that the localized extinction events are more clearly evident in the filtered acoustic signal. The bandpass filtering technique was much faster than previously developed acoustic detection techniques and reliably tracked fluctuations in equivalence ratio.

9.2.2 Dynamics

The dynamics of flame transition from a base-stabilized to a thin, 'tornado'-like flame configuration were studied in the interest of improving margin estimation. At very lean conditions, the base-stabilized flame was shown to 'burst' into the tornado mode for several milliseconds and at sporadic intervals as defined by a Poisson process. It was shown that a localized extinction event could be detected in the flame region immediately before the flame transitions to tornado mode. More generally, fluctuations in OH chemiluminescence, as detectable with a first order lowpass filter, also preceded the flame mode transition. The dynamics of the low pass filter characterized the flame

structure response (e.g. transition to tornado) to disruptions in the reaction rate (e.g. localized extinctions).

The analysis also indicated that flame transition toward blowout in a shorter combustor was comparable to flame transition towards a stable tornado state in a longer combustor. In all combustor lengths, flame 'bursts' from base stabilized to 'tornado' configurations became more frequent at leaner conditions, indicating the flame was transitioning away from the base-stabilized shape. However, since tornado-like flame shape was stable only in a combustor that was long enough to completely contain it, the transition in the shorter combustor was towards blowout; in a longer combustor the transition was towards another stable configuration. It was postulated, therefore, that the flame in a longer combustor transitions to a stable tornado state similar to the way the flame transitions to blowout in a shorter combustor. Since the combustor cooled during the tornado bursts, prolonged cooling probably inhibited the flame's ability to return to a base-stabilized configuration.

It was further shown that while flame degeneration into the 'tornado' configuration is a nonlinear bifurcation, the flame dynamics preceding such an event can be approximated as linear. Filtering the 'mid' OH chemiluminescence signal in lowpass with the appropriate time constant resulted in a filtered signal that could reliably predict flame transition. This suggested that the tornado burst was preceded by either a more severe fluctuation in OH or by several smaller fluctuations spaced close together.

Although a causal and dynamic relationship exists between localized extinctions and tornado bursts, the statistics of event spacing indicated that both events were Poisson processes; i.e., the occurrence of an event (whether localized extinction or tornado burst)

did not influence the time until the next event of the same type. The duration of each event type was less sensitive to equivalence ratio than spacing, indicating that the timescale of event recovery was determined more by the recovery of the flow, and less by the amount of chemical heat release at the onset of the event.

The hypothesized flame dynamics were then compared with swirl flow theory, which predicts bifurcation behavior in nonreacting flows with near critical swirl numbers. At certain rotation rates, the nonreacting flow can equally favor two vortex breakdown states; similarly, the flame's flow field gradually starts favoring another vortex breakdown state (from bubble-type to double helical) as the equivalence ratio is reduced and more perturbations, i.e., reaction rate fluctuations, are evident.

9.2.3 Margin Estimation

The reported improvements in detection and the enhanced understanding of flame dynamics were applied to the development of new margin estimation techniques. Margin estimation involved determining the frequency of localized extinctions in real time and transforming this frequency to a blowout proximity gauge.

It was determined that simply examining the frequency (i.e. number per unit time) of detected localized extinction 'events' provided a reliable gauge of blowout proximity. The same event frequency is apparent at blowout regardless of the pilot fraction. Event frequency was then considered a de facto margin estimate, but was dependent upon threshold level.

A 'forgetting filter' method of determining alarm, or event, frequency was shown to be superior to the previously used one-second 'moving window' summation. The frequency of localized extinction events, detected either via optical or acoustic methods

were shown to increase with diminishing margin. Whereas the one second moving window assigned equal weighting to all event information in a one second window, the forgetting filter gave maximum weight to the most recent time sample and exponentially declining importance to older samples. This resulted in a faster, less digitized gauge of event frequency, and a faster determination of blowout proximity.

Methods were then proposed for incorporating both localized extinctions and tornado bursts in margin estimation routines. While margin detection based on localized extinctions was effective, the threshold sensitivity rendered the approach vulnerable to offset errors from either false positives or negatives. Tornado bursts were less ambiguous, and could provide a reference point by which to calibrate margin estimation routines that were based on localized extinctions. Dynamic analysis indicated that low pass filtering the OH chemiluminescence signal, which detects localized extinctions, allowed prediction of the tornado bursts. A routine was proposed wherein the same OH signal could be thresholded to detect localized extinctions and lowpass filtered to detect tornado bursts. The ambiguous threshold can be calibrated in real time by simply resetting the margin to zero whenever a tornado burst is evident.

9.2.4 Actuation and Control

Redistributing the fuel in the combustor increased the blowout stability margin, but the richer pilot actually increased NOx. However, for a given safety margin, the piloted flame had lower NOx emissions than the unpiloted flame. Therefore, controller had to maintain safety margin without over-actuation.

The first attempt at control employed a rule based algorithm. Actuation was incrementally increased or decreased based on whether the combustor was presumed

'safe' or not. The rate of increase was significantly higher than the rate of decrease. The overly conservative algorithm ensured a stable flame but did not produce the optimal emissions performance.

A more advanced, proportional derivative controller was implemented. It was based on a rapid assessment of margin, which was made possible by the 'forgetting filter'. Both the margin and its rate of change determined the amount of commanded actuation. The closed loop system responded rapidly to abrupt changes in equivalence ratio, and the flame was stable in both steady state and transient operation.

9.3 Recommendations for Future Study

While advancements have been made in understanding blowout and blowout mitigation, the field is still in its infancy. Turbulent flames are so complex that even numerical simulations cannot characterize them fully. Control theory and applications are also constantly evolving as processors are shrinking. This section presents some suggestions for future work in the advancement of lean blowout mitigation.

9.3.1 Detection

An acoustic method to detect blowout precursors was presented in this work. However, the development is purely based on empirical data and heuristic understanding, and not on a fundamental understanding of flame acoustics. For instance, dynamic instabilities can be characterized as a result of an 'acoustically compact' flame resonating in a semi-enclosed chamber. Assuming that the flame thickness is much smaller than the acoustic wavelength, the system can be simplified. Unfortunately, no such simplifications are evident when considering the random pulsations of a lean flame. A more detailed analysis would have to be conducted based on numerical simulations.

While it was shown that flame shape modulations ('bursts') can be predicted using the OH chemiluminescence near the base of the flame, an acoustic method for doing the same was not developed. This can be undertaken either by looking for a frequency signature, as was done with the optical signal, or via a more detailed acoustic study of the flame.

Another open issue in detection is the nature of the so-called 'localized extinctions'. While prior studies have generally assumed that they are strain induced[15-17] this has only been shown for stagnation plane flames[12,13] and not for turbulent premixed flames.

9.3.2 Dynamics

The work presented here validated a simple, linear model for characterizing flame pulsations. It was clear that the base-stabilized flame is at a dynamic equilibrium, and that, as the margin decreases, perturbation amplitude and frequency (detected with OH chemiluminescence) increase and another equilibrium state emerges.

These promising results indicate that the flame dynamics should be studied further, with more and better sensors. More specifically, the radius of the inner recirculation 'bubble' should be monitored and correlated with its luminosity. If the stated conclusions are accurate, then the severe and closely spaced fluctuations in luminosity should affect the radius as if it were a dynamic system. A more detailed analysis may uncover dynamic complexities and nonlinearities. The aim of the dynamic characterization should be to predict the flame mode transition to 'tornado'.

9.3.3 Margin Estimation

The present work incorporates signal processing and data fusion techniques to integrate sensor information and enhance margin estimation. Furthermore, blowout probability is determined based on the dynamic characterization of the flame. Clearly, with improved detection and dynamic characterization, estimation can be improved as well.

While a framework to adaptively update the margin estimate was presented, the technique was not implemented. Ideally, the update algorithm should be implemented with control, with the state backing away from the blowout limit once a tornado burst was determined to be imminent. However, the actuator was not powerful enough nor dynamically well behaved enough to rapidly and reliably correct the state once a tornado burst was deemed imminent. Data indicated that only a 20 ms warning time was available before flame shape degeneration, and the actuator, with its nonminimum phase behavior, was not capable of responding in that time frame. Therefore, the margin estimation techniques presented here should be implemented with more advanced and faster actuation. One possibility is to incorporate plasma actuation, or total fuel flow control in addition to fuel split control.

9.3.4 Actuation and Control

As mentioned earlier, actuator limitations, associated with the valve's nonminimum phase response, inhibited the implementation of a more advanced or higher performance control algorithm. Hence, plasma actuation, total fuel control, and even swirl variation should be investigated as possible mitigation techniques.

Plasma actuation has received much attention for blowout mitigation applications[76,77]. However, the main drawbacks are the power requirements and the

electromagnetic disturbance that is generated every time there is a pulse. The latter drawback has the potential of interfering with detection. However, a plasma jet is ideally suited for proportional derivative control. The overall fuel flow rate (which responds relatively slower) can be governed with proportional feedback while the faster, electromagnetic pulse can be turned on whenever the derivative term is large. Hence, the plasma can stabilize the flame until the fuel flow responds.

The analysis presented in this work confirmed that the dynamics of a swirl and dump stabilized flame are very similar to nonreacting swirl flow dynamics when the rotation rate is varied. It is therefore intuitive that by varying the swirl angle, a lean flame may be stabilized. A rapid rotational actuator need only control this angle in real time to directly alter the flow field, and therefore, flame stability.

Only two control architectures, rule based and lead lag, were investigated in this work, but the scope exists for further experimentation, especially if the flame and actuator dynamics can be better understood and modeled. The possibilities for control are continually expanding as computational power becomes increasingly cheaper and processors become smaller. Improvements in control performance will result from a better understanding of flame dynamics and disturbances, and better actuators.

REFERENCES

[1] Mongia, H.C., "Aero-Thermal Design and Analysis of Gas Turbine Combustion Systems: Current Status and Future Direction," AIAA Paper 98-3982, 1998.

[2] Tacina, R., Mao, C. P., and Wey, C., "Experimental Investigation of a Multiplex Fuel Injector Module for Low Emission Combustors", paper no. AIAA 2003-0827, 41st AIAA Aerospace Sciences Meeting, Reno, NV, Jan 6-9, 2003.

[3] Nicholson, H., and Field, J., "Some Experimental Techniques in for the Investigation of Mechanism of Flame Stabilization in the Wakes of Bluff Bodies", Third Combustion Institute Symposium, 1951.

[4] Chen, T. H., Goss, L. P., Talley, D., and Mikolaitis, D., "Stabilization zone structure in jet diffusion flames from liftoff to blowout", paper AIAA-89-0153, 27th AIAA Aerospace Sciences Meeting, Reno, NV, Jan 9-12, 1989.

[5] Chao, Y.C., Chang, Y.L., Wu, C.Y., and Cheng, T.S., "An Experimental Investigation of the Blowout Process of a Jet Flame", Twenty Eighth Symposium (International) on Combustion, 2000.

[6] Bayliss, A., Leaf G., Matkowsky B., "Pulsating and Chaotic Dynamics near the Extinction Limit", *Combustion Science and Technology*, v. 84, (1992) pp. 253-278.

[7] Gorman, M., el-Hamdi, M., Robbins, K., "Chaotic Dynamics Near The Extinction Limit of a Premixed Flame on a Porus Plug Burner", *Combustion Science and Technology*, v. 98 (1994) pp. 47-56.

[8] Law, C. K., "Dynamics of Stretched Laminar Flames", *Proc. Comb. Inst.*, Vol. 22, 1988, pp 1381-1402.

[9] Ghoniem, A. F., Soteriou, M. C., Knio O. M., and Cetegen, B., "Effect of Steady and Periodic Strain on Unsteady Flamelet Combustion", *Proc. Comb. Inst.*, Vol. 24, 1992, pp 223-230.

[10] Sardi, K., Taylor, A. M. K. P., and Whitelaw, J. H., "Extinction of Turbulent Counterflow Flames under Periodic Strain", *Combustion and Flame* , Vol. 120, 2000, pp. 265-284.

[11] Sardi, K. and Whitelaw, J. H., "Extinction Timescales of Periodically Strained Lean Counterflow Flames", *Experiments in Fluids*, Vol. 27, 1999, pp. 199-209.

[12] Im, H.G., Bechtold, J. K., and Law, C. K., "Response of Counterflow Premixed Flames to Oscillating Strain Rates", *Combustion and Flame*, Vol. 105, 1996, pp 358-372.

[13] Korusoy, E. and Whitelaw, J.H., "Extinction and relight in opposed flames", *Experiments in Fluids*, Vol. 33, 2002, pp 75-89.

[14] Black, D.L., and Smith, C.E., "Transient Lean Blowout Modeling of an Aero Low Emission Fuel Injector", AIAA-2003-4520, 39th AIAA/ASME/SAE/ASEE Joint Propulsion Conference, Huntsville, AL, Jul 20-23, 2003.

[15] Muruganandam, T.M., Nair, S., Neumeier, Y., Lieuwen T., and Seitzman, J. M., "Optical and Acoustic Sensing of Lean Blow Out Precursors", AIAA 2002-3732, Joint Propulsion Conference, Indianapolis, IN July 7-10, 2002.

[16] Nair, S., and Lieuwen, T., "Acoustic Detection of Imminent Blowout in Pilot and Swirl Stabilized Combustors", GT 2003-38074, Proceedings of ASME/IGTI Turbo Expo 2003 Atlanta, Georgia, June 16-19, 2003.

[17] Muruganandam, T. M. "Sensing and Dynamics of Lean Blowout in a Swirl Dump Combustor", Ph.D. diss., Georgia Institute of Technology, 2006.

[18] Lucenko, M., Vanderleest, R. E., Onge, K. J. St., "Method and Apparatus for Detecting Burner Blowout", United States Patent Number 5581995, Dec 10, 1996.

[19] Snyder, T. S., Rosfjord, T. J., "Active Gas Turbine Combustion Control to Minimize Nitric Oxide Emissions", United States Patent Number 5706643, Jan 13, 1998.

[20] Nakae, T., Tamugi, A., Minemura, A., Ikawa, H., and Yoshida, M., "Combustion Control for Low NOx Combustor", AIAA 2002-3726, 38th AIAA/ASME/ASEE Joint Propulsion Conference & Exhibit, Indianapolis, IN, 7-10 July, 2002.

[21] Mongia, H.C., Held, T.J., Hsiao, G.C., and Pandalai, R.P., "Challenges and Progress in Controlling Dynamics in Gas Turbine Combustors", *Journal of Propulsion and Power,* Vol. 19 No. 5, Sept.-Oct. 2003, pp. 822-829.

[22] Turns, Steven R. *An Introduction to Combustion*, 2nd ed. McGraw Hill, Boston, 2000.

[23] Correa, S. M., "A Review of NOx Formation under Gas-Turbine Combustion Conditions," *Combustion Science and Technology*, Vol. 87, 1993, pp. 329-362.

[24] Zeldovich, J., "The Oxidation of Nitrogen in Combustion and Explosions," Acta Physicochimica USSR, Vol. 21 (4), 1946, pp. 577-628.

[25] Strehlow, R. A., and Savage, L. D., "The Concept of Flame Stretch", *Combustion and Flame*, Vol. 31, 1978, pp. 209-211.

[26] Muller, C.M., Breitbach, H., and Peters, N., "Partially Premixed Turbulent Flame Propagation in Jet Flames", *Proc. Comb. Inst.*, vol. 25, 1994, pp. 1099-1106.

[27] Schefer, R. W., and Goix, P. J., "Mechanism of flame stabilization in turbulent, lifted-jet flames", Combustion and Flame, vol. 112, 1998, pp. 559-574.

[28] Warris, A. M., and Weinberg, F., "Ignition and Flame Stabilization by Plasma Jets in Fast Gas Streams", *Proc. Comb. Inst.*, Vol. 20, 1984, pp. 1825 – 1831.

[29] Weinberg, F.J., "Advanced combustion methods", Academic press, 1986.

[30] Galley, P., Pilla, G., Lacostet, D., Ducruix, S., Lacas, F., Veynante, D., and Laux, C.O., "Plasma enhanced combustion of a lean premixed air propane turbulent flame using a nanosecond repetitively pulsed plasma", paper AIAA-2005-1193, 43rd AIAA Aerospace Sciences meeting and exhibit, Reno, NV, Jan 10-13, 2005.

[31] Switenbank, J., Turan, A., and Felton, P.G., "Three-dimensional two-phase modeling of gas turbine combustors", Gas Turbine Combustor Design Problems, Lefebvre, A. H., editor, Hemisphere Publishing, NewYork, 1980, pp. 249-314.

[32] Lucca-Negro O., and O'Doherty T., "Vortex Breakdown: A Review", *Prog. Energy and Comb. Sci.*, Vol. 27, 2001, pp. 431-481.

[33] Sarpkaya T. "On Stationary and Traveling Vortex Breakdowns", *J Fluid Mech* 1971; 45(3):545-59.

[34] Novak F., and Sarpkaya, T. "Turbulent Vortex Breakdown at High Reynold's Numbers" *AIAA Journal* 2000 Vol.38 No.5.

[35] Althaus, W., Krause, E., Hofhaus, J., and Weimer, M. "Bubble- and Spiral- Type Breakdown of Slender Vortices", *Experimental Thermal and Fluid Science* 1995; 11:276-284.

[36] Wang, S., and Rusak, Z. "On the Stability of Non-columnar Swirling Flows", *Phys. Fluids* 1996;8(4):1017-1023.

[37] Sohn, K-H., Rusak, Z., and Kapila, A. "Effect of Near-Critical Swirl on the Burke-Schumann Reaction Sheet", *Journal of Engineering Mathematics* 2006;54:181-196

[38] Faler, J.H., Leibovich, S. "Disrupted States of Vortex flow and Vortex Breakdown." *Phys Fluids* 1977;20:1385-400.

[39] Bradley D., Gaskell, P.H., Gu, X.J., Lawes, M., and Scott M.J., "Premixed turbulent flame instability and NO formation in lean-burn swirl burner", *Combustion and Flame*, Vol. 115, 1998, pp 515-538.

[40] Lilley, D.G., "Swirl Flows in Combustion: A Review", *AIAA Jl.*, Vol. 15, No. 8, 1977, pp1063-1078.

[41] Baker, R.J., Hutchinson, P., Khalil, E.E., and Whitelaw, J.H., "Measurements of Three Velocity Components in a Model Furnace with and without Combustion", *Proc. Comb. Inst.*, Vol. 15, 1975, pp553- 559.

[42] Chigier, N. A., and Dvorak, K., "Laser Anemometer Measurements in Flames with Swirl", *Proc. Comb. Inst.*, Vol 15, 1975, pp. 573-585.

[43] Lucca-Negro O., and O'Doherty T., "Vortex Breakdown: A Review", *Prog. Energy and Comb. Sci.*, Vol. 27, 2001, pp. 431-481.

[44] Wang, S., Hsieh, S-Y., and Yang, V., "Unsteady Flow Evolution in Swirl Injector with Radial Entry in Stationary Conditions", *Physics of Fluids*, Vol. 17, 2005, pp. 1-13.

[45] Rusak, Z., Kapila, A. K., and Choi, J. J., "Effect of Combustion on Near-Critical Swirling Flow", *Combustion Theory and Modeling*, Vol. 6, 2002, pp. 625-645.

[46] Lewis, B. and von Elbe, G., *Combustion, Flames and Explosions of Gases*, 2nd ed., Academic Press, 1961.

[47] Wohl, K., Kapp, N.M., and Gazley, C., "Flame Stabilization and Quenching", Proc.Comb. Inst., Vol. 3, 1951, pp. 3-21.

[48] Kostiuk, L.W., Bray K.N.C., and Cheng, R. K., "Experimental Study of Premixed Turbulent Combustion in Opposed Streams. Part II – Reacting Flow Field and Extinction", *Combustion and Flame*, Vol. 92, 1993, pp. 396-409.

[49] Roquemore, W. M., Reddy, V. K., Hedman, P. O., Post, M. E., Chen, T. H., Goss, L. P. Trump, D., Vilimpoc, V., and Sturgess, G. J., "Experimental and Theoretical Studies in a Gas-Fueled Research Combustor", Paper AIAA-91-0639, 29th Aerospace Sciences Meeting, Reno, NV, Jan 7-10, 1991.

[50] De Zilwa, S.R.N., Uhm, J.H., and Whitelaw, J.H., "Combustion Oscillations Close to the Lean Flammability Limit", *Comb. Sci. and Technol.*, Vol. 160, 2000, pp 231-258.

[51] Hedman, P.O., Fletcher, T.H., Graham, S.G., Timothy, G.W., Flores, D.V., and Haslam, J.K., "Observations of Flame Behavior in a Laboratory-Scale Pre-mixed Natural Gas/Air Gas Turbine Combustor from PLIF measurements of OH", Paper No. GT-2002-30052, Proceedings of ASME Turbo Expo 2002, Jun 3-6, Amsterdam, Netherlands, 2002.

[52] Althaus W., and Weimer M., "Review of the Aachen Work on Vortex Breakdown", in Dynamics of Slender Vortices, Krause E., and Gersten K. (Eds.), IUTAM Symposium on Dynamics of Slender Vortices, Kluwer Academic Publishers, 1998, pp. 331-344.

[53] Gupta, A. K., Lilley, D.G., and Syred, N., *Swirl Flows*, Abacus Press, Kent, England, 1984.

[54] Gaydon, A.G. and Wolfhard, H.G., "Flames: Their Structure, Radiation, and Temperature", 4th edition, Chapman and Hall, 1978.

[55] Lawn, C.J., "Distributions of Instantaneous Heat Release by the Cross-Correlation of Chemiluminescent Emissions," Combustion and Flame, Vol. 132, 2000, pp. 227-240.

[56] Higgins, B., McQuay, M. Q., Lacas, F., Rolon, J. C., Darabiha, N., and Candel, S., "Systematic measurements of OH chemiluminescence for fuel-lean, high-pressure, premixed, laminar flames", *Fuel*, Vol. 80, 2001, pp 67-74.

[57] Roby, R. J., Reaney, J .E., and Johnsson, E. L., "Detection of Temperature and Equivalence Ratio in Turbulent Premixed Flames Using Chemiluminescence," *Proceedings of the 1998 Int. Joint Power Generation Conference*, Vol. 1, 1998, 593-602.

[58] Morrell, R., Seitzman, J., Wilensky, M., Lee, J., Lubarsky, E., and Zinn, B., "Interpretation Of Optical Flame Emissions For Sensors In Liquid-Fueled Combustors," paper AIAA-2001-0787, *39th AIAA Aerospace Sciences Meeting*, Reno, NV, Jan 8-11, 2001.

[59] Photomultiplier. (2007, March 22). In Wikipedia, The Free Encyclopedia. Retrieved 21:19, April 27, 2007, from http://en.wikipedia.org/w/index.php?title=Photomultiplier&oldid=116943476

[60] Gaydon, A.G. and Wolfhard, H.G., "Flames: Their Structure, Radiation, and Temperature", Fourth edition, Chapman and Hall, 1978.

[61] Lawn, C.J., "Distributions of Instantaneous Heat Release by the Cross-Correlation of Chemiluminescent Emissions," *Combustion and Flame*, Vol. 132, 2000, pp. 227-240.

[62] Roby, R.J., Hamer, A.J., Johnsson, E.L., Tilstra, S.A., and Burt, T.J., "Improved Method for Flame Detection in Combustion Turbines", *Transactions of the ASME*, Vol. 117, 1995, pp. 332 –340.

[63] Mehta, G.K., Ramachandra, M.K., and Strahle, W.C., "Correlations between Light Emission, Acoustic Emission and Ion Density in Premixed Turbulent Flames", *Eighteenth Symposium (International) on Combustion,* 1981, pp 1051-1059.

[64] Roby, R. J., Reaney, J .E., and Johnsson, E. L., "Detection of Temperature and Equivalence Ratio in Turbulent Premixed Flames Using Chemiluminescence," Proceedings of the 1998 Int. Joint Power Generation Conference, Vol. 1, 1998, pp. 593-602.

[65] Morrell, R., Seitzman, J., Wilensky, M., Lee, J., Lubarsky, E., and Zinn, B., "Interpretation Of Optical Flame Emissions For Sensors In Liquid-Fueled Combustors," paper AIAA-2001-0787 at the 39th AIAA Aerospace Sciences Meeting, Reno, NV, January 8-11, 2001.

[66] Muruganandam, T. M., Nair, S., Prakash, S., Scarborough, D., Neumeier, Y., Lieuwen, T., Jagoda, J., Seitzman, J., and Zinn, B., "An Active Control System for LBO Margin Reduction in Turbine Engines", AIAA 2003-1008, 41st Aerospace Sciences Meeting & Exhibit, Reno, NV, January 6-9, 2003.

[67] Strahle, W., "On Combustion Generated Noise", *Journal of Fluid Mechanics*, Vol. 49(2), 1971, pp. 399-414.

[68] Kotake, S., and Takamoto, K., "Combustion Noise: Effects of the Velocity Turbulence of Unburned Mixture", *Journal of Sound and Vibration*, Vol. 139, 1990, pp. 9-20.

[69] Prakash, S., Neumeier, Y., Zinn, B. "Investigation of Mode Shift Dynamics in Lean, Premixed Flames" AIAA 2006-0961, 44th Aerospace Sciences Meeting & Exhibit, Reno, NV, January 9-12, 2006.

[70] Huang, Y. and Yang, V. "Bifurcation of flame structure in a lean-premixed swirl-stabilized combustor: transition from stable to unstable flame," *Combustion and Flame* v.136 (2004) 383–389.

[71] Muruganandam, T.M. and Seitzman, J. "Characterization of extinction events near blowout in swirl-dump combustors", *41st AIAA/ASME/SAE/ASEE Joint Propulsion Conference & Exhibit*, Tuscon, AZ, July 10-13, 2005.

[72] Hayter, Anthony J. Probability and Statistics for Engineers and Scientists. 2nd ed. 2000 Duxbury p.657-72.

[73] Noble, D. R., Zhang, Q., Shareef, A., Tootle, J., Meyers, A., Lieuwen, T., "Syngas Mixture Composition Effects Upon Flashback and Blowout," Proceedings of ASME Turbo Expo 2006: Power for Land, Sea, and Air, GT2006-90470.

[74] Franklin, G., Powell, J., and Emami-Naeini, A. *Feedback Control of Linear Systems*. 3rd Ed. Addison-Wesley Publishing Co. Reading, MA 1994. p.161.

[75] Muruganandam, T. M., Nair, S., Prakash, S., Scarborough, D., Neumeier, Y., Lieuwen, T., Jagoda, J., Seitzman, J., and Zinn, B., "An Active Control System for LBO Margin Reduction in Turbine Engines", AIAA 2003-1008, 41st Aerospace Sciences Meeting & Exhibit, Reno, NV, January 6-9, 2003.

[76] Choi, W., Neumeier, Y., Jagoda, J. , "Stabilization of a Combustion Process Near Lean Blow Off (LBO) by An Electric Discharge", AIAA 2004-982, 42nd Aerospace Sciences Meeting & Exhibit, Reno, NV, January 5-8, 2004.

[77] Choi, W., Neumeier, Y., Jagoda, J. , "Preliminary Study of a Low Power Plasma Radical Jet Generator for Combustion Systems", Proceedings of ASME Turbo Expo 2006: Power for Land, Sea, and Air, GT2006 p 877-884.

VITA

SHASHVAT PRAKASH

PRAKASH, born in Madison, Wisconsin, attended public schools in Cincinnati, OH, Indianapolis, IN and Hudson, OH. He completed his Bachelor's in Mechanical Engineering from University of Illinois at Urbana-Champaign in December 1997. He went on to complete his Master of Science in Mechanical Engineering from Carnegie Mellon University in December of 1999. At CMU, his research focus was computational design of micro electromechanical systems (MEMS). Mr. Prakash held an Aerospace Engineer position at NASA Goddard Space Flight Center, where he was a member of the Attitude and Orbit Control Systems group, contributing to Triana and ST-7 missions. In August 2002, Mr. Prakash came to Georgia Tech to pursue his doctorate in Mechanical Engineering. Mr. Prakash enjoys outdoor activities, particularly downhill skiing.